NATIONAL TECHNICAL UNIVERSITY OF ATHENS

SCHOOL OF MECHANICAL ENGINEERING

ARIS KONSTANTINIDIS

ANALYSIS AND DESIGN OF NOVEL SUPERELASTIC COMPRESSION PLATE WITH ADJUSTABLE PRE-TENSION FOR LONG BONE OSTEOSYNTHESIS

Department of Mechanical Design & Automatic Control

Machine Elements Laboratory

Supervisor: Associate Professor Vasilios Spitas

Athens 2022

ΕΘΝΙΚΟ ΜΕΤΣΟΒΙΟ ΠΟΛΥΤΕΧΝΕΙΟ

ΣΧΟΛΗ ΜΗΧΑΝΟΛΟΓΩΝ ΜΗΧΑΝΙΚΩΝ

ΑΡΗΣ ΚΩΝΣΤΑΝΤΙΝΙΔΗΣ

ΑΝΑΛΥΣΗ ΚΑΙ ΣΧΕΔΙΑΣΜΟΣ ΚΑΙΝΟΤΟΜΟΥ ΥΠΕΡΕΛΑΣΤΙΚΗΣ ΠΛΑΚΑΣ ΣΥΜΠΙΕΣΗΣ ΜΕ ΡΥΘΜΙΖΟΜΕΝΗ ΠΡΟΕΝΤΑΣΗ ΓΙΑ ΟΣΤΕΟΣΥΝΘΕΣΗ ΜΑΚΡΩΝ ΟΣΤΩΝ

Τομέας Μηχανολογικών Κατασκευών και Αυτομάτου Ελέγχου

Εργαστήριο Στοιχείων Μηχανών

Επιβλέπων: Αναπληρωτής Καθηγητής Βασίλειος Σπιτάς

Αθήνα 2022

--- blank page ---

Acknowledgments

First of all I would like to thank my supervisor Associate Professor Vasilios Spitas for providing me with the opportunity to work on a thesis topic combining the field of mechanical design and bio-mechanics and for his invaluable help and advice in every stage of the project.

I would also like to thank my project coordinator Christos Kalligeros for his eagerness to advise me and answer my questions, for the excellent handling of every problem that occurred during the course of the project and for making me feel welcome in the workplace.

I would like to thank Mr Vasileios Soranoglou,MD for his indispensable help in understanding the problem at hand and his input in the medical aspects of the project.

Thank you to my colleagues Thanasis Alexopoulos and Dimitris Georgiou for their zealous contribution to the completion of the project.

Finally, thank you to my family and my partner for their unwavering support and understanding throughout my studies and diploma thesis project.

Solemn declaration for plagiarism and copyright theft:

I have read and understood the rules for plagiarism and how to properly cite the sources contained in the Diploma Thesis writing guide. I declare that, as far as I know, the content of this Thesis is the product of my own work and there are references to all the sources I have used.

The views and conclusions contained in this Thesis are those of the author and should not be construed as representing the official positions of the School of Mechanical Engineering or the National Technical University of Athens.

Aris Konstantinidis

Table of Contents

Acknowledgments 4
Table of Contents 6
Abstract 8
Περίληψη 9
1. Introduction 10
2. Literature review 12
3. Finite element model and benchmarks for the DCP 22
3.1. Bone model 22
3.2. Plate and screws model 27
3.3. Walking load model 28
3.4. Finite element analysis 31
4. Conceptual design 37
4.1. Technical specifications and selection criteria 37
4.2. Alternative solution list 40
4.3. Evaluation method 45
4.4. Feasibility study and final concept selection 47
4.4.1. Variable magnetic screws 47
4.4.2. Shape memory and superelasticity 49
5. Embodiment design 55
5.1. Superelastic compression plate 55
5.1.1. Screw slot configuration 55
5.1.2. Material properties and compression force 60
5.1.2.1. Mechanical properties 60
5.1.2.2. DCP compression force 64
5.1.3. Sliding inserts 69
5.2. Tensioning tool 70
5.2.1. Design specifications and conceptual design 70
5.2.2. Design and calculation of the tension tool 71

5.2.2.1. Tensile loading mechanism 72
5.2.2.2. Power Input 78
5.2.2.3. Supports and fixation 79
5.2.2.4. Gear components 81
5.2.2.5. Clamp 86
5.2.2.6. Additional complementary elements 88
5.2.3. Design and Calculation of the sustain Tool 88
5.3. Titanium case 90
5.4. Surgical procedure description for SCP installation 93
6. Conclusion 94
Table of figures 96
List of tables 99
List of images 100
List of references 101
Appendix I – Design drawings 105
Appendix II – Alternative solutions table with scores 106
Appendix III – Compression load cell specifications and program codes 111

Abstract

Compression plate osteosynthesis techniques have revolutionized the field of fracture treatment in the last 50 years, offering excellent clinical results in a variety of cases. However, they remain static fixations that are prone to compression loss over time, especially in the case of bone resorption. The goal of this study is the design of a true dynamic fixation device for long bone fractures based on superelasticity that is able to adjust the compression force as required. The steps of the design process are followed: study of existing solutions, conceptual design and embodiment design. A finite element model for the loading of a dynamic compression plate during walking is constructed, from which a maximum equivalent stress of 627 MPa and a minimum compression force estimate of 810N are deduced, confirming the relevant bibliography. The conceptual design involves an evaluation process based on the technical specifications, to determine the best among a list of alternative solutions. The potential of the superelasticity effect of Nitinol (Ni-Ti) as a prospective solution is revealed and subsequently examined. In the embodiment design stage, finite element models of loading and unloading, as well as physical tensile and bending tests, attest to the ability of Nitinol to achieve strain values of around 10% at failure and constant compressive stress for a large part of its superelastic rebound. The latter characteristic, inspires a design of a titanium case and a superelastic Nitinol compression plate (SCP), inserted into the case under tension and let to rebound and compress the fracture gap with approximately constant force. The proposed design shows encouraging signs towards mitigating the common compression plating problem and thus accelerating the healing process for fracture patients.

Περίληψη

Οι τεχνικές οστεοσύνθεσης με πλάκες συμπίεσης, έχουν φέρει επανάσταση στον τομέα της θεραπείας καταγμάτων τα τελευταία 50 χρόνια, προσφέροντας εξαιρετικά κλινικά αποτελέσματα σε ποικίλες περιπτώσεις. Ωστόσο, παραμένουν στατικές στηρίξεις που είναι επιρρεπείς στην απώλεια της συμπίεσης με την πάροδο του χρόνου, ειδικά στην περίπτωση της οστικής απορρόφησης. Ο στόχος αυτής της μελέτης είναι ο σχεδιασμός μιας πραγματικά δυναμικής συσκευής στερέωσης καταγμάτων μακρών οστών, βασισμένης στην υπερελαστικότητα που να είναι σε θέση να ρυθμίζει τη δύναμη συμπίεσης ανάλογα με τις ανάγκες. Ακολουθούνται τα βήματα της διαδικασίας σχεδιασμού: μελέτη υφιστάμενων λύσεων, εννοιολογικός σχεδιασμός και σχεδιασμός ενσάρκωσης (embodiment design). Κατασκευάζεται ένα μοντέλο πεπερασμένων στοιχείων για τη φόρτιση μιας πλάκας δυναμικής συμπίεσης κατά το βάδισμα, από το οποίο προκύπτει μέγιστη ισοδύναμη τάση 627 MPa και εκτίμηση ελάχιστης δύναμης συμπίεσης 810 N, επιβεβαιώνοντας τη σχετική βιβλιογραφία. Ο εννοιολογικός σχεδιασμός περιλαμβάνει μια διαδικασία αξιολόγησης με βάση τις τεχνικές προδιαγραφές, για τον προσδιορισμό της καλύτερης από μια λίστα εναλλακτικών λύσεων. Η δυναμική του φαινομένου υπερελαστικότητας της Νιτινόλης (Ni-Ti) ως πιθανής λύσης αποκαλύπτεται και στη συνέχεια εξετάζεται. Στο στάδιο του σχεδιασμού ενσάρκωσης, μοντέλα πεπερασμένων στοιχείων φόρτισης και εκφόρτισης, καθώς και πειραματικές δοκιμές εφελκυσμού και κάμψης, πιστοποιούν την ικανότητα της Νιτινόλης να επιτυγχάνει τιμές παραμόρφωσης περίπου 10% στην αστοχία και σταθερή θλιπτική τάση για μεγάλο μέρος της υπερελαστική επαναφοράς της. Το τελευταίο χαρακτηριστικό, εμπνέει ένα σχέδιο μιας θήκης από τιτάνιο και μιας υπερελαστικής εσωτερικής πλάκας Νιτινόλης (SCP), που εισάγεται στη θήκη υπό τάση και αφήνεται να επαναφερθεί και να συμπιέσει το διάκενο του κατάγματος με περίπου σταθερή δύναμη. Ο προτεινόμενος σχεδιασμός δείχνει ενθαρρυντικά σημάδια για την άμβλυνση του κοινού προβλήματος των πλακών συμπίεσης και επομένως την επιτάχυνση της διαδικασίας ανάρρωσης για τους ασθενείς με κατάγματα.

1. Introduction

The concept of internal fixation has been a staple of orthopedic surgery for at least a century, even though documented efforts of surgical stabilization of fractured bones date even earlier. The developments of internal fixation techniques presented a revolution in fracture treatment. With the use of older fixation techniques (such as splinting and casting), severe fractures often led to amputation, due to extensive damage of soft tissues and sepsis. The term "internal fixation" refers to a surgical procedure that stabilizes and joins the ends of fractured bones by mechanical devices such as metal plates, pins, rods, wires or screws. The main goals of the procedure are achieving structural stability and recovery of function in a short time span, promoting healing of the fracture, through the creation of new bone tissue (osteosynthesis) and preventing infection through meticulous antiseptic measures [1].

The most prominent method of internal fixation for long bones is plating, where a rigid stainless steel or titanium plate is attached to the fractured bone with screws. At present, there is a multitude of plate designs available in various shapes, sizes and configurations allowing for the treatment of a vast assortment of fracture types. The main types of plates used currently are the dynamic compression plate (DCP) and the locking compression plate (LCP). The former bases its function on achieving rigidity at the fracture site through axial compression of the bone fragments and the latter offers rigidity by thread connection with the plate body. The combinations of both types have been very successful in treating the vast majority of fracture cases, however they remain essentially static fixations with no adjustment capability and thus have limited efficiency in cases of extensive bone resorption or other non-union types, where the interfragmentary gap widens over time. In such cases, the compression at the fracture site is reduced or even nullified, which greatly reduces rigidity and leads to numerous problems. Notably, common problems are the delayed healing due to the excessively wide gap which is not conducive for primary bone union and the high risk of plate failure due to increased stress concentration at the fracture site [2]–[4].

The goal of this study is the design of a true dynamic fixation device that is able to achieve almost constant compression at the fracture site irrespective of bone tissue loss. In this way, the healing process is accelerated and the patients can return to their normal activities much sooner and with minimal complications, even in challenging fracture cases. The proposed solution consists of a titanium case and a semi-active compression adjustment mechanism based on superelasticity. It utilizes the large strain and subsequent superelastic effect of superelastic Nitinol to offer sustained compression over the course of the fracture healing. The design attempts to preserve all the advantages of the DCP and to mitigate the effect of compression loss in the fracture site.

Before installation, the superelastic component of the plate is elongated under a specific load and is placed in the plate under pretension. When fixed with screws on the bone fragments, the superelastic plate is let free to rebound and thus compress the fragments together. For every widening of the fracture gap, the plate is able to provide instant corrective compression with approximately constant force. Moreover, the compression load can be accurately set by the surgeon, in contrast to the empirical techniques used at present, therefore the probability for complications during the healing process is minimized. All in all, with the use of the novel plate the parameters of the surgical installation are quantified and are easily reproducible with increased reliability. The adjustment mechanism is non-invasive and doesn't require a secondary procedure after the initial operation.

In this study, the design process of the novel superelastic compression plate is described. The first chapter is a short literature review describing the main turning points and milestones in the history of fixation plates, with an emphasis on long bone plates. Subsequently, a finite element model of a regular DCP is constructed, in order to simulate the behavior of the plate in the worst-case condition of maximum walking load and thus assess the critical points that could be subject to failure. The main body details the design stages in two chapters covering the conceptual design and the embodiment design. In the conceptual design section, all alternative solutions and the evaluation method with criteria for the selection are described, the best solutions are selected and further primary concepts are developed for each one. The concepts are subsequently evaluated with simple calculations, in terms of feasibility and efficiency. Finally, the embodiment design process for the final solution is presented, with detailed calculations and descriptions for all aspects of the design. The study concludes with a discussion section, in which the main conclusions, advantages and drawbacks and potential for further improvement and research are critically discussed, with reference to the existing literature and common medical practice.

2. Literature review

The progress of plating technologies and methods throughout the years is based on the biological advancements in understanding the bone healing mechanism, as well as the evolution in engineering and material science. The combination of the knowledge in both fields has culminated in numerous plate designs in the last 130 years, contributing to the development of modern internal fixation. In the following review, the focus is on citing the main points in the history of fracture healing research and relating the findings to plate designs conceived to apply them in a clinical setting, as well as assessing their efficiency and their overall impact on patient recovery and quality of life.

The knowledge of the basic biology of fracture healing is first attributed to John Hunter, who described the process of natural bone repair in four stages: inflammation, soft callus, hard callus and remodeling [5]. Succeeding Hunter, the work of Belchier and Goodsir on the contribution of osteoblasts in bone creation [6] and later research of McEwen and Ollier on the importance of the blood-vessel-rich periosteum in bone regeneration led to a more complete understanding of the healing mechanism by the end of the 19th century. In the following years and until 1950, more knowledge on the role of specialized cells and blood supply of surrounding soft tissues emerged and complemented the repair model known today as secondary or indirect bone healing [7].

a. Inflammation

Occurs shortly after injury and has the same characteristics as in soft tissues (erythema, swelling, increased temperature and pain). The blood supply in the fracture area is disrupted and blood clots can form. The inadequate blood supply, leads to necrosis of the bone and surrounding tissues, especially in the fragment ends. Soon a hematoma is created and starts the essential cellular processes for tissue regeneration. The inflammatory stage ends with resorption of dead bone and the creation of a transient granulation tissue that contains modulated mesenchymal cells, essential for tissue regeneration (chondroblasts, fibroblasts and osteoblasts) [1], [7].

b. Soft callous

Chondroblasts and fibroblasts activate and form an initial callous tissue in a grid formation around the fracture site. The resulting tissue is a combination of cartilage and fibrous tissue and has relatively low strength. However, it provides a degree of structural stability around the fracture gap [1], [7], [8].

c. Hard callous

Following the soft callous stage, cartilage is calcified and then resorbed by chondroclasts. Subsequently, chondroclasts differentiate to form osteoblasts, which create primary bone tissue. At

the end of the hard callus phase, the fibrocartilage of soft callous has been replaced with fibrous bone. The shape of the callus is irregular and increased in volume in comparison to healthy bone. In this form, the strength of the bone is considerably lower, in comparison to the healthy state, therefore the danger of refracture is increased [1], [7], [9].

d. Remodeling

During this phase, fibrous bone is replaced with lamellar bone with the action of the basic multicellular unit, a combination of osteoclasts, progenital cells that differentiate into osteoblasts, capillaries and other cells. The BMU first replaces all the hard callus with fully functional bone of normal mechanical properties and then reduces the volume of the structure in an effort to recover the original bone shape. The remodeling phase is long, requiring 1 to 4 years to complete, during which the bone hasn't recovered the full mechanical properties of its healthy state, however the probability of refracture is increasingly low [7], [10].

In 1949, Robert Danis' experimentation with compression in the fracture site, led to the discovery of a new type of bone healing, called then “autogenous welding” and known today as primary or direct bone healing. It has to be noted, that this process does not occur naturally and is only possible if the fracture ends are compressed together and rigidly connected [3], [11]. In this case, no or minimal callus is formed, as the bone passes immediately to the remodeling phase. Necrotic bone tissue at the fracture ends is resorbed and remodeling units of endothelial and progenital cells (cutting cones), that create new blood vessels and osteoblasts. The produced osteoblasts bridge the interfragmentary gap producing bone tissue, in areas where the two fragments are in contact. In areas where small gaps still exist, fibrous bone is created, to then be converted into lamellar bone over time, as in the remodeling phase of secondary bone healing [7].

Modern research has revealed more information on how molecular processes controlled by hormones and genetic factors influence the healing process, however such theories are beyond the scope of this study. The understanding of the bone healing process and mechanisms dictated the internal fixation designs and surgical techniques throughout history. To this day, Hunter's four-stage model of indirect bone healing still serves as a guide for flexible fixation and fixation of comminuted and non-union fractures that aim at creating callus around the fracture site. On the other hand, Danis' discovery of direct bone union set the base for compression plating and relevant techniques applied in simpler long bone fractures. It is apparent, that from an engineering standpoint, the designs must follow the latest advancements in bone healing research and utilize the findings in an effective way. Despite the progress, many influencing factors of osteosynthesis remain unknown, thus limiting the potential of internal fixation. Thorough understanding of the biological mechanisms and subsequent creative designs can contribute to reducing recovery time for patients and avoiding post-operational complications [7].

The first reference to plates for long bone fixation was made in 1886 by Carl Hansmann in Heidelberg, who used nickel-coated steel plates (Image 2.1) in 20 discrete cases, with success [12]. In 1895, Lane presented another early plate design (Image 2.2), which was later discontinued due to problems with corrosion [13]. Other historically significant designs are those of Lambotte (Image 2.3) [14], Sherman [15] and Groves.

Image 2.1 – Hansmann's plate set [4]

Image 2.2 – Lane's plate design [2]

Image 2.3 – Lambotte's plate design [2]

Despite the improved corrosion resistance, all these newer designs suffered due to strength limitations resulting in failure of the implants. The new plate fixation solutions were able to solve several problems of the past and were applied increasingly often with some success, however

they were still in a premature phase and faced numerous shortcomings. Even though the achievement of effective asepsis during the surgical procedure remained a challenging task, it became apparent that the engineering was equally or even more problematic. The understanding of the biology and biomechanics of osteosynthesis was still scarce, resulting in ineffective designs. Moreover, the aforementioned pioneers of plating osteosynthesis were general surgeons, not solely preoccupied with research and practice on internal fixation, which in combination with their eventual retirement didn't leave a rich enough body of work to their successors. The latter, lacking adequate knowledge of the principles and techniques, were responsible for many costly failures that swayed the consensus of specialists away from internal fixation and back to more conservative methods. These developments led to a 30-year period of inactivity on the front of internal fixation research, until the end of the 1940s marked a new breakthrough, which was to introduce the basic ideas of modern-day osteosynthesis techniques [16].

The first effort to amend bone resorption was made by Eggers [17], who designed a two-slot plate that permitted sliding of the screws, bringing the bone fragments together. The design was abandoned due to strength limitations. In 1949, Danis revolutionized plate fixation by designing the “coapteur”, the first compression plate (Image 2.4), aiming at compressing the fragment ends together and fixing them rigidly. The compression is made possible with the use of an adjusting screw on the side of the plate. This design resulted in the healing mode known as direct bone union, without callus formation and inspired many later designs [11]. Another groundbreaking design was proposed by Bagby and Janes in 1958 who designed a plate with oval holes and sloped sides (Figure 2.1), able to provide compression by tightening the screws [18].

Image 2.4 – Danis’ “coapteur” plate, the first compression plate [2]

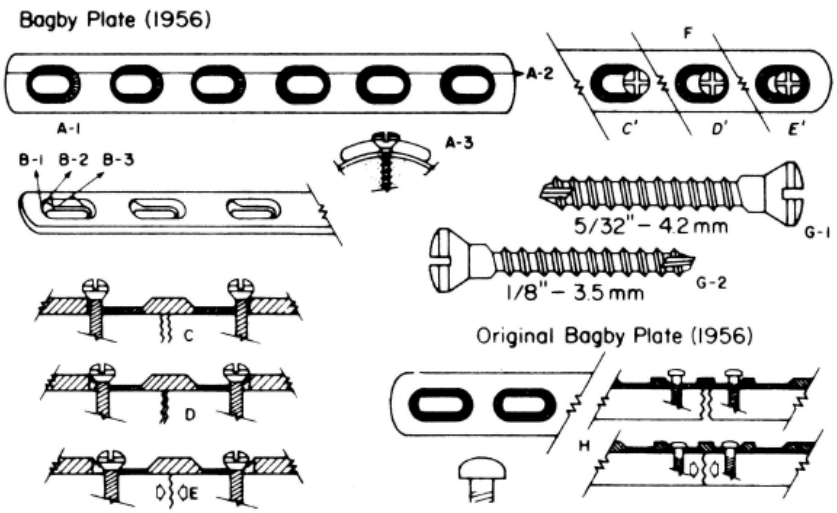

Figure 2.1 - Bagby and Janes' compression plate [2]

In 1965, Muller, Allgower and Willenegger, founding members of the well-known Swiss group of orthopedic surgeons AO (Arbeitsgemeinschaft für Osteosynthesefragen), created a design that achieved compression with the aid of an external temporary tensioning device. A screw-lever system is attached to the bone and the plate, preloads the plate until the fragment ends are compressed and is subsequently removed [19]. It has to be noted that since its inception in 1958, the AO organisation had devised a complete set of conventional non-compression plates. The AO group has been at the forefront of advancements in internal fixation until today and its contribution to the development of the modern principles of internal fixation is invaluable. Concerning their aforementioned compression plate design, the tensioning device was eventually discontinued, using instead a solution with oval holes, similar to the design of Bagby and Janes. The Swiss surgeons did not acknowledge the preceding solution and claimed to have developed the design independently [2], [3]. Finally in 1967, Schenk and Willenegger, presented a new design, drawing reference from the compression principle of Bagby and Janes. The design was similarly based to oval screw holes, however the side slopes were revamped, having the shape of part of a slanted cylinder. The new device, named the dynamic compression plate (DCP) ensured axial translation when tightening eccentrically placed screws [20]. The screw heads slide along the pathways created by the hole sides and move axially (Figure 2.2), together with the bone fragment, as they are bound to it with the thread. In this way, the bone fragments are moving relative to one another, until the fracture gap closes and compression is achieved. With symmetrical holes on each side of the fracture, the surgeon can achieve movement bilaterally and control the level of compression as desired.

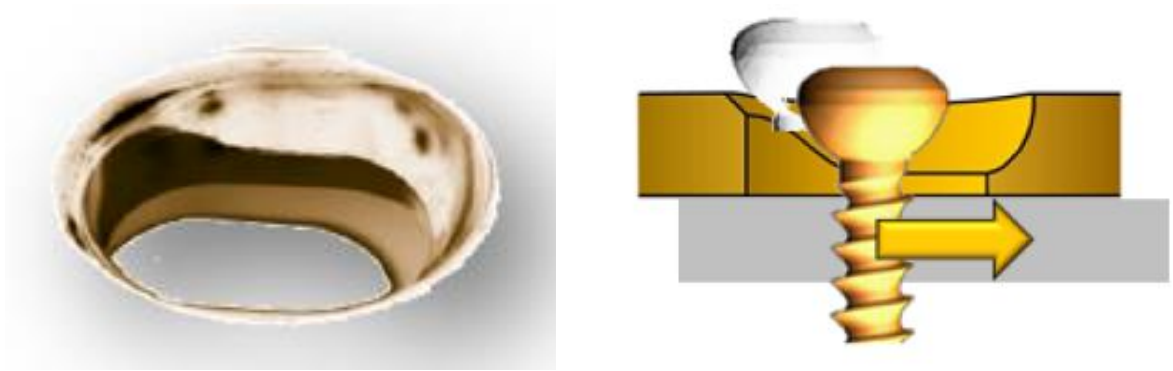

Figure 2.2 - DCP holes form and function [4]

The DCP was a revolutionary and successful design, offering multiple advantages and signaling the passage to the modern era of plate fixation, as after its conception it became the standard for plate fixation. Most importantly, the probability of misalignment and insufficient closing of the gap at the fracture site is greatly reduced and the rigidity of the fixation provides stability, allowing restoration of movement soon after the surgery. Dynamic compression plates (Image 2.5) have been extensively utilized in operations to this day and the results are very positive.

Image 2.5 – Modern dynamic compression plate (DCP) [21]

Nonetheless the large sample size also unveiled the shortcomings of the design, which presented opportunities for improvement. The main disadvantages observed were the inability to assess the healing process with x-ray scanning, the loss of bone on the undersurface of the plate with subsequent refracture danger and the delayed union in cases of increased bone resorption at the fragment ends during the healing [2]. The first problem is owed to the primary bone union

achieved with rigid compression plates, which doesn't produce any callus to be assessed radiologically, while the fracture gap is also invisible. When it comes to bone loss, a lot of discussion has been made as to the causes and consequences of the phenomenon. The most common result associated with bone loss is refracture of the bone after the removal of the plate, usually happening after 18-24 months after the initial fracture. Examination of the refractured bones usually shows reduction in cortical bone tissue and failure in areas of malunion. Perren and his research team attributed the bone loss to excessive contact between the underside of the plate and the periosteum. They hypothesized that increased friction in metal to bone contact and excessive compressive force in the radial direction due to screw tightening deprived the periosteum of the necessary blood supply and led to necrosis of the bone tissue. As a result, the remodelling process activated to replace the necrotic cortical tissue with new bone tissue caused increased porosis and diminished strength. The proposed solution, published in 1992 [22] and implemented in 1994, was a new plate, called the limited contact-dynamic compression plate (LC-DCP) with strategically placed notches on the underside of the plate between the screw holes resulting in 50% reduction of the plate footprint and thus a decrease in contact area between the plate and the bone (Figure 2.3).

Figure 2.3 - Comparison of footprints in DCP and LC-DCP [4]

However, the LC-DCP quickly came under scrutiny by a number of researches refuting the claims of Perren and his colleagues and offering alternative explanations. The term stress shielding refers to the reduction in density (osteoporosis) of cortical bone tissue as a result of stress deprivation induced by a rigid fixation device. According to Wolff's law, cortical bone adapts and remodels itself, according to the loads it is subjected to. In surgical fixation of a fracture, the stresses are redirected from the bone to the rigid fixation device, thus depriving the bone of the load-induced remodeling and reducing its volume. Uhthoff et al. [23] hypothesized that osteoporosis of cortical tissue under a compression plate is a result of stress shielding, rather than plate-bone contact. To assess their claim, they compared regular DCPs with railed limited contact plates as to necrosis and porosis in the periosteum end endosteum of cortical bones. As expected, more extensive necrosis was observed in the periosteal portion, however the degree of porosis

was interestingly greater in the endosteal portion. Moreover, the degree of necrosis was virtually identical between the two plate groups. These findings refute both contact area-necrosis and necrosis-porosis correlations and indicate the stress shielding effect to be more significant. The notion was supported by an earlier study, that concluded on cortical tissue porosis and widening of the medullary canal as a result of rigid plating or external immobilization [24]. Also notably, Jain et al. [25] performed measurements of blood flow in cortical tissue of canine tibias in a control group fixed with DCPs and a group fixed with LC-DCPs, concluding to no significant difference between the two groups. Around the same time, the concept of biological fixation emerged, thanks to the contributions of Gerber and Gainz [26]. This refers to a less rigid fixation, aimed at minimizing soft tissue injury around the fracture. An expansion to the idea presented the initiation of secondary bone union and callus formation as desirable for faster and stronger healing, achievable through a flexible fixation with no interfragmentary compression, to allow for micromotion, small relative movement between the bone fragments. This fixation principle produced new less rigid designs, such as the point-contact fixator (PC-Fix), a plate with almost no contact with the bone, fixed by monocortical as opposed to bicortical screws (shorter cortex screws that grip only the top part of cortical bone and end inside the medullary canal) which are locked into the plate [27]. These plates were soon abandoned, but they became the predecessor of the locking compression plate (LCP) which appeared in 2001. The same cortical screws are used, with the difference that their heads are threaded or are locked in place by a threaded nut screwed onto the female thread of the screw holes. Depending on the configuration, the screws can be placed at an angle to increase stability of the fixation. The LCP provides a more flexible fixation than the DCP and offers excellent pullout resistance, amending the common problem of sequential pullout of the screws under load and subsequent failure of the fixation. Moreover, it responds excellently to shear loading. The design retains the characteristics of the DCP with the use of combination holes (Figure 2.4). This gives the ability to the surgeon to use the plate as per case, making use of both principles for a better result. It has to be noted, that such combinations can be very challenging and must be approached with caution. [4]

Figure 2.4 - Combination holes in the locking compression plate (LCP) [4]

As a whole, biological fixation principles, as the name suggests, focus more on the biological aspect of healing, rather than the mechanical. The focus is set just on proper alignment of the fragments and not on absolute stability, as in traditional compression plating. This relatively new theory produces reliable fixation and good healing results, though not without the absence of caveats. Each fracture case is different and requires the appropriate management. In cases where injury to soft tissues is minimal and blood supply is mostly intact, flexible fixation with callus formation appears as the most advantageous course of action for faster healing time, however other cases characterized by severe disruption to the blood flow around the fracture site are still better treated with rigid compression fixation, as extensive necrosis and bone resorption lead to increased remodeling time. Another challenge is assessing the maximum instability threshold for a fracture. In flexible fixations some degree of instability is desired, however above a certain limit, instability can be detrimental to both fracture healing and structural integrity of the fixation. [28]

In recent years, there has been research addressing the shortcomings of the aforementioned designs, focusing on different questions and suggesting improvements, but no new design has been widely utilized and replaced the current DC and LC plates. Uhthoff et al. [2] proposed a new approach to combat stress shielding, that of dynamic loading and micromotion in the axial direction. This is made possible by a polymethylmethacrylate (PMMA) insert between the screw heads and screw holes that can be compressed under load and exhibit elastic recovery after unloading. An attempt at improvement by replacing the PMMA inserts with bioresorbable ones constructed by polylactic acid (PLA), proved unsuccessful due to premature failure. In general, biodegradable fixation is advancing, with increasing research for biodegradable materials, mainly polymers, and efforts to apply such fixation devices. In theory, the devices can be resorbed by the body, so no removal procedure is necessary and load is progressively transferred back to the healed bone. The considerable strength limitations of those plates however, limit them to only specific low-stress applications.

More recently, efforts have been made to test plates constructed from polyetheretherketone (PEEK) and other plastics and compare their behavior and properties to traditional stainless steel and titanium plates. These materials offer the advantage of similar elastic modulus to bone, thus supposedly reducing stress shielding and surpassing metal plates in fatigue strength. In practice, the concept is problematic due to the existence of the fracture gap which acts as a stress riser. The strength of plastic plates is still simply inadequate, especially for use in compression fixation and eventually the plates fail. An improvement on those designs has been proposed by the Italian group of Padolino et al. [29] and uses carbon fiber reinforced PEEK (CFR-PEEK). The plates were tested in 21 patients with proximal humerus fractures and produced similar clinical results and decreased bone necrosis in comparison to a control group treated with metal plates, at the expense of increased stress shielding in cortical bone tissue on the underside of the plate. Presently,

osteosynthesis plates are available in a multitude of shapes and sizes, offering versatility, as they can be used in different bones and locations.

Despite its name, the DCP is only capable of one-time dynamic compression during its installation. During the healing process, not only it does not allow micromotion in the fracture gap, but it is actually susceptible to complete loss of compression, in case of bone resorption between the fragment ends. This fact isn't necessarily problematic if the fracture gap remains small; notwithstanding, there are cases of severe resorption, where the fragment gap can widen up to 8mm. In this case, the stresses on the plate rise considerably, undermining its durability and more importantly delayed union on non-union is common, as the distance between the fragments is too large to be bridged. In such cases, the recovery time significantly increases and even a follow-up procedure may be required for the fracture to heal. So far, there hasn't been a design that addresses all these shortcomings effectively. As mentioned, increased emphasis in research is placed on micromotion, with the prevalence of the biological osteosynthesis theory, however the fracture gap expansion problem has not yet been resolved. Moreover, exact force metrics for screw pretension and axial compression are not widely available as results of concrete experiments.

Therefore, the proposed design in this study is a non-invasive or minimally invasive fixation that provides true dynamic compression maintaining a constant compression force, accounting for bone tissue loss due to resorption. Auxiliary, experiments quantifying various parameters of the surgical process for installation of bone plates can provide a better understanding of the impact of surgical techniques and practices on healing and can contribute to streamlining the procedure, reducing the dependence on surgeon experience and skill for achieving optimal results.

3. Finite element model and benchmarks for the DCP

In order to identify the critical points on the plate body and to analyze its behavior during regular use, a simple finite element model for the DCP under load is constructed. The selected long bone that the model is going to be based on is the femur, the largest bone of the human body, which absorbs a substantial load, since it is located in the lower extremities and bears the weight of the patient in standing. The modeling process is described further down and can be divided into three sections: bone model, plate and screws model, walking load model.

3.1. Bone model

In modeling the bone, it is required to create a three dimensional model of the bone volume and apply an appropriate mesh. The model is based on a series of DICOM images derived from a CT scan of a healthy left femur bone of an 81 year old male patient. The images are imported into 3D Slicer, an open source software platform for medical image processing. In order to extract a model for the femur from the complete CT scan data, segmentation techniques must be used to identify the bone tissue and differentiate it from the surrounding soft tissues. Common segmentation methods in imaging include:

a. Region based methods: Separate the objects into different regions based on some threshold value
b. Edge based methods: Make use of discontinuous local features of an image to detect edges and hence define a boundary of the object
c. Clustering based methods: Divide the pixels of the image into homogeneous clusters
d. Watershed based methods: Treat the image like a topographic map with the brightness of each point representing its height and identify the contours to separate overlapping objects
e. Convolutional neural networks (CNN): A network architecture for deep learning which learns directly from data, eliminating the need for manual feature extraction. They are particularly useful for finding patterns in images to recognize objects, faces, and scenes.
f. Volume rendering: A collection of methods to create a 2D projection from a discretely sampled 3D data set [30]

The most preferable methods for medical imaging are the CNNs and volume rendering. On this occasion, the methods used are volume rendering and thresholding, as described below. In the Slicer interface, the DICOM images are displayed in three views for the transverse, saggital and coronal plane and the three-dimensional volume model that results from the combination of the images is displayed on a separate view. For reference, the definitions of reference planes in anatomy are presented in Figure 3.1. The transverse plane divides the body into superior (top) and

inferior (bottom) portions, the saggital plane divides it into left and right portions (areas away from the craniocaudal axis are called lateral and towards the axis are called medial) and the coonal plane divides it into ventral (front) and dorsal (back) portions.

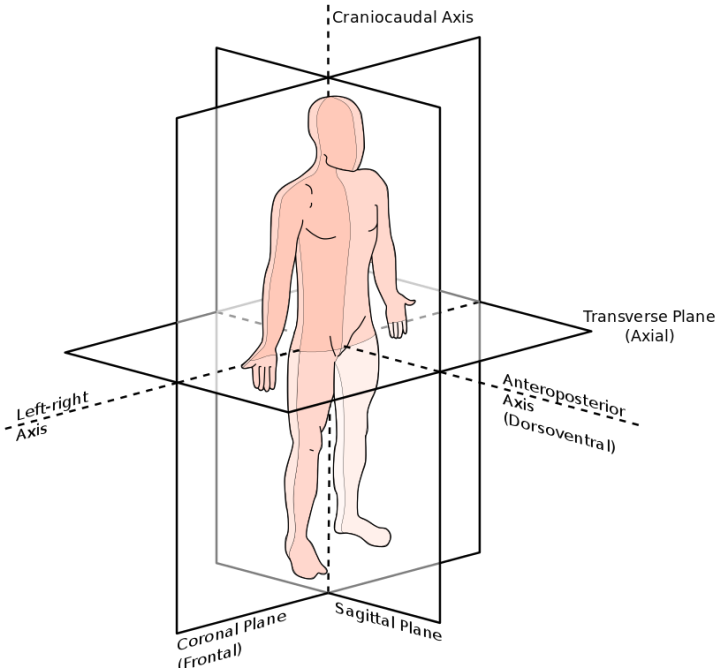

Figure 3.1 – Anatomical planes and axes of the human body

The volume rendering module is selected and the full CT data are cropped using the crop module, to form a rectangular volume that encloses the left femur (Image 3.1).

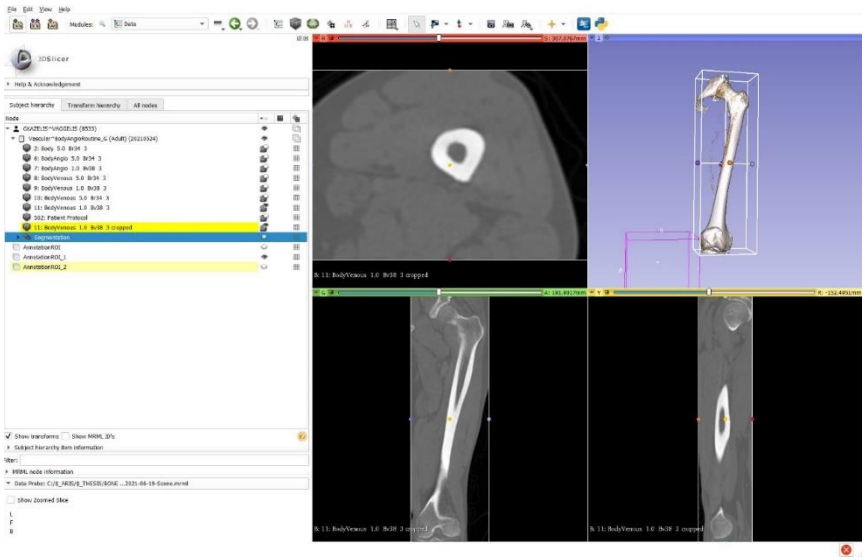

Image 3.1 – The interface of the 3D Slicer software

Subsequently, the editor module is used with parameters for the threshold tool as shown in Image 3.2, which permits the identification of the bone with respect to surrounding bone tissues. The bone tissue is automatically crudely painted in green, whereas the rest of the structures remain unmarked. The resulting segment contains, excluding the desired femur, part of the knee cap, acetabulum and pelvis, whereas the femur body is not solid, but displays holes. To correct the imperfections, the threshold tool incorporates the Paint and Erase effects for manual marking of the desired tissue. This corrective marking is executed for each individual picture in every direction until an adequate volume render of the femur is produced. The render is then exported as a model in .stl format and is available for post-processing.

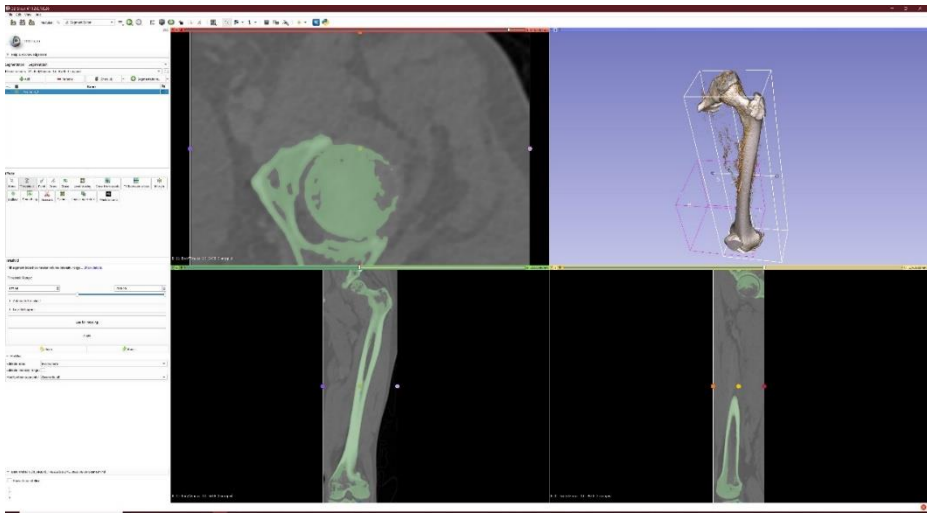

Image 3.2 – Bone tissue thresholding in the 3D Slicer interface

This initial model still contains errors, such as surface bumps and holes, due to inaccurate segmentation. In order for it to be used for FEA purposes, the surface has to be smoothed and the holes should be filled. The post-processing is performed using the open source software Meshmixer (Image 3.3). The Draw and Pinch brushes of the software are used in combination to fill the holes on the surface, whereas the Flatten and BubbleSmooth brushes aid in smoothing. For each part of the femur, the parameters of Strength, Size and Depth are modified according to the size and complexity of the structures and the level of processing required.

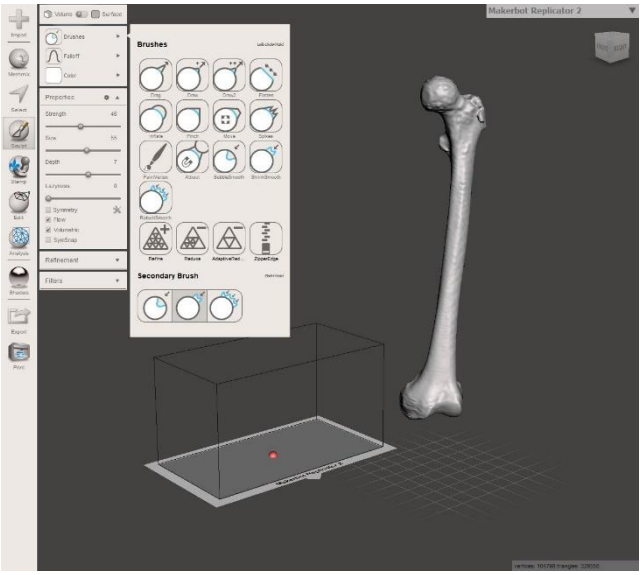

Image 3.3 – The interface of the Meshmixer software

The femoral head, neck and trochanter areas require smaller brushes and more accurate application of the tools, while the condyle, epicondyle and particularly the femoral shaft are already of acceptable quality and only need minor modification with larger, less accurate brushes. After the completion of the post-processing procedure, the modified model is exported to use in the FEA. Image 3.4 offers a comparison between the models before and after smoothing.

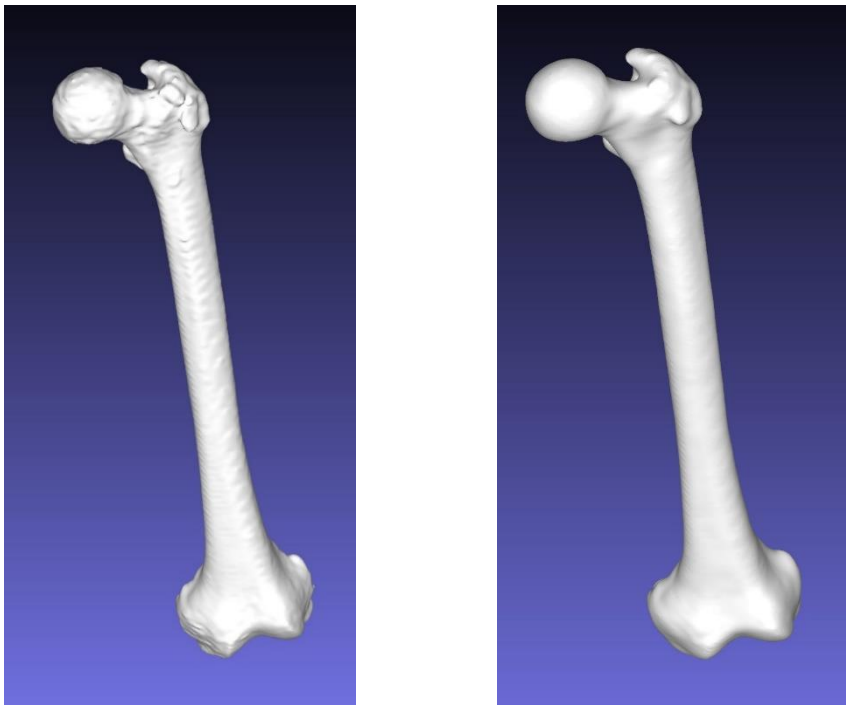

Image 3.4 – Comparison of the initial and the smooth femur model

The smooth model is imported into Ansys Workbench. Using the SpaceClaim software, the model is simplified with triangle merging to reduce complexity and thus calculation times. To simulate a typical transverse and non-displaced fracture, the model is divided into two parts by a transverse intersection plane, at the midpoint of the femoral shaft and suitable 4.5mm screw holes are opened (10 holes bilaterally and symmetrically to the fracture gap) as displayed in Images 3.5.

Figure 3.2 - Femur model with holes in the ANSYS Spaceclaim interface

The material assigned to the model will correspond to cortical bone tissue, as the properties of bone marrow inside the medullary canal have negligible effects on the result and the femoral shaft does not contain trabecular bone tissue. The cortical bone is modeled as orthotropic and more specifically is transversely isotropic, as it has the same properties across all directions of the transverse plane and different properties in the longitudinal direction. The properties are derived from the research of Morgan et al. [31] and are displayed in Table 3.1.

Table 3.1 – Material properties of cortical bone tissue in the ANSYS Workbench interface

Properties of Outline Row 3: Bone

	A	B	C	D	E
1	Property	Value	Unit		
2	Material Field Variables	Table			
3	Density	1.9	g cm^-3		
4	Orthotropic Elasticity				
5	Young's Modulus X direction	10100	MPa		
6	Young's Modulus Y direction	10100	MPa		
7	Young's Modulus Z direction	18030	MPa		
8	Poisson's Ratio XY	0.4			
9	Poisson's Ratio YZ	0.3			
10	Poisson's Ratio XZ	0.3			
11	Shear Modulus XY	4000	MPa		
12	Shear Modulus YZ	3300	MPa		
13	Shear Modulus XZ	3300	MPa		
14	Orthotropic Stress Limits				
15	Tensile X direction	53	MPa		
16	Tensile Y direction	53	MPa		
17	Tensile Z direction	135	MPa		
18	Compressive X direction	-131	MPa		
19	Compressive Y direction	-131	MPa		
20	Compressive Z direction	-205	MPa		
21	Shear XY	65	MPa		
22	Shear YZ	65	MPa		
23	Shear XZ	65	MPa		

3.2. Plate and screws model

The plate model is based on a typical 10-hole narrow DCP (Figure 3.3) and the screws are 4.5mm diameter, 42mm length cortical bone screws, in line with the relevant standardization specified in **ISO 5835:1991**. The complexity of the accurate models can be reduced without loss of accuracy, as far as the screws and slots are concerned, therefore the following simplified models are constructed. The material assigned for both plates and screws is a Grade 5 Titanium alloy (Ti-6Al-4V) used in medical applications, with the properties displayed in Table 3.2 at body temperature (37°C).

Figure 3.3 - 10-hole narrow DCP model

Table 3.2 - Material properties of Grade 5 Titanium alloy (Ti-6Al-4V) in the ANSYS Workbench interface

Properties of Outline Row 6: Titanium Alloy

	A	B	C	D	E
1	Property	Value	Unit		
2	Material Field Variables	Table			
3	Density	4620	kg m^-3		
4	Isotropic Secant Coefficient of Thermal Expansion				
6	Isotropic Elasticity				
7	Derive from	Young's ...			
8	Young's Modulus	96000	MPa		
9	Poisson's Ratio	0.36			
10	Bulk Modulus	1.1429E+11	Pa		
11	Shear Modulus	3.5294E+10	Pa		
12	Tensile Yield Strength	930	MPa		
13	Compressive Yield Strength	930	MPa		
14	Tensile Ultimate Strength	1070	MPa		
15	Compressive Ultimate Strength	1070	MPa		
16	Isotropic Thermal Conductivity	21.9	W m^-1...		
17	Specific Heat, C_p	522	J kg^-1 ...		
18	Isotropic Relative Permeability	1			
19	Isotropic Resistivity	1.7E-06	ohm m		

The plate is placed on the lateral portion of the femur, according to the tension band principle. As the joint load is placed eccentrically with respect to the mechanical axis of the femur, the lateral portion of the bone is loaded in tension, while the medial is loaded in compression. If the plate is fixed on the lateral cortex, the tension load is absorbed and the load on the bone becomes compressive on both sides, therefore the fracture site is stabilized. In other words, the compression achieved by the screws of the DCP is complemented by the load and the resistance of the bone in compression is utilized to provide stability. If the plate was applied to the medial portion, the fracture gap in the lateral portion would immediately widen, since the resistance of a fractured bone to tension is non-existent. Such loading conditions would lead to instability and inevitable failure of the plate. [1], [4]

3.3. Walking load model

The loading condition applied to the model is the maximum load of a normal walking cycle on the femur, as a representation of the worst-case scenario load the plate can receive under normal circumstances. In gait analysis, the gait cycle for each foot is defined as the time between consecutive heel strikes. The initial contact is defined as the beginning or 0% of the cycle and the end of the terminal swing is defined as the end or 100% of the cycle, while each intermediate point of the cycle is annotated with a percentage of the full cycle. The cycle is divided into the stance phase, when the foot is on the ground (approximately 60% of the cycle) and the swing phase, when the foot is lifted (approximately 40% of the cycle). In modern gait terms, the stance phase is divided into three sub-phases: the loading response, mid-stance and terminal stance, whereas

the swing phase is divided into four sub-phases: the preswing, initial swing, mid-swing and terminal swing. [32]

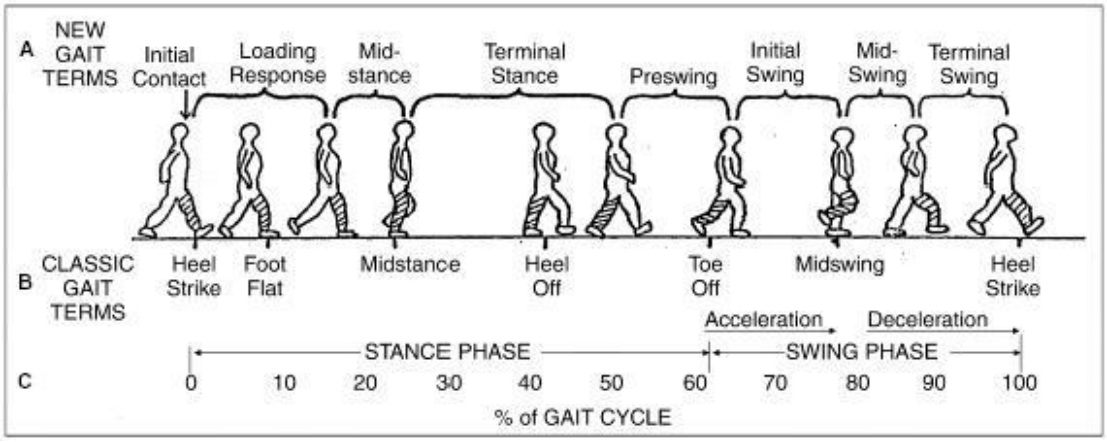

Figure 3.4 – Gait cycle phases and terms [32]

The maximum load on the femoral head is observed in the end of the loading response sub-phase, at 16% of the cycle and is estimated to be between 238-404% of a person's bodyweight (BW) for normal walking [33]–[36]. As far as the muscle forces on the femur are concerned, a total of 28 muscles generate force during walking (Figure 3.5).

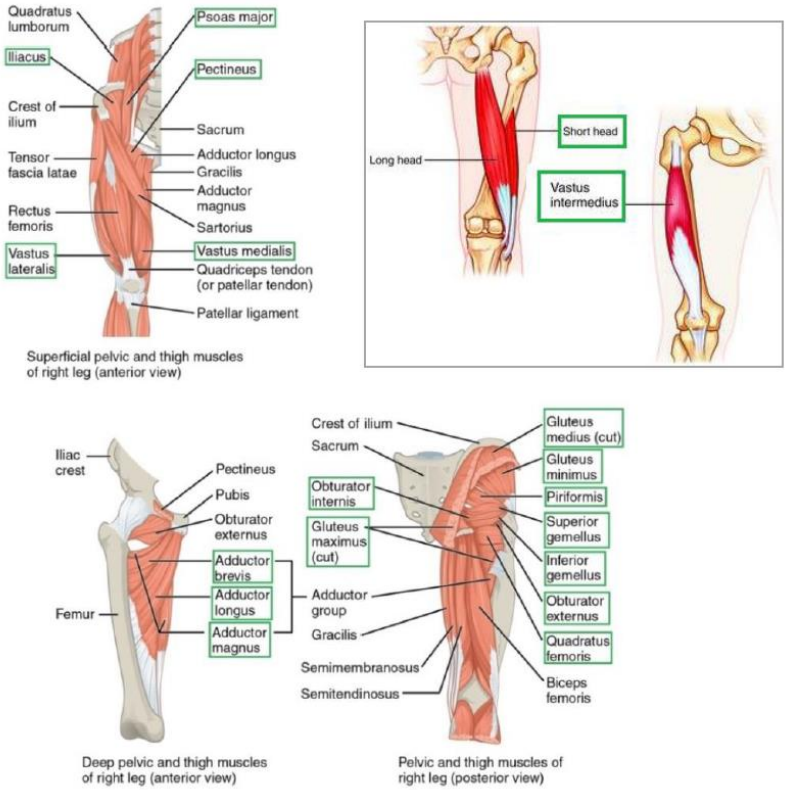

Figure 3.5 – Pelvic and thigh muscles of the human body [37]

For simplicity of the model, given the magnitudes of the muscle forces at 16% of the gait cycle, only the three major muscle groups with the largest effects are modeled: the abductors (comprised of the gluteus medius, gluteus minimus and gluteus maximus), quadriceps (comprised of the vastus lateralis, vastus intermedius and vastus medialis) and the iliopsoas (effectively the psoas major for the gait phase in question). The respective forces of the muscles are calculated in the relevant literature in the range of 104-158% BW for the abductors, 58-95% for the quadriceps and 20-32% BW for the iliopsoas [33], [35], [37]. Studies performed on older adults, usually after operations such as hip transplants, place the forces on the lower end of the spectrum and newer studies performed on young healthy adults report results compatible with the higher values. Given the fact that a typical load on a compression plate before healing of the femur (i.e. with a fracture gap present) is not expected to resemble that of a person walking at full capacity, it is considered logical to assume lower values. Besides that, the newer studies (many of which have not been performed in vivo, but are numerical) have been criticized for overestimation of the forces due to simplifications. The assumed bodyweight is that of an average male, at 75 kilograms.

The force vector for the joint force is placed on the femoral head area that is inserted in the hip socket and contacts the acetabulum and at an angle with the saggital plane of 13° laterally and with the coronal plane at 3° posteriorly. The force vectors for the muscle forces are placed on the femur model in the positions of the respective muscle insertions: the greater trochanter for the abductors, the intertrochanteric line for the quadriceps and the lesser trochanter for the iliopsoas and at respective angles with the saggital plane of 20° medially, 0° and 9 degrees medially and with the coronal plane of 0°, 0° and 47° anteriorly. The resulting force components as a product of the aforementioned are presented in Table 3.3. The references of the x, y and z components are relative to the coordinate system located at the center of the femur, presented in Figure 3.6. [33]

Table 3.3 – Force components acting on the femur model

Force	Total (N)	x-component (N)	y-component (N)	z-component (N)
Hip joint	1751	393.9	92	1748.6
Abductors	765	261.6	0	718.9
Quadriceps	427	0	0	427
Iliopsoas	147	107.5	0	145.2

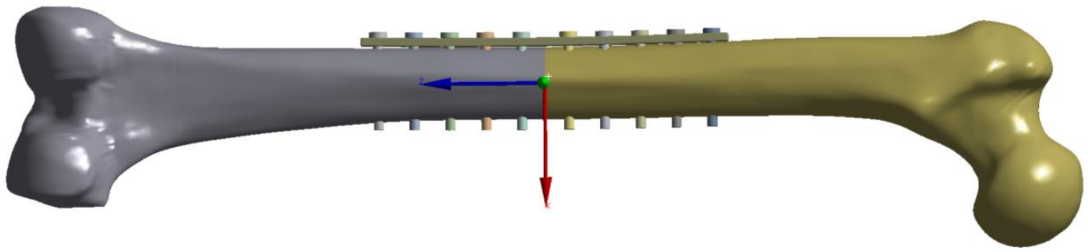

Figure 3.6 – Femur and DCP model with reference coordinate system in the ANSYS Workbench interface

3.4. Finite element analysis

These force components are inserted into the Static Structural module of ANSYS Workbench. A fixed support is placed on the patellar groove, where the femur is contacting the tibia to model the support of the knee in the standing phase of walking. Finally, the compression force derived from the plate pretension is applied on the surface between the two bone fragments as a remote force. Very limited data is available as to the magnitude of this force, since it is a result of the surgeon's experience and intuition and isn't yet standardized. According to a study conducted by Perren et al. [38], the force magnitude is in the region of 1000N. Extensive testing through simulation runs with different values of compression force, resulted in a compression force of **810N** as a minimum requirement for stability in the fracture area. Smaller forces prove insufficient in maintaining the rigidity needed to support the walking load without plate failure or loss of compression, any of which is detrimental to the healing process. As a result of the aforementioned, the final version of the force model is presented in Figure 3.7 and the following results correspond to this version.

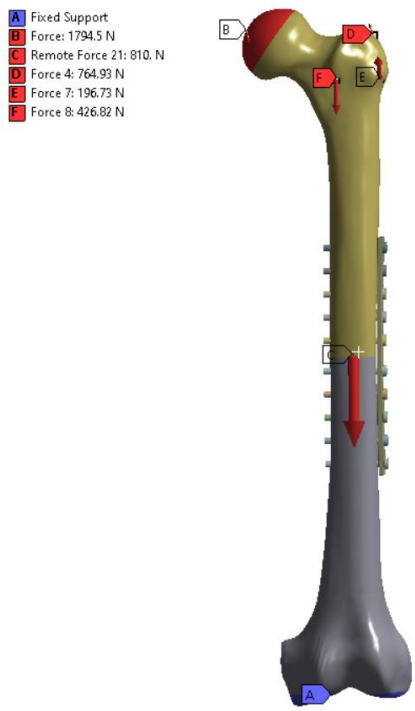

Figure 3.7 – Loading conditions for the femur and DCP model in the ANSYS Static Structural interface

To establish relations between the different parts of the models, the contact areas and types are declared, as described in Table 3.4. The values for the friction coefficients are estimates based on the studies of Voutat et al. [39] and Zhang et al. [40].

Table 3.4 – Contact areas and types for the femur and DCP model

Contact bodies	Target bodies	Contact type	Friction coefficient
Plate underside	Bone surface	Frictional	0.5
Screw threads	Bone holes	Bonded	-
Screw heads	Plate holes	Bonded	-
Top bone fragment	Bottom bone fragment	Frictional	0.9

The mesh (Figure 3.8) is generated using the Patch Conforming method with tetrahedral elements of varying size (3.0mm for the femur and 0.8mm for the plate and screws) and soft behavior.

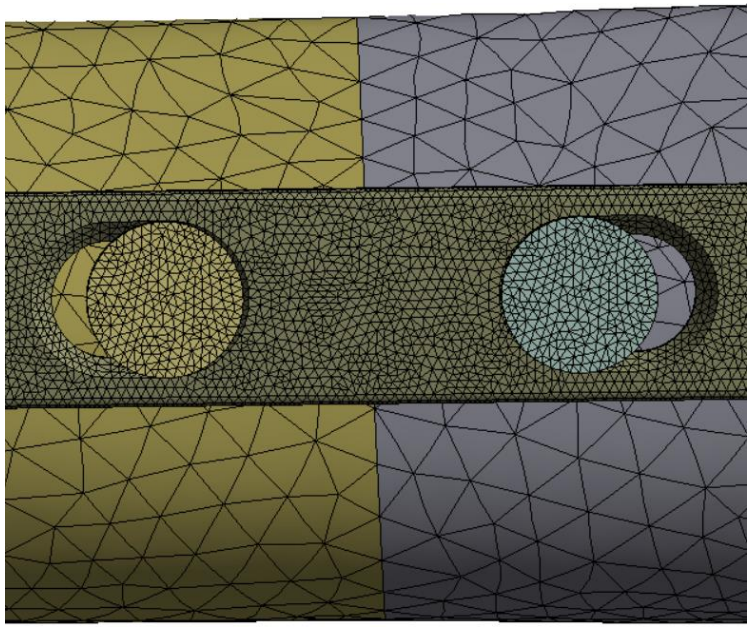

Figure 3.8 – Detail of the mesh for the femur and DCP model in the ANSYS Static Structural interface

The environment temperature for the analysis is set to 37°C, as the plate is located inside the body and the analysis settings are presented in Table 3.5.

Table 3.5 – Analysis settings for the femur and DCP model in the ANSYS Static Structural interface

Details of "Analysis Settings"

Step Controls	
Number Of Steps	1.
Current Step Number	1.
Step End Time	0.25 s
Auto Time Stepping	On
Define By	Substeps
Initial Substeps	10.
Minimum Substeps	10.
Maximum Substeps	100.
Solver Controls	
Solver Type	Program Controlled
Weak Springs	Off
Solver Pivot Checking	Program Controlled
Large Deflection	On
Inertia Relief	Off
Rotordynamics Controls	
Coriolis Effect	Off
Restart Controls	
Generate Restart Poi...	Program Controlled
Retain Files After Fu...	No
Combine Restart Files	Program Controlled
Nonlinear Controls	
Newton-Raphson O...	Unsymmetric
Force Convergence	Program Controlled
Moment Convergence	Program Controlled
Displacement Conve...	Program Controlled
Rotation Convergen...	Program Controlled
Line Search	Program Controlled
Stabilization	Program Controlled

The result of the analysis is a contour of the equivalent von Mises stress on the plate body, as presented in Figure 3.8. The maximum stress is located inside the middle screw slots and reaches a value of **627 MPa**. The posterior outer side of the plate is subjected to maximum stresses in the order of **448-492 MPa** in the location of the slots and **314-358 MPa** elsewhere. Even though the stresses are noticeably lesser than the yield strength of the titanium alloy (930 MPa), the result is an indication that the slot configurations are particularly crucial and demand attention in the design process of the new plate. It has to be noted as well, that due to torsion of the femur under load, the stress is asymmetric and higher in the posterior outer side of the plate.

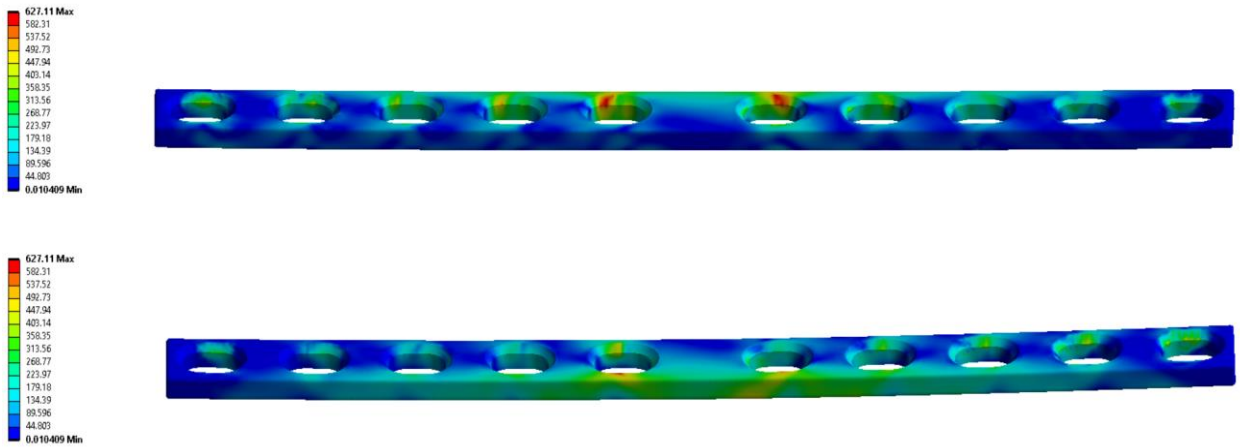

Figure 3.9 - Maximum equivalent von Mises stress contour on the DCP in the ANSYS Static Structural interface

The results obtained are comparable with various finite element analysis studies of osteosynthesis plates. Zhang et al. [41] (Figure 3.10) and Antoniac et al. [42] (Figure 3.11) performed analyses on a plates for humerus fractures. The former examined the effect of different screw hole configurations and the latter performed a failure analysis. While the stress values cannot be compared to the femur model, since the loading conditions are different, the points of maximum stress are located in the area of the screw slots in all configurations of both studies, similarly to the femur and DCP model.

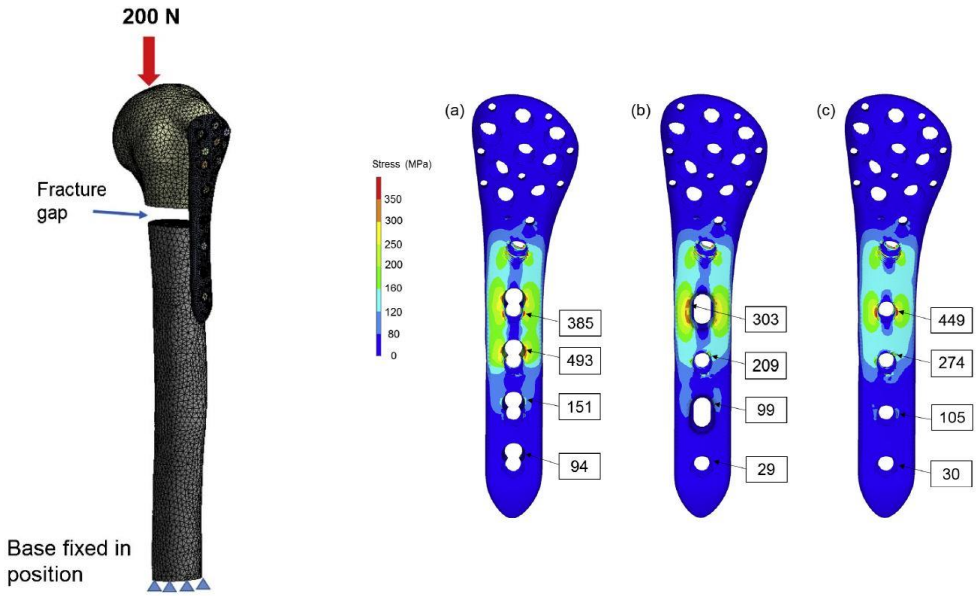

Figure 3.10 – Loading conditions and stress contours for the Zhang et al. humerus and plate model [41]

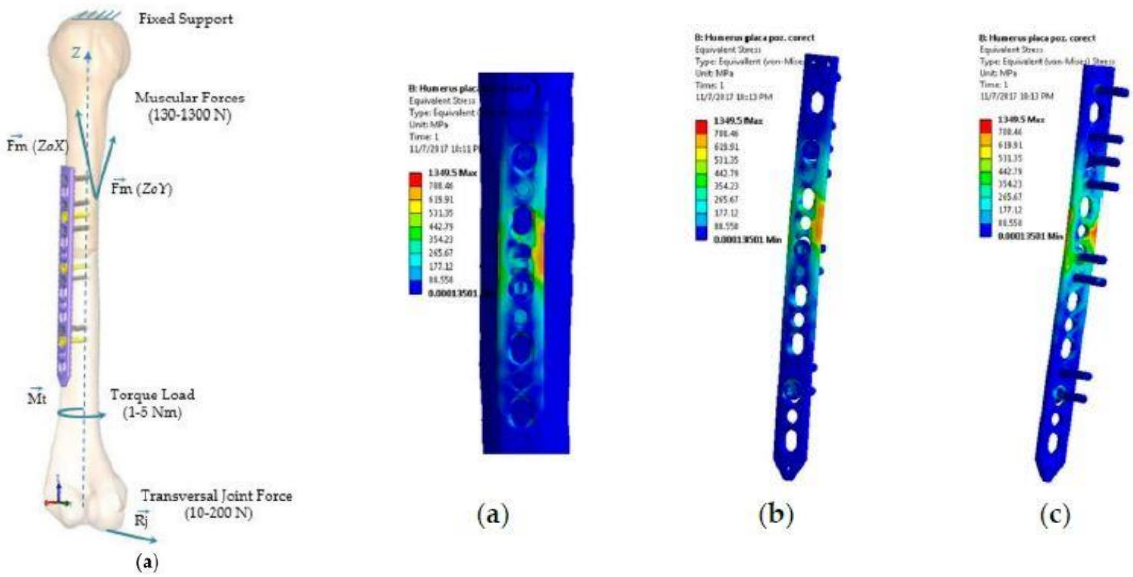

Figure 3.11 – Loading conditions and stress contours for the Antoniac et al. humerus and plate model **[42]**

Zhou et al. [43] created a model for a three-part LCP and a regular LCP, applied on a femur comminuted fracture. The maximum stress value calculated for the three-part plate is very high, at 1565 MPa, whereas the corresponding value for the LCP is 681.3 MPa (Figure 3.12). Due to the major differences in design and mechanics of the three-part plate compared to regular plates, no useful conclusions can be extracted. However, the analysis of the regular LCP provides an indication for the accuracy of the DCP model, as the difference of approximately 230 MPa in the maximum stress value can be logically attributed to the differences of the load models, type of fracture (comminuted versus transverse non-displaced and type of plate (LCP versus DCP).

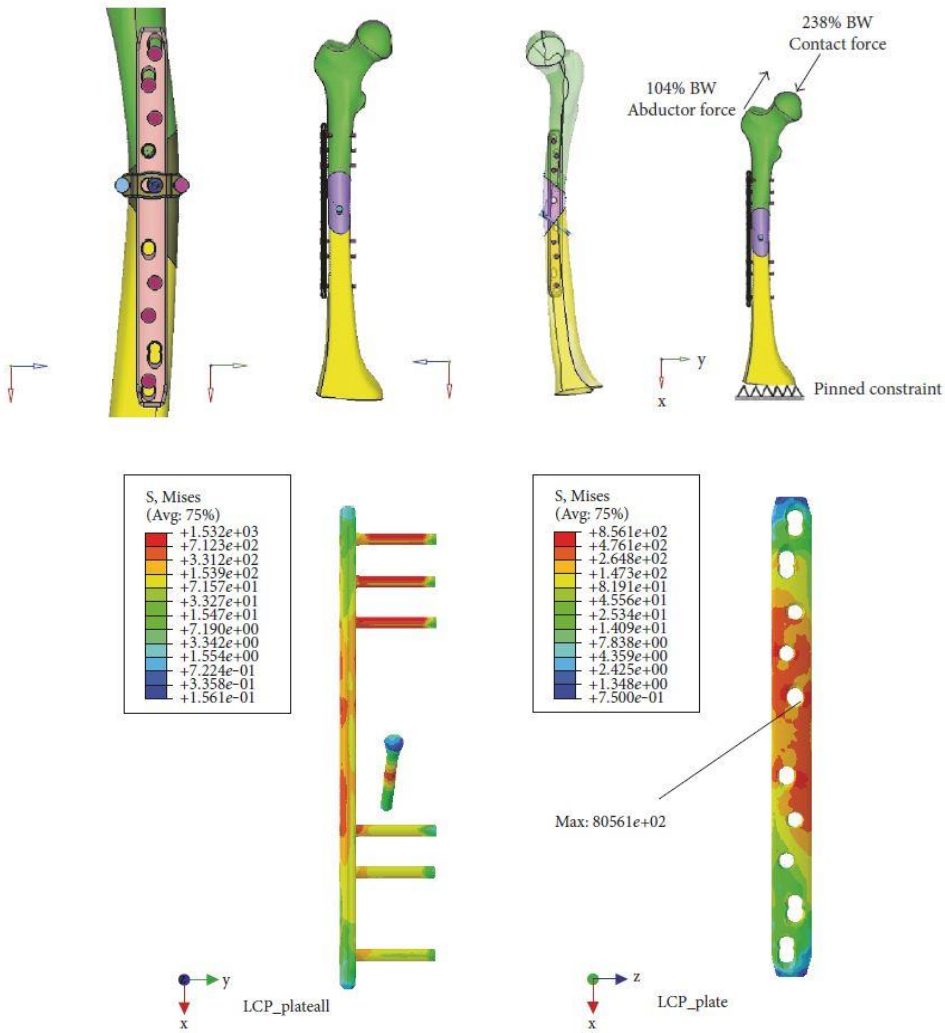

Figure 3.12 – Loading conditions and stress contours for the Zhou et al. femur and plate model **[43]**

The main takeaways of the analysis are initially deemed plausible, as they are in line with several known benchmarks and empirical descriptions of orthopedic surgeons. Generally, osteosynthesis plates tend to fail at the screw slots sites, which are widely considered to be weak points in the structures. As far as the compression force is concerned, the data available is scarce and despite the minimum force calculated from the model at 810N is within an expected range, further research and comparisons with experimental data would be beneficial in determining the definitive accuracy of the calculation.

4. Conceptual design

The conceptual stage of the design process involves the inception and description of various solution concepts that address the main specification points. The primary goal of the conceptual design isn't the production of detailed and mature designs, but rather the creation through brainstorming of multiple crude solutions that can be compared and evaluated in a systematic way. The process begins with the listing of technical specifications for the device that are used to create evaluation criteria, a list of alternative solutions and an evaluation process to determine the best alternative that will be the focus of the embodiment design stage.

4.1. Technical specifications and selection criteria

A variety of criteria is examined, in order for the different solutions to be evaluated and for the best ones to be selected to proceed to the detailed design phase. The selection criteria are directly based on the technical specifications for the device and are classified in five main categories as follows:

1. Bone healing facilitation

    a. *Preservation of blood supply*

    The degree to which the device allows for adequate blood supply to the fracture area to promote cell regeneration. The blood supply is dependent on the area of contact between the periosteum and the surrounding soft tissues and on the pressure of the plate against the bone, which, if excessive, can cut off blood supply with adverse effects for healing of the fracture.

    b. *Ensuring proper alignment and contact between bone fragments*

    The degree to which the device correctly aligns the bone fragments and ensures optimal contact between them, in the installation phase. The relative position of the fragments is very important for protection against refracture and for faster recovery.

    c. *Promotion of callous formation through micromovements*

    The degree to which the fixation allows for small relative motion (micromovements) between bone fragments, which promotes secondary callous formation. It has to be noted, however, that the device is to be primarily oriented towards primary callous formation.

2. Adjustment potential

    a. *Range of possible positions*

    The maximum distance between fragments that is possible to be compensated by the adjustment mechanism of the device. The minimum requirement is set at 5mm.

b. *Control on compression progression*

The level of control on the compression during the adjustment phase. The ability of achieving any desired progression in a pre-determined and precise way, as opposed to a random one, is judged.

c. *Ability of correcting mistakes after initial adjustment*

d. *Ability of not adjusting if not needed*

3. Application difficulty

a. *Control equipment complexity*

The technological and design complexity of all equipment necessary to control the adjustment parameters of the device during the rehabilitation phase.

b. *Manufacturing methods and time*

The complexity of the manufacturing methods used for the production of the device and its control equipment, as well as the total duration of the manufacturing process.

c. *Storage conditions*

The need for special storage conditions (specific temperature, humidity, other devices and materials) for the preservation of the properties of the device that are sensitive to the conditions of their environment.

d. *Dimensions*

The ability to achieve the required rigidity and adjusted compression without exceeding the restrictive dimensions of the bone area surrounded by soft tissues. The final dimensions must be comparable to current DCPs. Typical dimensions for a wide 10-hole DCP are in the range of 175x15x4.5 mm.

e. *Level of invasion*

How invasive the installation during surgery and the post-operation adjustment procedures are, in terms of incisions, operation time and foreign bodies inserted in the body for the device to function properly. The surgery is desired to be equally or less invasive compared to current practice and the adjustment must be minimally invasive or non-invasive.

f. *Simplification and improvement on current method*

The degree to which the proposed device and method simplifies and improves the current solution, in terms of processes, technologies used and scientific value.

g. Need for removal

Whether the device must be removed after rehabilitation, in order to avoid possible complications and discomfort for the patient. The removal protocol should remain the same as in current plates.

h. Surgeon training and skill level

The degree to which extensive training and exceptional skills are needed for the surgeon to familiarize themselves with the new device and to be able to install it correctly.

i. Post-operation care

The complexity of patient care and procedures needed for successful operation and maintenance of the device during the rehabilitation phase.

4. Robustness and reliability

a. Strength

The fixation's stiffness and durability compared to the current plates, for the same dimensions.

b. Minimization of risk for post-op complications/recurring fractures

How effectively the fixation minimizes the risk for complications in the rehabilitation phase and how quickly the patient can return to normal activity without problems.

c. Versatility for different types of fractures

Whether the fixation can be used for every type of long bone (femur, tibia, fibula, ulna, radius, humerus) with minor adjustments.

d. Adjustment mechanism reliability

Whether the adjustment mechanism is capable of operating without fault for the entirety of the adjustment procedure.

e. Biocompatibility

f. Interaction with the environment or other devices

How sensitive the device is to environmental conditions or proximity to other devices and the degree to which unexpected environmental effects render it non-functional.

g. Consequences in case of failure

The level of protection and safety the device offers to the patient in case of unexpected failure.

5. Cost
    a. *Materials*
    b. *Manufacturing*
    c. *Post-operation*
    d. *Surgeon training*

The cost of the device is not initially considered as a defining factor in the selection process, therefore there is no cost requirement. Nevertheless in later design stages a cost analysis will be performed.

4.2. Alternative solution list

A list of alternative solutions is formulated, as a product of research for existing devices and a brainstorming procedure. The solution concepts presented, qualify for further examination, as they satisfy the basic requirements stated in the technical specifications. Other solutions that were deeemed inadequate or inapplicable in this early selection stage are not included in the following description.

1. Rack-pinion

    A simple rack-pinion mechanism of a two-part plate is proposed. The outer part is a simple DCP or LCP with a central slot and an adjusting pinion gear, whereas the inner part is a thinner plate with a rack attachment, sliding in the slot of the outer part. The pinion determines the position of the rack, thus controlling the compression on the fracture site. It can be directly rotated with a screwdriver, or remotely with a magnetic induction mechanism. With the use of this mechanism, only one of the two bone fragments is mobile and is compressed against the other fragment.

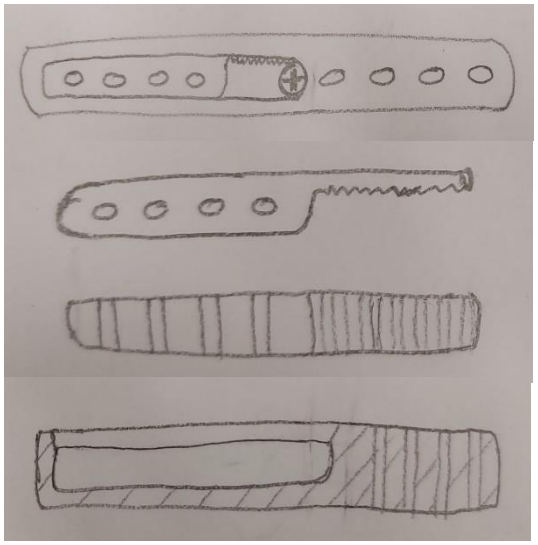

Figure 4.1 – Rack-pinion sketch

2. Weight-based adjustment

This solution is utilizing the progressive increase of load bearing on the bones during the rehabilitation phase. The same two-part plate with a slot and sliding part is used. Two variations are proposed, in regard to the adjusting mechanism that controls the position of the inner plate.

a. Ratchet

A ratchet mechanism is attached to the inner plate and locks into place inside the corresponding detents of the outer plate. The load on the bone during the gait, exerts a force on the mechanism and adjusts the plate position, achieving increased compression progressively.

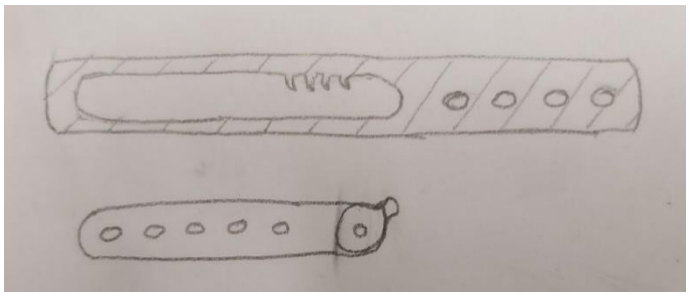

Figure 4.2 – Weight-based ratchet sketch

b. Permanent deformation spring

A compression spring is coupling the inner and outer plate resisting the sliding of the inner plate inside the slot. The spring deforms permanently when compressed under the gait load and holds the inner plate into the desired position.

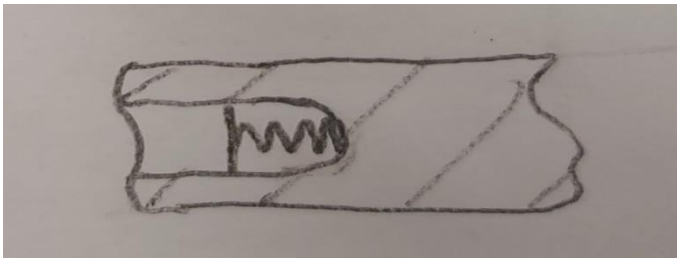

Figure 4.3 – Weight-based permanent deformation spring sketch

3. Magnetic screw tightening

A normal DCP or LCP is attached to the bone with specialized screws. The screw heads are magnetic and could have an adjusted shape to facilitate the production of the electromagnetic force. The mechanism is based on the operation principle of magnetic induction and is implemented with an external rotating magnet of inverse polarity to the screw head. Depending on the direction of the rotation, the screws are tightened or untightened. A controlled

tightening of one or more screws results to an increase of the compression force. Depending on the screws activated, only one or both bone fragments can be mobile.

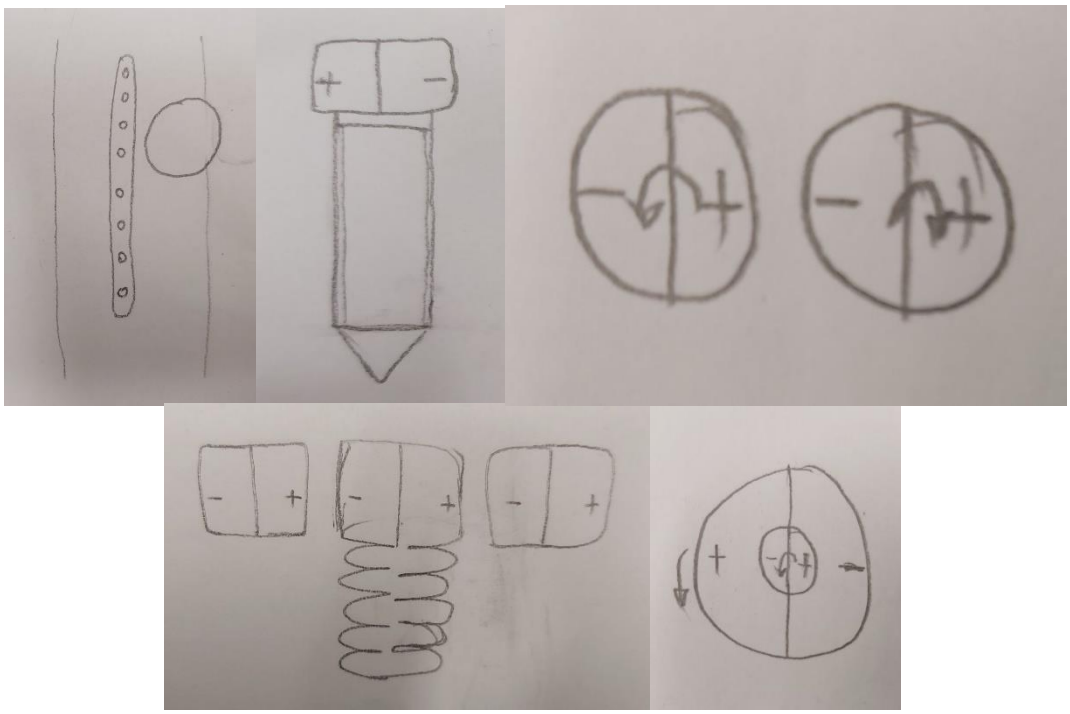

Figure 4.4 – Magnetic screw tightening sketch

4. Shape memory plate

In this solution, the properties of shape memory materials are used to construct a self-adjusting plate that recovers its shape, eliminating the use of external equipment. For this application, the use of the environment of the body in the fracture site (pH, humidity, temperature) or of an injectable solution is viable. Based on the location of the shape memory material the following variations are proposed.

a. Contracting plate

The whole body of the plate is constructed from shape memory material, or from a composite with shape memory fibers. Over time, the plate contracts and produces added compression to bring the bone fragments into contact.

b. Expanding slots

The shape memory material is used only in the areas around the screw slots. Instead of the plate contracting, the slots expand, allowing for the intended compression.

5. Shape memory screws

A normal DCP or LCP is screwed onto the bone using modified screws with shape memory parts, which degrade and allow further compression and micromovements. Similarly to the previous case, two variations are distinguished according to the location of the shape memory material.

a. Shape memory shaft

The screw shaft includes a shape memory collar which increases the available space for compression and micromovements, making the fixation less rigid.

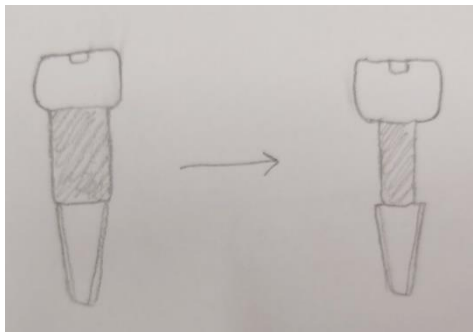

Figure 4.5 – Shape memory screw shaft sketch

b. Shape memory head

The screw head has a shape memory outer part, or rests on a shape memory base. Depending on the shape-changing mechanism, the screw angle and/or their position is modified.

6. Screw-less fixation

This fixation type eliminates the need for screws, which can be problematic due to installation problems and stress concentration. The fixation is mounted on both bone fragments, away from the fracture site, using collars and utilizing the friction force for stability and compression force production. It can be located either internally, inside the medullary canal, or externally like most fixation devices.

a. Shape memory scaffold

A scaffold structure from shape memory material is proposed, to ensure the greatest contact area between the bone and the surrounding soft tissues possible. The structure offers stability in an extended area and contracts gradually due to the body environment, or on demand after the injection of a fluid with specific properties which trigger the shape memory mechanism.

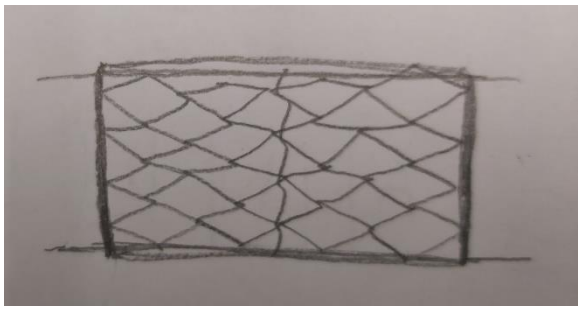

Figure 4.6 – Screw-less shape memory scaffold sketch

b. Bone sleeve

An external sleeve is stabilized with adjustable collars, which increase the axial compression through friction when they are tightened. The tightening can be controlled with an adjusting screw or shape memory material rings in the collars.

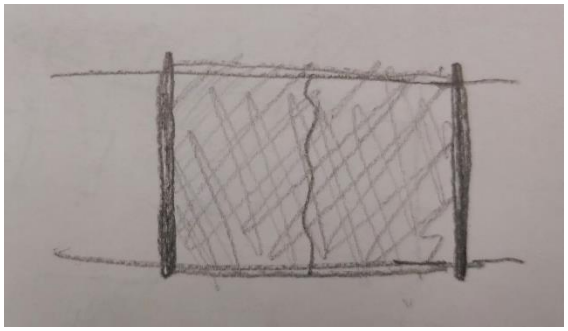

Figure 4.7 – Screw-less bone sleeve sketch

7. Shape memory screw connector

The compression control is achieved by connecting the plate screws together. The screw heads or shafts are designed with a slot for placement of the shape memory connector. The connector contracts under the effect of a stimulus which activates the shape memory mechanism, thus reducing the distance between the screws and increasing compression of the bone fragments.

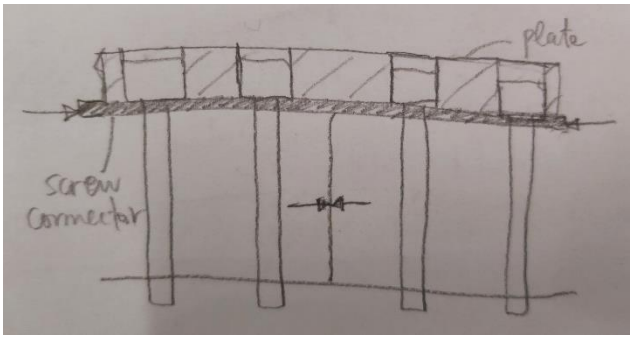

Figure 4.8 – Shape memory screw connector sketch

8. Split plate

   A two-part plate, with a spring or shape memory connector between the two parts is used. The parts must remain connected to preserve contact between the bone fragments.

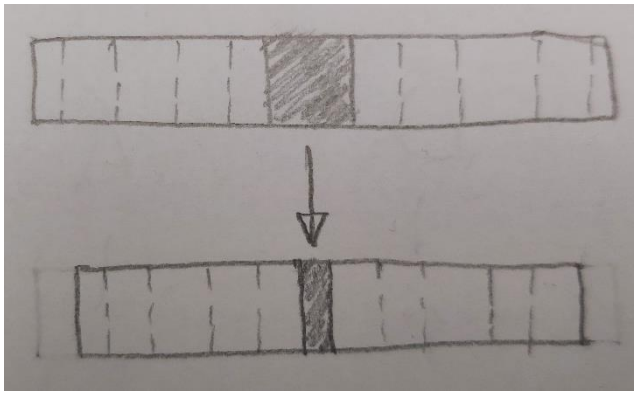

Figure 4.9 – Split plate sketch

4.3. Evaluation method

The alternative solutions are evaluated according to the aforementioned criteria as to their suitability, in order for the best solution to emerge. Each different variation is given a score in the 0 to 5 scale for its fulfilment of each individual criterion. A score of 0 denotes non-existent satisfaction of the criterion, whereas a score of 5 denotes excellent satisfaction of the criterion. The scores for each criterion are multiplied with a weight coefficient, used to prioritize the criteria by their importance for the function of the device and are then summed to extract the final score for the different solution propositions. The most essential criteria for the function of the device are deemed to be the blood supply, alignment and contact, axial force control, mistake correction, non-adjustment, invasion level, strength, interaction with the environment, failure consequences, material cost and manufacturing cost. The weight coefficients for all these criteria are above the average value, in order to highlight their influence in the selection. The sum of all weight coefficients is 1, therefore the maximum achievable score is 5 and the minimum is 0. After this procedure, the solutions are sorted by their evaluation score and the best ones are determined. The solutions are evaluated and assigned scores by two independent evaluators and the final score is extracted as the mean of two evaluations (Table 4.1). The final scores for the alternative solutions and a detailed breakdown of the assignment of weight coefficients and individual scores for each criterion are presented in Appendix II.

Table 4.1 – Final evaluation scores of alternative solutions in descending order of highest score

Alternative	Solution	Mean score	Score 1	Score 2
3 Variable magnetic screw		**4.10**	4.15	4.05
6 Screw-less	a Shape memory scaffold	**3.53**	3.75	3.32
7 Shape memory screw connector		**3.48**	3.69	3.28
6 Screw-less	b Sleeve	**3.45**	3.63	3.26
5 Shape memory screws	a Shaft	**3.40**	3.52	3.28
4 Shape memory plate	a Contracting plate	**3.38**	3.51	3.25
5 Shape memory screws	b Head/Angle cone	**3.36**	3.52	3.20
4 Shape memory plate	b Variable slots	**3.33**	3.51	3.15
8 Split plate		**3.14**	3.29	2.99
1 Rack-pinion		**2.89**	2.99	2.80
2 Weight-based	b Spring	**2.67**	2.80	2.54
2 Weight-based	a Ratchet	**2.41**	2.63	2.19

The variable magnetic screw solution performed well in almost all criteria, excelling specifically in the adjustment potential category. The magnetic field application has the potential to offer accuracy, paired with minimal invasion and reliability. The adjusting mechanism concerns the screws and the plate body can remain unchanged, in line with the current standards. This allows for the focus to be shifted towards the function of the mechanism, rather than strength and reliability, which are expected to be adequate.

The shape memory scaffold and shape memory screw connector also exhibit potential, particularly in the healing facilitation and invasion, at the expense of some adjustment accuracy and strength. The use of shape memory materials allows for non-invasive adjustment and is increasingly prominent in medical applications. It should be noted, however, that the manufacturing and machining of these materials can be challenging, therefore the cost of their applications is increased.

4.4. Feasibility study and final concept selection

The solution of variable magnetic screws amasses the highest mean score with a considerable difference to the next best scoring alternatives (shape memory scaffold, shape memory screw connector). Consequently, it is prioritized and examined in more detail to determine its feasibility. The other aforementioned solutions are also examined as secondary priorities, to allow for further flexibility in case the main solution is ultimately unsuitable.

4.4.1. Variable magnetic screws

In order to test the feasibility of the magnetic screws, basic calculations of the required torque for screwing a single screw in the bone are performed.

A singular square thread that is screwed onto a nut can be modeled as a rectangle sliding on a sloped plane at an angle a to the x axis and the forces on the nut are displayed in Figure 4.10.

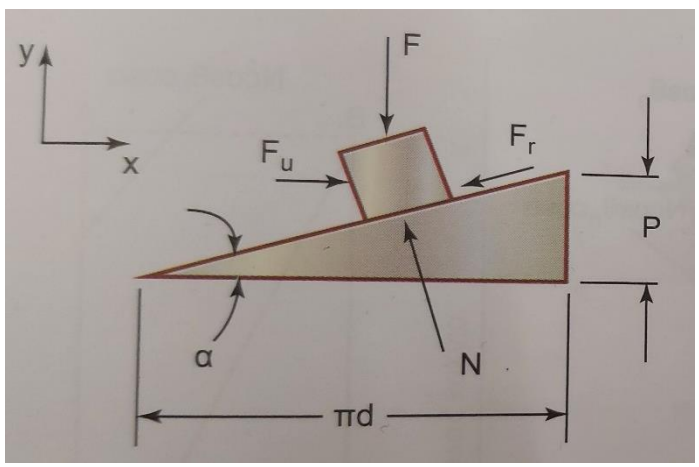

Figure 4.10 – Forces on a square thread and nut pair [44]

The forces on each axis are as follows:

$$\sum F_x = F_u - N \sin a - F_r \cos a = 0 \;\rightarrow\; F_u = N\,(\mu \cos a + \sin a) \;(4.1)$$

$$\sum F_y = -F + N \cos a - F_r \sin a = 0 \;\rightarrow\; F = N(\cos a - \mu \sin a) \;\;(4.2)$$

By dividing the two equations and expressing the coefficient of friction μ as an additional angle ρ of the sloped plane (where tanρ=μ), the formula for the screwing force Fu is obtained.

$$\frac{(4.1)}{(4.2)} \rightarrow F_u = F\,\frac{\mu \cos a + \sin a}{\cos a - \mu \sin a} = F\,\frac{\tan \rho + \tan a}{1 - \tan \rho \tan a} \rightarrow F_u = F \tan(\rho + a) \;\;(4.3)$$

As a result the required screwing torque M_s is calculated as:

$$M_s = F\tan(\rho + a)\frac{d_2}{2} \quad (4.4)$$

In a thread like the one on cortical bone screws, the normal force on the nut is applied at an angle $\theta_n = \beta/2 = 15^o$ to the xy plane, therefore the projection of this force on the xy plane is sketched. The modified force equations are the following:

$$\sum F_x = F_u - N\sin a\cos\theta_n - F_f\cos a = 0 \;\rightarrow\; F_u = N\,(\sin a\cos\theta_n + \mu\cos a)\;(4.5)$$

$$\sum F_y = -F + N\cos a\cos\theta_n - F_r\sin a = 0 \;\rightarrow\; F = N(\cos a\cos\theta_n - \mu\sin a)\;(4.6)$$

Similarly, the equations are divided and the modified additional angle of the plane ρ' is defined, where $\tan\rho' = \frac{\tan\rho}{\cos\theta_n}$. The equation for the screwing force derives as follows:

$$\frac{(4.5)}{(4.6)} \rightarrow F_u = F\,\frac{\sin a\cos\theta_n + \mu\cos a}{\cos a\cos\theta_n - \mu\sin a} = F\,\frac{\tan a\cos\theta_n + \tan\rho}{\cos\theta_n - \tan\rho\tan a} = F\,\frac{\tan\rho' + \tan a}{1 - \tan\rho'\tan a}$$

$$\rightarrow \quad F_u = F\tan(\rho' + a) \quad (4.7)$$

And the corresponding screwing torque is:

$$M_s = F\tan(\rho' + a)\frac{d_2}{2} \quad (4.8)$$ [44]

Using the equations (4.7) and (4.8) and assuming an axial load of F=1000N on the screw, the values for screwing forces and torques are obtained for several cases (Table 4.3). The cases examined differ in the diameters of the screws and the coefficient of friction. Other relative parameters of the screws are presented in Table 4.2.

Table 4.2 – Parameters for 3.5mm and 4.5mm cortical screws (ISO 5835:1991)

Screw diameter d (mm)	Pitch (mm)	Inner diameter (mm)	Angle a (rad)
3.5	1.25	2.4	6.486
4.5	1.75	3.0	7.057

Table 4.3 - Screwing force and torque values for 3.5mm and 4.5mm cortical screws

Screw diameter d (mm)	Coefficient of friction μ=tanρ	Screwing force F_u (N)	Screwing torque M (Nm)
3.5	0.4	553.83	0.665
	0.5	670.75	0.805
	0.6	790.63	0.949
4.5	0.4	566.93	0.850
	0.5	685.29	1.025
	0.6	806.95	1.210

The required torque range is calculated at **0.67-1.21 Nm**. Even the maximum value is attainable with the use of external magnets, making the solution initially feasible. Nonetheless, there are also shortcomings that arise and they must be considered before progressing. Most importantly, the production of this torque requires a relatively strong magnetic field and therefore a large external magnet and motor to rotate the magnet. Due to the restrictive dimensions for the screws, specially designed screws with larger heads that facilitate magnetic force application are challenging to use. Furthermore, the presence of skin and other soft tissues between the screws and external magnet is a considerable injury risk with strong magnets and rotating components that can trap those tissues between them. As a result, the adjustment procedure is projected to only be carried out in a controlled environment with the presence of a medical professional. Finally, there is a fundamental question pertaining to the interaction of the magnetic components with the environment of the patients. There is a possibility that the magnetic screws will attract metal objects in their vicinity, which is an immediate injury hazard, while an MRI scan is impossible to perform. Overall, the proposed solution is promising, however there is uncertainty about several details of the device and its function. For this reason, it is not selected to progress to the embodiment design phase.

4.4.2. Shape memory and superelasticity

Analyzing the shape memory scaffold and screw connector solutions requires a brief study of the properties and uses of shape memory materials in medicine. The main characteristic of these materials is the ability to “remember” and recover a predetermined shape even after significant deformation. The shape recovery effect can be activated by a variety of triggering events, including temperature change, mechanical load, environment pH change, electric current, magnetic fields and others. The most prominent categories of shape memory materials used in medical

applications today are shape memory polymers (SMPs) and shape memory alloys (SMAs). [45], [46]

The SMPs have two phases, the fixity or glassy phase responsible for stability of the permanent shape and the reversible or rubbery phase responsible for shape recovery (Figure 4.11). In the most common case of temperature-based shape recovery, the characteristic temperature of the shape memory effect is the glass transition temperature (T_g). An SMP in the fixity phase can be heated above the glass transition temperature and into the reversible phase, deformed into a new shape under mechanical load and cooled below the T_g to solidify the new shape. If the polymer is heated again, it recovers the original shape returning to the fixity phase. The reduced cost, easy processing and biocompatibility of SMPs have rendered them vastly utilized in many applications in the medical field, most notably stents, sutures, staples and micro tools. For orthopedic applications, polymers are rarely used due to their limited stiffness and load bearing capabilities, therefore they are not considered suitable to use in the particular solutions. [47], [48]

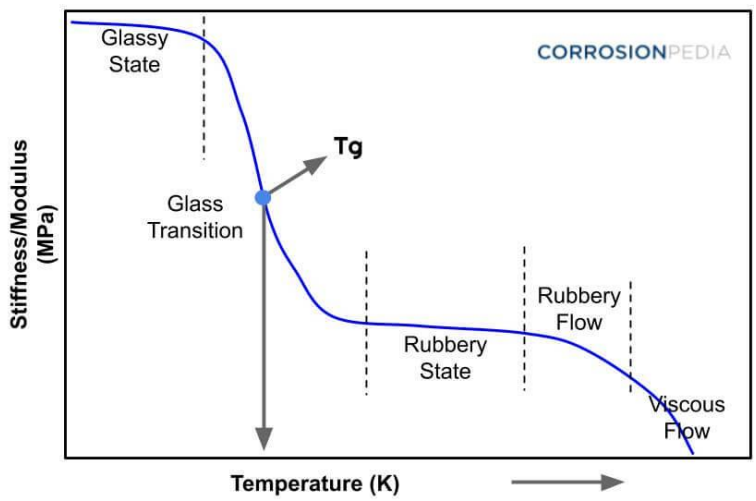

Figure 4.11 – Stiffness-temperature graph for shape memory polymers **[49]**

The SMAs on the other hand owe their shape memory capabilities to a martensitic transformation. They also alternate between two phases, a stable austenitic phase for the permanent shape and a deformable martensitic phase, where the change of shape occurs. In temperature-induced martensitic transformations, the characteristic temperatures are the martensitic start (M_s), martensitic finish (M_f), austenitic start (A_s) and austenitic finish (A_f) temperatures. An SMA at the austenitic phase, above the A_f, can be cooled below the M_f in a twinned martensite that can be deformed into detwinned martensite under relatively low loads, assuming a transformed shape. When the load is removed, the new shape is retained. Heating above the A_f then recovers the original shape [50], [51]. In contrast to SMPs, the SMAs additionally exhibit superelastic properties in the austenitic phase, due to a thermoelastic stress-induced martensitic transformation

this time. A large enough load can transform the austenite into detwinned martensite, however in this case the removal of the load leads to immediate recovery of the original shape.

Figure 4.12 – Stress-strain curves for shape memory alloys exhibiting shape memory effect and superelasticity [52]

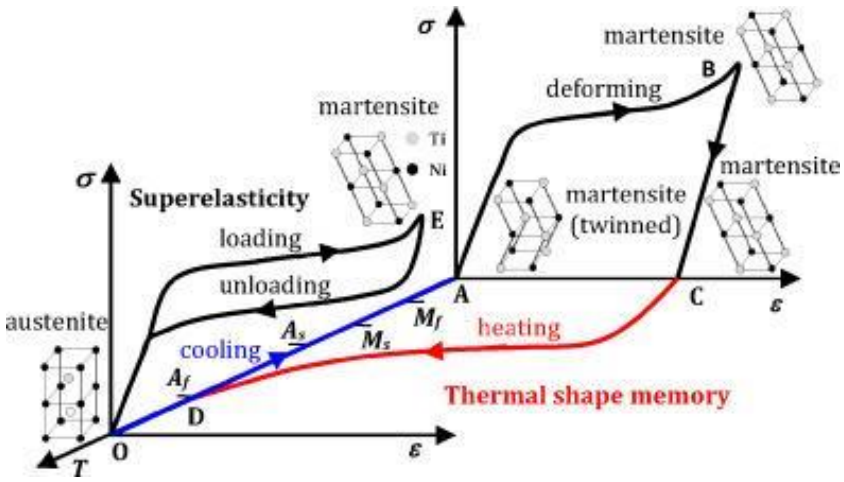

The most commonly used SMAs in medicine are Au-Cd, Cu-Zn and predominately Ni-Ti alloys, since the transformation temperatures of the latter are usually around body temperature [47]. Ni-Ti alloys, also called Nitinol for near equal amount of nickel and titanium (atomic 50-51%, weight 55-56% Ni) exhibit shape memory and superalastic characteristics in this particular range of nickel concentration, due to the presence of a parent austenite phase formed in an ordered body-centered cubic crystal structure at temperatures around 973K, where the permanent shape is set [51]. The phase diagram of Ni-Ti is available in Figure 4.12.

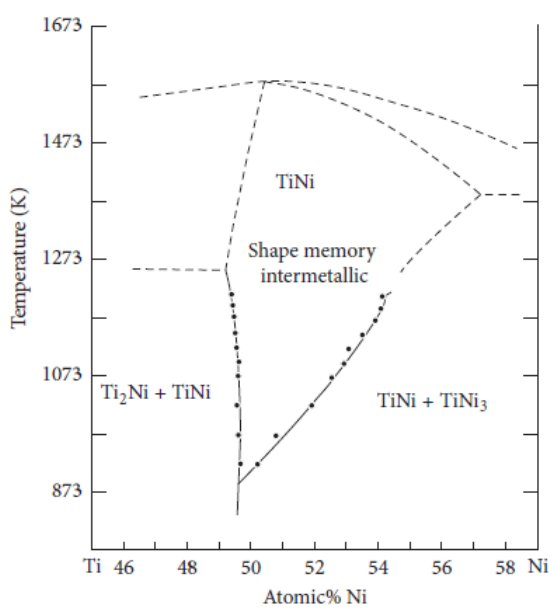

Figure 4.13 – Partial phase diagram of Ni-Ti [53]

These alloys are used in a variety of medical applications, such as expandable stents, endoscopic instruments, orthodontic wires and most importantly orthopedic staples and even plates [47], [51]. Even though these staples and plates are presently designed for small bones, such as phalanges, metatarsals and jaw bones, their unique properties could offer solutions even in long bone osteosynthesis, of course taking the strength limitations compared to stainless steel and titanium plates into account. These limitations make a solution like the scaffold challenging to apply, since the lightweight formations required to reduce disruption of the periosteum and blood supply only offer low rigidity and are bound to face strength problems. Therefore, the screw connector solution projects as superior, since the shape memory parts can be paired with stainless steel or titanium to form the rigid body of the plate.

The twofold nature of Nitinol permits the choice of the desired shape recovery effect (shape memory or superelasticity), depending on the temperature area it is going to be used at. Comparing the two, it becomes clear that the shape memory effect presents specific disadvantages for the particular application. The adjustment has to be performed in a controlled fashion and approximately 1-2 months after the operation. Therefore, an alloy with A_f around body temperature isn't suitable, because the transformation would be triggered during the operation. Taking into account the local temperature rise due to inflammation, the A_f should be in the range of 50°C which demands heating of the area during the adjustment procedure. As the heating should be localized inside the body and not on the surface of the skin and in a range tolerable to the tissues, a heating coil could be utilized. However, the coil must have a large enough diameter to surround the leg and heat the fracture area along its axis of symmetry. This procedure is complicated and can only be carried out under professional supervision, whereas the precision in the temperature achieved must be excellent to avoid unpredictable behavior of the shape memory transformation and mainly discomfort to the patient. In general, the control of the shape memory effect is very challenging and costly, in order to ensure that the transformation will occur as intended. On the contrary, if Nitinol is used in the superelastic range, namely above the A_f temperature, the elastic recovery can be taken advantage of to compress the bone fragments. The A_f can be at around 0°C, so that the plate is at the stable austenitic phase during all stages of the procedure. Moreover, the superelastic shape recovery is a simpler mechanism compared to shape memory recovery, as it is direct and it occurs immediately after the deforming load is removed, thus not requiring an external triggering event that has to be precisely controlled.

The superelasticity effect of Nitinol was studied by Qian et al. [54] who performed an experiment of loading and unloading cycles in Nitinol wires (50.9% Ni, 0.5mm diameter) in the superelastic temperature range ($T>A_f$) and compared the results with an improved theoretical model based on Graesser and Cozzarelli's model [55], which accounts for the martensitic hardening behavior of Nitinol. The characteristic temperatures of the alloy are M_f= -73°C, M_s= -55°C, A_s= -23°C and A_f= 5°C The stress-strain curves obtained are shown in Figure 4.14, where the characteristic hysteresis loops are present, with the elastic area and the upper plateau (almost constant stress for

increasing strain) in the loading phase, as well as the lower plateau (almost constant stress for decreasing strain) and recovery without residual strain in the unloading phase.

Figure 4.14 – Superelastic nitinol stress-strain hysteresis loops comparison between experimental data and an improved Graesser and Cozzarelli theoretical model

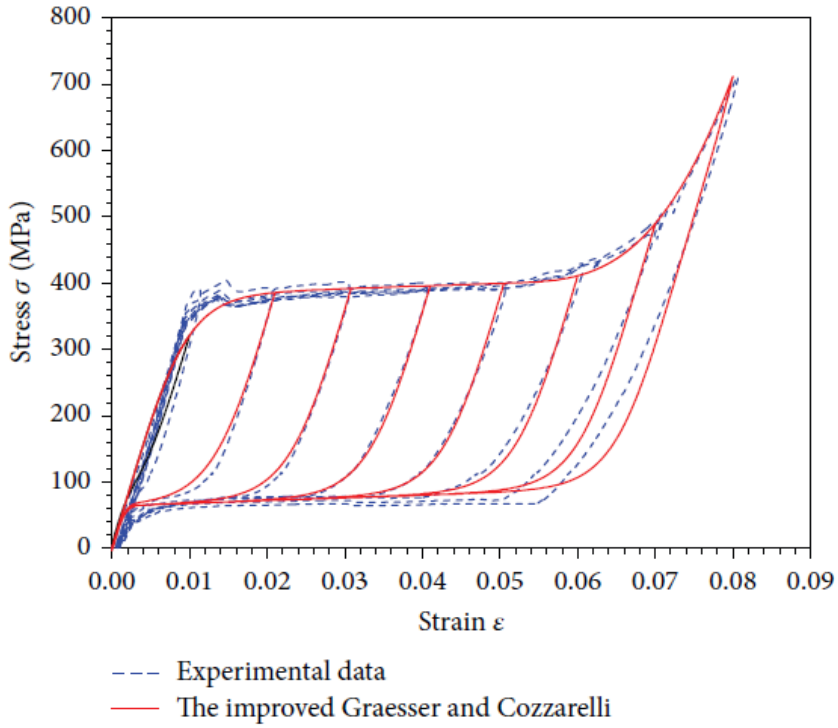

As a result of the aforementioned points, an advanced concept for the screw connector is created (Figure 4.15). The proposed design is a two-part plate, composed of a titanium external casing for increased strength and a superelastic nitinol internal plate acting as the screw connector for adjusting the compression force. The internal plate is initially deformed and inserted into the case under tension and contacts all screws, so that it can displace them and produce compression through superelastic recovery. After the installation and placement of the screws, the external load is removed and the plate is allowed to contract until the fracture gap is closed and compressed. The compression force is almost constant, as can be exacted from the available stress-strain curves of the material for the unloading phase and the adjustment is completely non-invasive and automatic. At the onset of a possible fracture gap widening, the plate shortens until the bone fragments come into contact again and maintains compression in the area due to the residual compressive stress. The concept is selected to be further developed and analyzed in detail for the final design parameters to be determined.

Figure 4.15 – Advanced concept for the screw connector, using a titanium case and a superelastic inner plate

5. Embodiment design

The embodiment design stage encompasses the design steps required to progress from the selected concept to the construction of the device, the design is finalized and the relevant parameters are calculated elaborately. The goal in this stage is the creation of a comprehensive design that meets all the relevant technical specifications and can be used to create a prototype. The design process is divided into four sections for the superelastic plate, the tensioning tool, the titanium case and the description of the surgical procedure for installation of the new device, called hereinafter the superelastic compression plate (SCP).

5.1. Superelastic compression plate

The design of the SCP is the most complicated part of the process, as it is the most critical component for the desired function of the plate, i.e. the compression adjustment. The technical specifications that need to be satisfied for the SCP are the following:

- 5-6mm of deformation at 5-6% strain, in order to mitigate a relatively large fracture gap without being close to failure
- Uniform deformation across the length of the plate
- Sliding mechanism for the screws allowing for axial displacement of the bone
- Compression force production matching the standard for DCPs (at least 800N)
- Special form elements to accommodate the tensioning tool that is necessary for the deformation of the plate

5.1.1. Screw slot configuration

Four distinct screw slot configurations are designed and compared between them as to the degree to which they satisfy the specifications. The two parameters tested are the number of total slots on the plate and the shape of the slots, therefore the plates tested cover the range of combinations for 6-slot and 8-slot configurations with oval or rectangular slots. The models of the plates are presented in Figure 5.1.

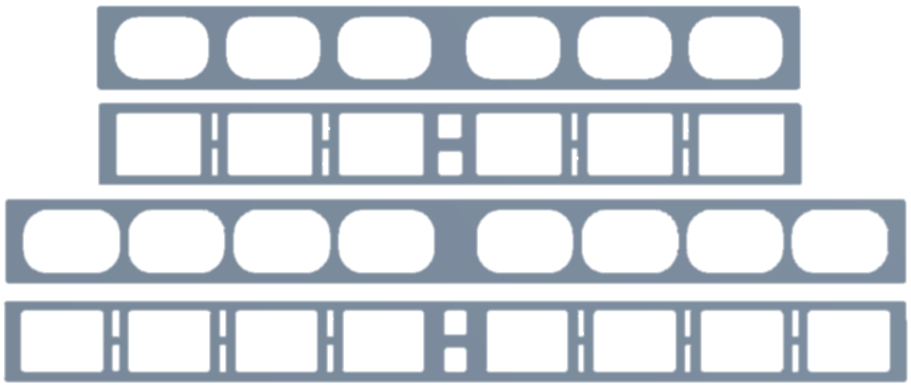

Figure 5.1 – Four screw slot configurations for the SCP

The testing is performed using the Static Structural module of ANSYS Workbench. The setup of the finite element model is demonstrated below on one of four configurations and is identical for all other configurations. A fixed support is placed on the middle of the plate and a displacement value is defined for each of the two ends (Figure 5.2). The displacement is applied in two phases, one simulating the loading phase with a linear increase of the displacement up to 3mm laterally for each end and one simulating the unloading phase by cancelling the displacement back to the original length. The loading conditions simulate the use of a tensioning tool that tensions the plate symmetrically.

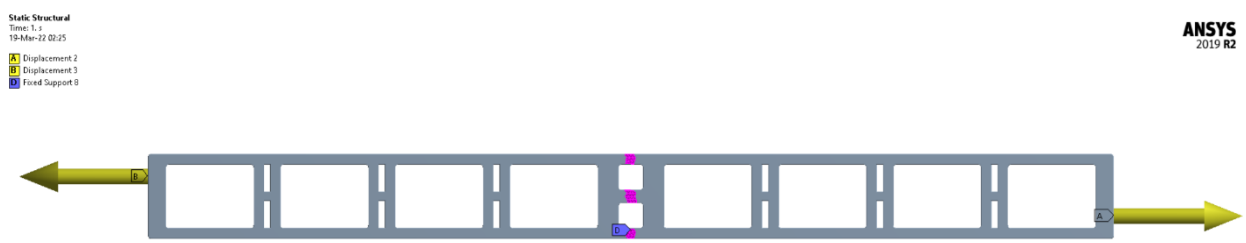

Figure 5.2 - Loading conditions for the femur and DCP model in the ANSYS Static Structural interface

The mesh is generated using the Patch Conforming method with tetrahedral 0.5 mm elements and soft behavior. The material properties for Nitinol are derived from the findings of Qian et al. [54] and are displayed in Table 5.1. The Qian et al. experiment was conducted at an ambient temperature of 20°C, whereas the simulation is run for body temperature (37°C), therefore some degree of error is to be expected.

Table 5.1 - Material properties of superelastic Nitinol in the ANSYS Workbench interface

Properties of Outline Row 4: Nitinol

	A	B	C	D	E
1	Property	Value	Unit		
2	Material Field Variables	Table			
3	Density	6.45	g cm^-3		
4	Isotropic Elasticity				
5	Derive from	Young's Modulus and Poisson's...			
6	Young's Modulus	39500	MPa		
7	Poisson's Ratio	0.33			
8	Bulk Modulus	3.8725E+10	Pa		
9	Shear Modulus	1.485E+10	Pa		
10	Tensile Ultimate Strength	900	MPa		
11	Superelasticity				
12	Sigma SAS	320	MPa		
13	Sigma FAS	385	MPa		
14	Sigma SSA	120	MPa		
15	Sigma FSA	60	MPa		
16	Epsilon	0.054	mm mm^-1		
17	Alpha	0.01			

The results of the analysis are contours of the equivalent von Mises stress and equivalent total strain on the plate body (Figures 5.4-5.7) and two force measurements (maximum force during loading and primary lower plateau force), for each plate. The transformation of the plate is marked on the stress strain curve of Figure 5.3.

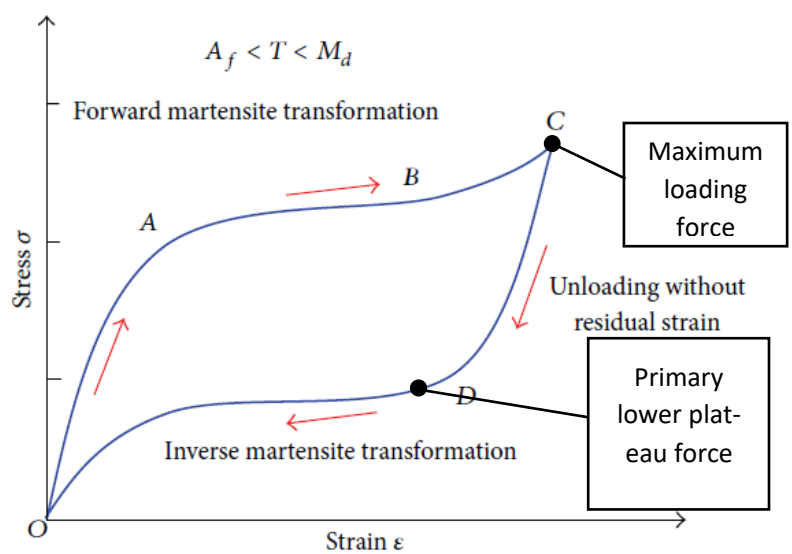

Figure 5.3 – Location of force measurements on the stress-strain hysteresis loop of superelastic nitinol

The loading and unloading forces reflect the difficulty of deforming the plate to the desired displacement and the compression force it will be able to produce. The start of the lower plateau area is selected, to indicate the force the plate can produce over an extended period of time and compare it with the force a DCP produces. Generally, lower maximum loading forces and higher lower plateau forces are preferred.

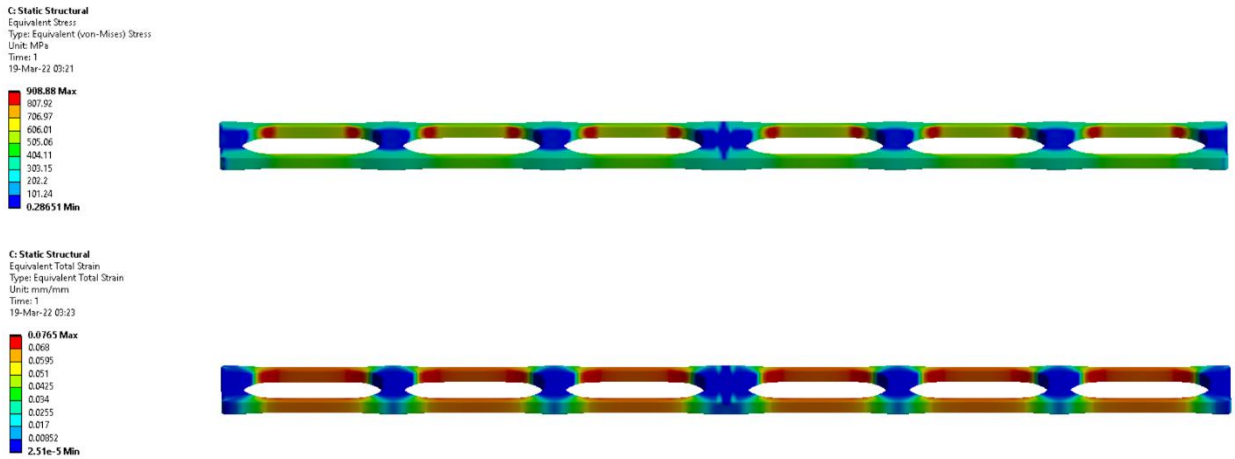

Figure 5.4 - Maximum equivalent von Mises stress and equivalent strain contours for the 6 oval slots SCP configuration in the ANSYS Static Structural interface

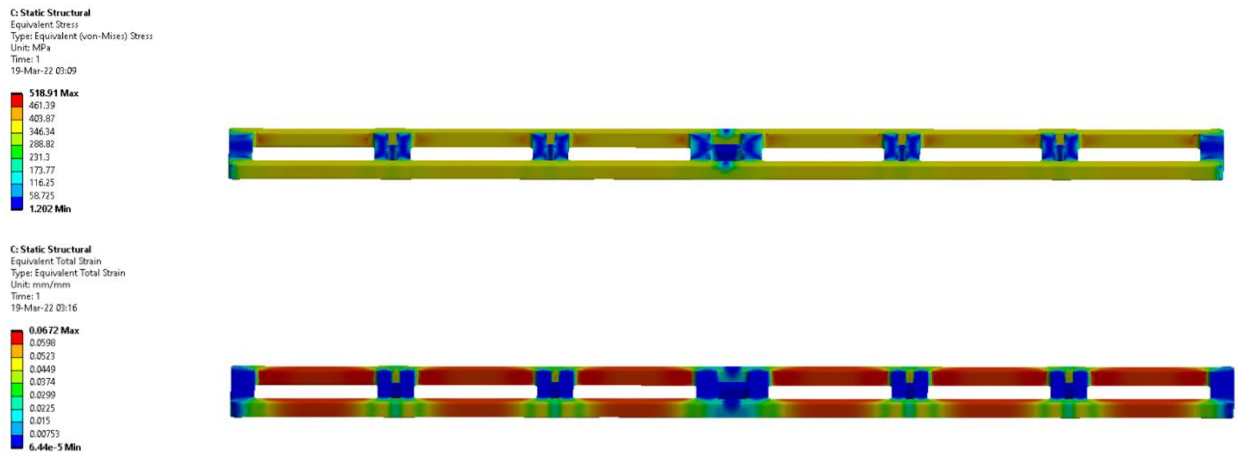

Figure 5.5 - Maximum equivalent von Mises stress and equivalent strain contours for the 6 rectangular slots SCP configuration in the ANSYS Static Structural interface

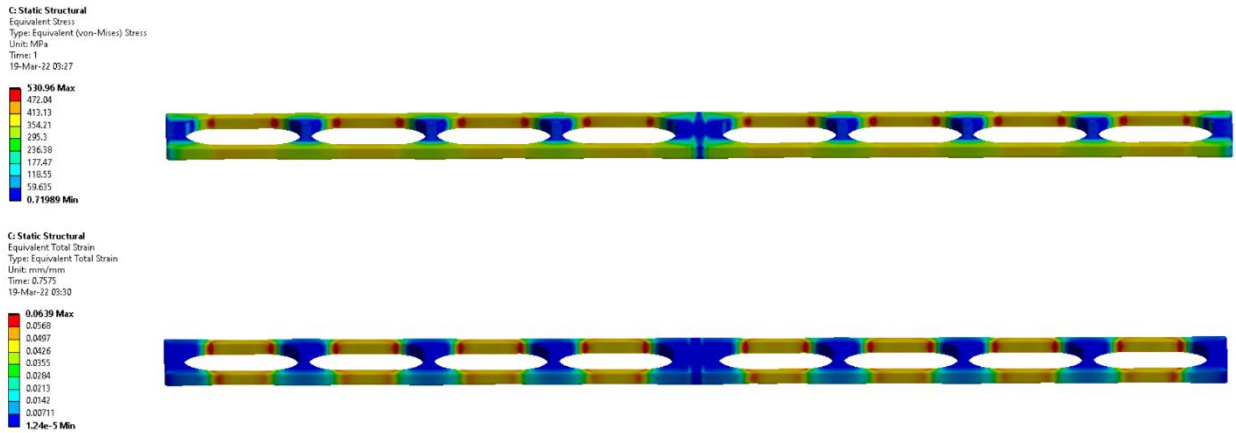

Figure 5.6 - Maximum equivalent von Mises stress and equivalent strain contours for the 8 oval slots SCP configuration in the ANSYS Static Structural interface

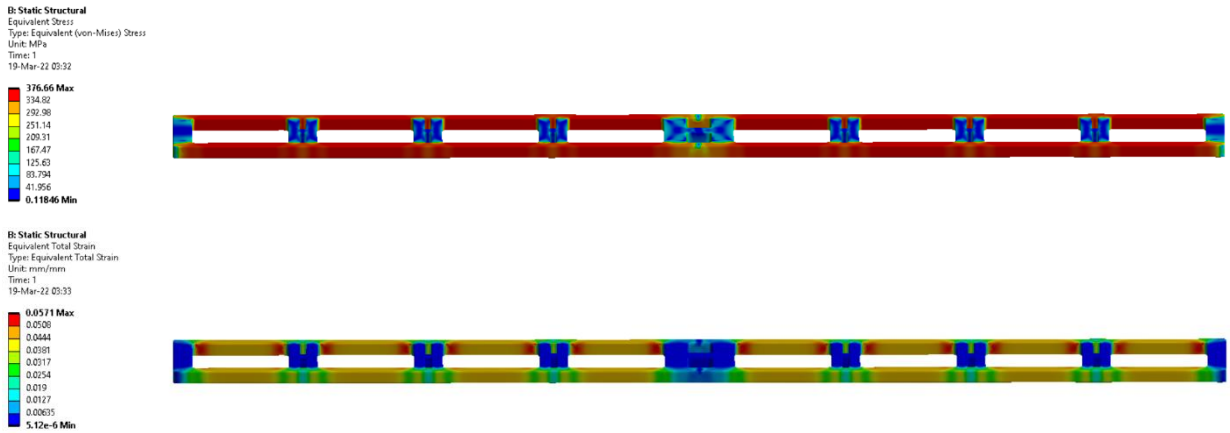

Figure 5.7 - Maximum equivalent von Mises stress and equivalent strain contours for the 8 rectangular slots SCP configuration in the ANSYS Static Structural interface

The results for maximum stress and strain at 6mm total deformation, as well as the forces, are presented in detail in Table 5.2.

Table 5.2 – Values of maximum stress, maximum strain, maximum force and lower plateau force of the four screw slots configurations for the SCP

Plate configuration	Maximum stress (MPa)	Maximum strain (mm/mm)	Maximum force (N)	Lower plateau force (N)
6 oval slots	908.88	7.65	3469.5	1249.6
6 rectangular slots	518.91	6.72	2524.9	866.2
8 oval slots	530.96	6.39	2646.6	939.8
8 rectangular slots	376.66	5.71	2437.9	798.01

It is apparent that 8-slot configurations perform better than 6-slot ones and rectangular slots perform better that oval slots. The overall best configuration is the 8-slot plate with rectangular slots, which for the same deformation develops the lowest stress, strain and maximum deformation force, but also the lowest lower plateau force. The low stress and strain indicate that the plate can be safely deformed even more than 6mm, thus being able to close larger fracture gaps and produce larger compression forces. Consequently, this configuration is selected, although the 8 oval and 6 rectangular slots are still viable options. The dimensioning of the slots is dictated

by the specifications for outer dimensions of compression plates and for the desired deformations. The length of the slots areas is crucial, since they are the only areas of the plate that are deformed. In line with the deformation specification, the slots are designed at 14.5mm in length, for a total slot length of 116mm, which ensures strains in the order of 5% at 6mm deformation. The width of the slots is 10.5mm to accommodate the sliding mechanism with respect to the width restriction imposed by the maximum dimensions of the titanium case. Finally, the supports between the slots are designed to prevent stress concentration in the corners and buckling of the sides.

5.1.2. Material properties and compression force

The lower plateau forces calculated in the simulation are comparable to the 800-1000 N estimations for the compression force produced by the DCP. Before progressing with the finalization of the design for the SCP, it is of utmost importance that the computational models for the DCP and SCP are validated by real-life tests. For this reason, two series of experiments are carried out, corresponding to each of the relevant parameters. The first series is concerned with the mechanical properties of superelastic nitinol and the second is dedicated to measuring the compression force of a DCP. A third series of experiments constituting a proof of concept application for the SCP is also planned, however it is not included in this study.

5.1.2.1. Mechanical properties

The mechanical properties testing is comprised of two experiments, a tensile test to failure (Image 5.1) and a three-point bending test to failure (Image 5.2). A loading-unloading hysteresis test is also planned, but it is not included. For each test, two specially designed test specimens (Image 5.1) are cut from a 350x230x3mm Nitinol sheet, in accordance to the relevant ASTM regulations (E8-2016a, E290-14, E466-15). The selected method of cutting is water jet cutting, which offers good precision without surface hardening or thermal fatigue, which could compromise the properties of the material.

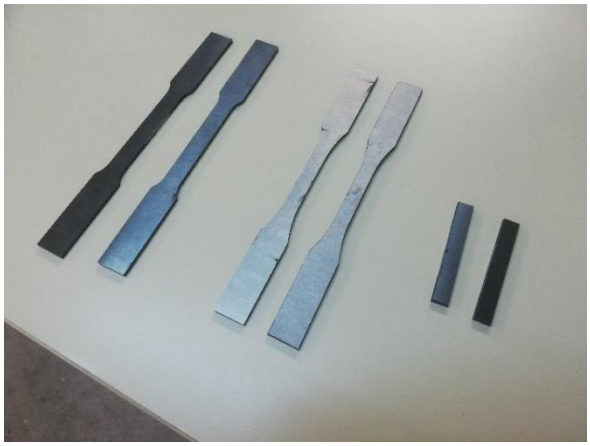

Image 5.1 – Test specimens for tensile test (left), loading-unloading test (middle) and bending test (right)

All tests are performed on an INSTRON 4482 testing machine, with a loading rate of 5 mm/min. The gauge length for the tensile and loading-unloading tests is 50mm and the span length for the three-point bending test is 30mm. Due to cutting imperfections in the test specimens, the results correspond to the higher-quality and thus more representative specimen, however the stress and load values could be underestimated. An iteration of the experiment with more precise specimens should be performed to extract reliable results. Additionally, the tension was performed without a strain gauge to measure deformation accurately, accounting for slippage at the clamps and deformation of the specimen areas outside of the gauge length.

Image 5.2 – INSTRON 4482 testing machine with tension test specimen clamped

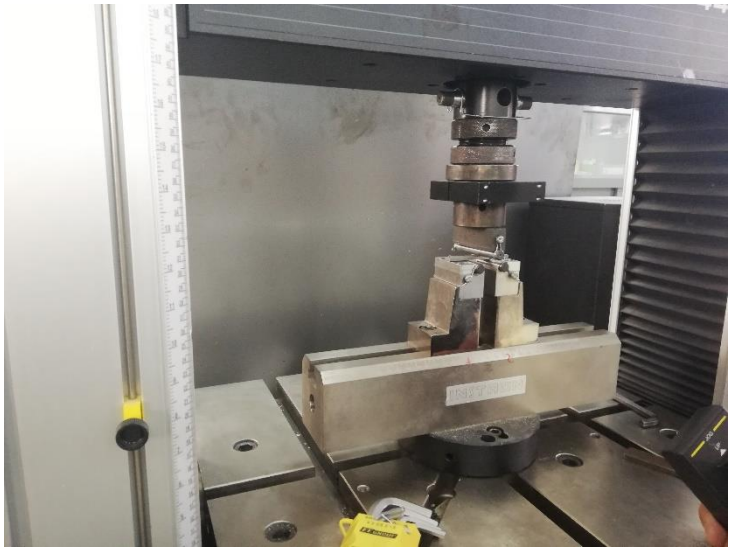

Image 5.3 - INSTRON 4482 testing machine with compression test specimen placed

As a result of the aforementioned inaccuracies, the strain output at failure is abnormally high, approaching 24%. To amend this, a finite element model of the tension test is constructed in ANSYS Static Structural, to provide estimates for the true strain values. A fixed support is placed on one end of the specimen to simulate the fixed clamp of the testing machine and a displacement is placed on the other (Figure 5.8). The displacement is increased linearly up to the 12.25mm maximum displacement measured by the machine.

Figure 5.8 - Loading conditions for the tension test specimen model in the ANSYS Static Structural interface

The mesh is generated using the Patch Conforming method with tetrahedral 0.5 mm elements and soft behavior. The material properties for Nitinol are derived from the findings of Qian et al. [54]. The results of the simulation are directional deformation and strain contours at the point the simulation ended (Figure 5.9). The load calculated at this point is 22.2 KN, which is lower than the 28.5 KN measured by the testing machine. Estimating the deformation of the gauge length by the simulation results and extrapolating it for the load of the machine, a strain value of 10.35% at failure is obtained. Adjusting the measurements to match this value, the corrected stress-strain curve for the tension test is presented in Figure 5.9. The stress measurement at failure is **769 MPa**.

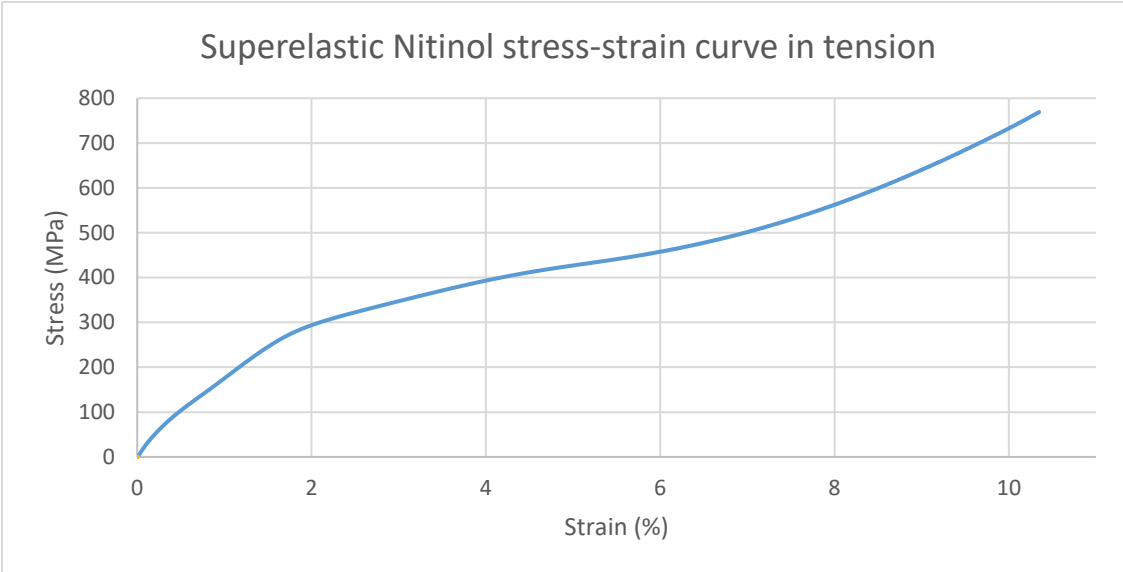

Figure 5.9 – Experimental tension stress-strain curve for superelastic Nitinol with corrected strain values

The resulting curve for tension is very similar to the Qian et al. [54] curve, therefore the experimental results attest to the accuracy of the material model used in previous simulations.

For the bending test, the load measurement at failure is 4281N. Using the formula 5.1 for the bending stress and treating the specimen as a rectangular beam, the maximum bending stress value of **428MPa** is obtained.

$$\sigma_b = -\frac{M*y}{I_c} \quad (5.1)\ ,$$

Where:

- M=64.21Nm: bending moment applied by the machine
- y=1.5mm: distance from the centroid to the top extreme fiber
- I_c=2.25*10^{-11} m^4: moment of inertia about the x-axis

Adjusting the measurements by associating the maximum stress measurement with the calculated maximum stress, the corrected stress-strain curve for the bending test is presented in Figure 5.10.

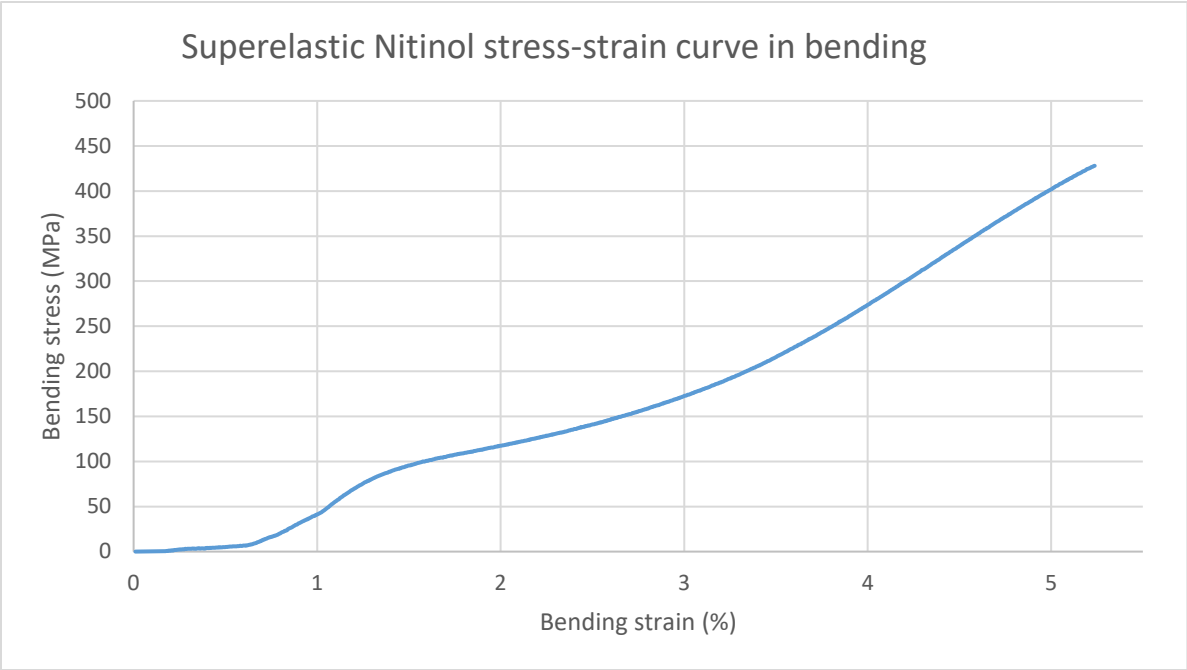

Figure 5.10 - Experimental bending stress-strain curve for superelastic Nitinol with corrected stress values

The curve is very similar to the tension curve and the stress and strain values also match the tension measurements and the data available in the bibliography.

In both tests, brittle fracture without necking was observed (Image 5.4), which presents a contrast to the failure type of other highly ductile and superelastic materials. It is to be expected though, due to the martensitic nature of Nitinol under large strains.

Image 5.4 – Brittle fracture of Nitinol

5.1.2.2. DCP compression force

To measure the compression force, an experimental procedure is set up to simulate the surgical procedure of a DCP fracture fixation. In the first stage of the experiment, the bone model used is a 3D printed PLA model of the femur bone that was used for the finite element analysis. The model is cut into two fragments using a saw and the fragments are stabilized with a typical 10-hole wide DCP and 4.5mm cortical screws (Image 5.5).

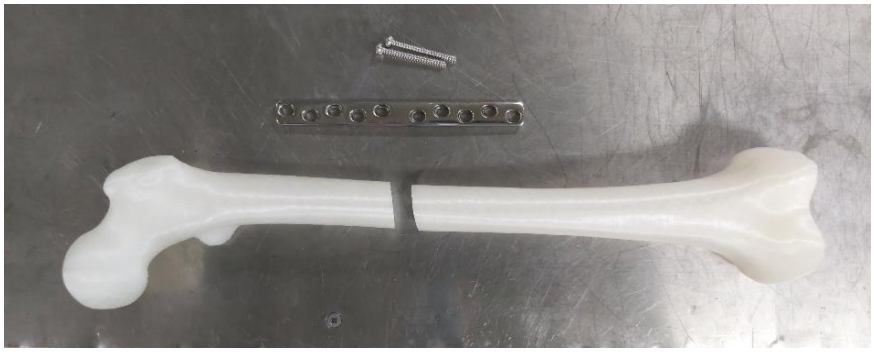

Image 5.5 – Split PLA femur model, 10-hole wide DCP and two 4.5mm cortical screws

The bone fragments are mounted on a vise and the plate is positioned on the lateral side, symmetrically and perpendicular to the fracture line (Image 5.6). The plate is held into place and 3.5mm holes are drilled with the aid of a drill guide to place the holes eccentrically on the DCP slots, so that the screws can produce compression (Image 5.7).

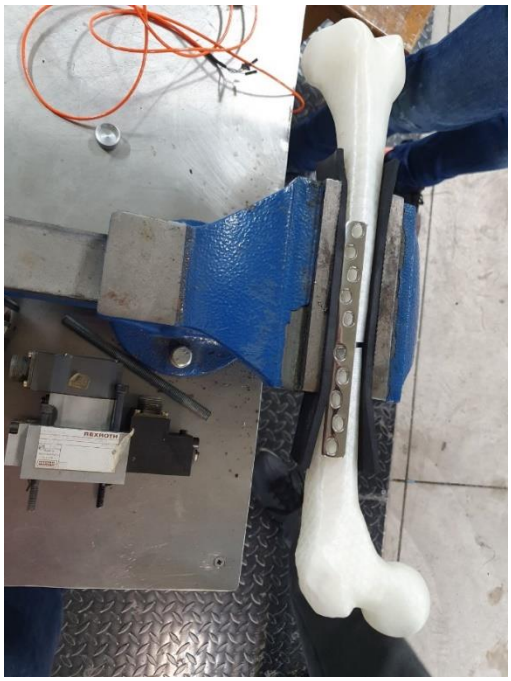

Image 5.6 (left) – Placement of the DCP on the 3D printed femur model

Image 5.7 (right) – Use of a drill guide for positioning of the holes

Subsequently, 20mm blind holes are created on the fracture surface of both fragment, using a milling machine. Each hole is fitted with an aluminum cup cut with a lathe machine from a 30mm aluminum rod (Image 5.8) and a button type compression load cell is placed between them (Image 5.10). The two cups are of varying depth, to ensure that the load cell stays in place on one fragment and that it contacts the cup surface of the other fragment perpendicular to the button for measurement accuracy. The measuring capacity of the load cell is 200 Kg and its specifications sheet is available in Appendix III.

Image 5.8 – Cutting of an aluminum cup from a rod using a lathe machine

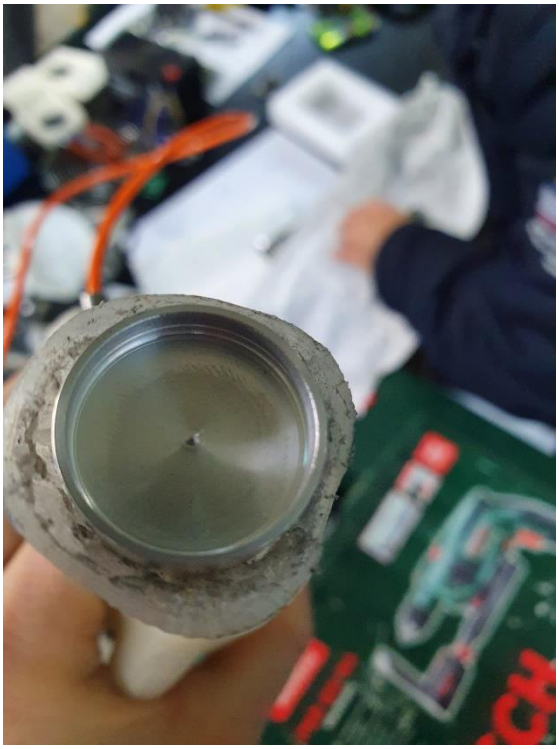

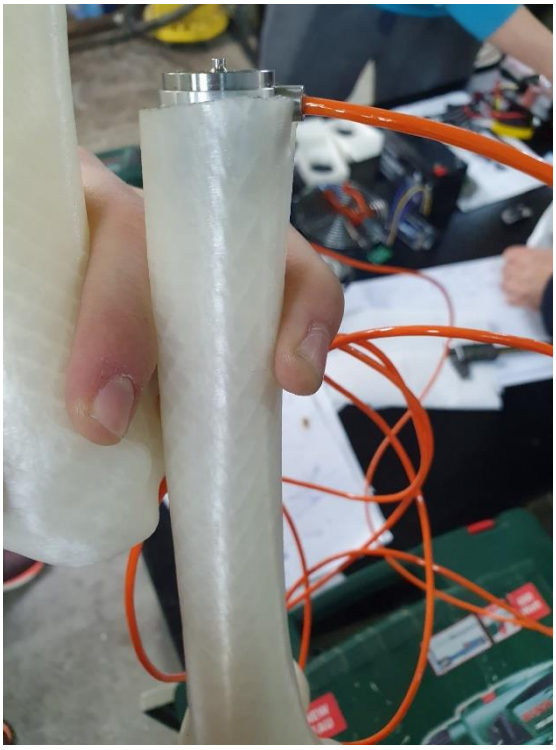

Image 5.9 (left) – Aluminum cup inside a slot in the 3D printed bone fragment

Image 5.10 (right) – Placement of a button type load cell inside the aluminum cup in the 3D printed bone fragment

The load cell contains a diaphragm and four strain gauge elements connected in a Wheatstone bridge configuration. One or more resistors have variable resistance and detect changes in strain. Usually, a pair of opposite resistors measures compression strain and the other pair measures tension. In a compression load cell like the one used in the experiment, the single active strain sensor is wired in compression. In such a configuration with a variable resistor and three fixed-value resistors as shown in Figure 5.11, the strain measurement is given by formula (5.2), where GF is the gauge factor of the sensor. [56]

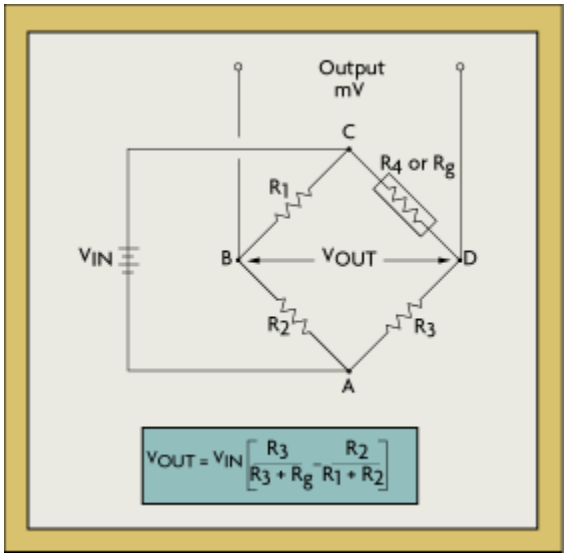

Figure 5.11 – Wheatstone bridge resistors configuration used in load cells [56]

$$e = \frac{(\frac{\Delta R_g}{R_g})}{GF} \quad (5.2)$$

The output of the sensor is the voltage V_{out}. This output is read and interpreted using a simple circuit of an HX711 analog to digital converter (ADC) and an Arduino Uno microcontroller. The load cell is connected to the ADC and the ADC to the Arduino, as shown in Image 5.11.

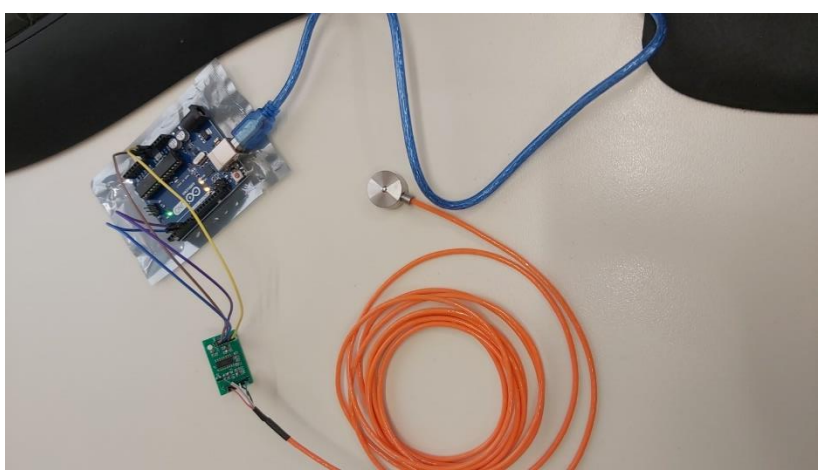

Image 5.11 – Load cell, ADC and Arduino microcontroller configuration

The Arduino is plugged into a computer and two programs for calibration and measurement extraction are loaded. The program codes are available in Appendix III. The calibration program is run and the load cell is initially calibrated with a known 10 Kg plate. Consequently, the measurement reading program is run and four cortical screws are screwed onto the plate and bone in two slot pairs, nearest and furthest from the fracture (Image 5.12). Due to the presence of the load cell, it is not possible to place screws on the pair of slots nearest to the fracture line. Each pair is tightened separately and the force measurements are obtained.

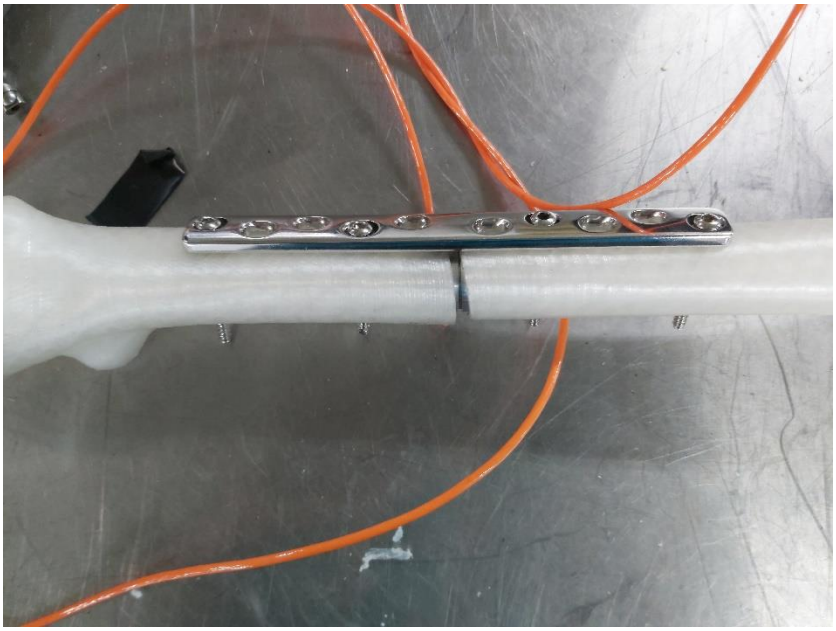

Image 5.12 – DCP mounted on the 3D printed femur fragments with two screw pairs

Table 5.3 – Compression force measurements from the load cell for the DCP with one or two screw pairs fixed

Screws tightened	Compression Force (Kgf/N)
Outer pair	12.36/121.25
Outer + inner pair	38.24/375.13

As expected, with only four screws fixed, the force value is lower than the known estimates. Given that that the placement of the holes was performed without relevant experience, a bone substitute with vastly different mechanical properties than bone tissue was used and that in 10-hole DCP applications all or 8 screws are used, the measurements obtained are assessed as comparatively accurate. An improved iteration of the experiment is planned, where the plate is applied on a bovine femur and is installed by a trained surgeon using all available screw positions. The improved surgical technique and natural bone tissue are predicted to produce highly reliable final results for the compression force, which should be similar to the estimates.

5.1.3. Sliding inserts

The selected sliding mechanism is rectangular inserts that are fitted into corresponding slots in the SCP and provide housing for the screws. The inserts have holes deeper than the screw heads and a matching side to ensure uniform application of the adjusting force and precise axial movement of the screws across the plate axis. At present, the screws used are the normal 4.5mm cortical screws, nevertheless it could be beneficial in the future to design custom cortical screws with modified heads, to improve the screw-insert contact and force transmission. With the described configuration, the screws rest on the sliding inserts while being screwed on the bone, thus pressing the inserts on the bottom of the titanium case, and connecting them together. The friction force produced in the bottom of the case is estimated in the order of 800N for 8 screws and typical screwing torque of 2-3Nm and could be detrimental to the sliding capability of the inserts. Even though the SCP can produce compression forces considerably higher than this value, the lower plateau force in normal conditions is in the same range. A low friction coating on the surfaces of both sliding inserts and titanium case, such as TiN can reduce the friction coefficient to as low as 0.15, combining exceptional bonding and wear resistance. However, even without coating, the vibrations created by walking are expected to overcome any sticking effects and provide the inserts with enough clearance to slide under the compression of the SCP. The design of the sliding inserts is presented in Figure 5.12.

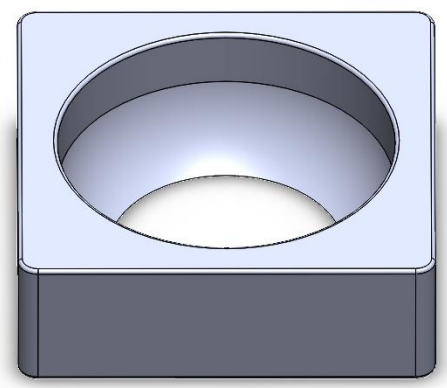

Figure 5.12 – Sliding insert design

Finally, the SCP design is completed as a combination of the aforementioned features (Figure 5.13). In each end of the plate, two **2.5mm** holes are designed, for the tensioning sustain tool to be able to hold the plate under tension during the surgery. The material of choice is superelastic Nitinol with **A_f=0°C**, martensite elastic modulus **E_m=40GPa** and austenite elastic modulus **E_a=80GPa.** The desired properties are achieved with a mixture of **50.8% Ni – 49.2% Ti**.

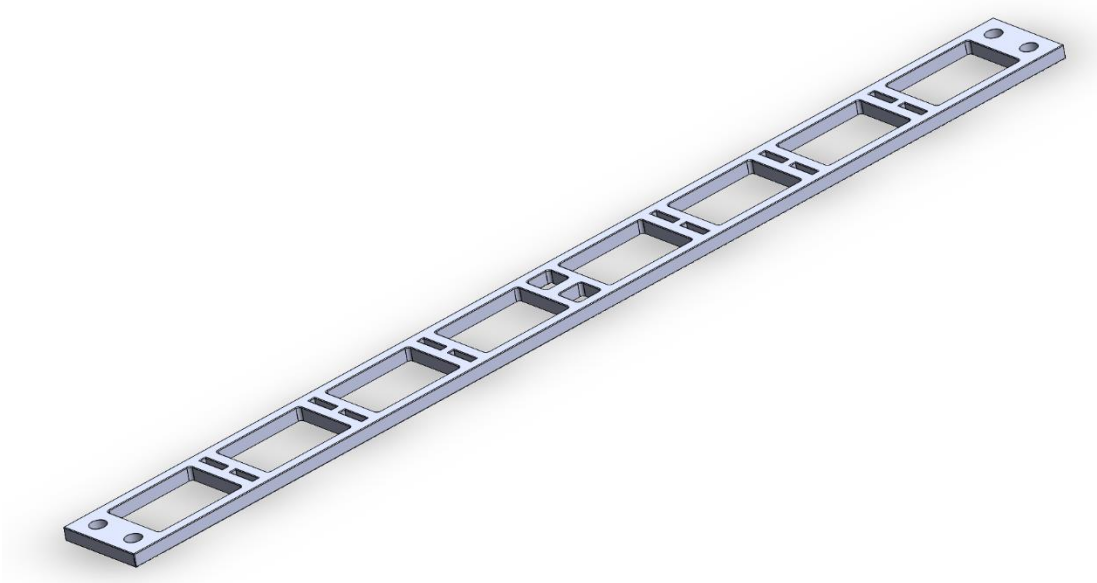

Figure 5.13 – Superelastic compression plate (SCP) design

5.2. Tensioning tool

5.2.1. Design specifications and conceptual design

In this section the specifications that must be met by the tools will be presented as well as the conceptual design of the tool, i.e., the early thoughts that led to the construction and the final form of the tool.

The design specifications are the following:

- Tensile loading of the Superelastic Compression Plate (SCP) in discrete points (along its length) based on the plate overall length and size as well the severity of bone fracture.
- Sustained tension of the SCP in discrete points, as well as controlled unloading
- Adjustability of the tools to various SCP sizes.
- Force applied on each end of the plate uniformly.
- Ability to operate during surgical procedures.
- Compatibility with the surgical procedure (i.e., not interfering with the screwing of the cortical screws, dimension restrictions).

- Not complicated operation
- Relatively low cost

The latter two specifications are not critical for the design, but rather preferences at this stage.

The initial thought that was derived from the conceptual design was to split the workload to two different tools, one for tensioning and one for sustaining it.

The preloading tool is designed to resemble a tensile machine, much smaller in size and easier to operate by a doctor, as it does not require any specialization in engineering. It is desirable to be mounted (permanently or semi-permanently) on a bench. There are various ways to implement the pretension mechanism ranging from mechanically actuated (manual, electrical or hydraulic) to pre-tensioned by thermal expansion (not of the plate, but of a piece that is kinematically coupled to the plate). However, for such designs, an autonomous mechanical mechanism is preferred. In Figure 5.14, a concept of the tool is provided.

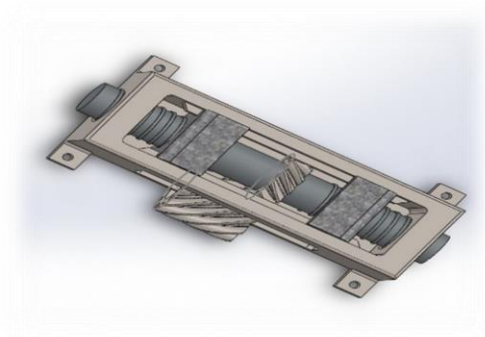

Figure 5.14 – Concept for the tension tool

The sustaining tool is created with the purpose of ensuring that the preloading caused by the first tool is sustained until the surgeon finishes applying it on the patient. Its working principle should be simple, easily understood, and the tool should not interfere with the surgical procedure. Based on the aforementioned, the shape and form of the tools is materialized and their design is detailed separately for each one.

5.2.2. Design and calculation of the tension tool

The analysis for the tension tool with detailed calculations is performed and will be divided into the following categories: tensile loading mechanism, power input, supports and fixation, gear components, clamp and additional complementary elements.

5.2.2.1. Tensile loading mechanism

The most important element of the tensioning mechanism is the power screws, as they are responsible for converting the required deformation force into an achievable torque as well as for the motion that requires elongation at the SCP. The mechanism is designed to use two lead screws against one. This solution favors the stress applied at each screw, but mainly it is used to be able to remove eccentricities in relation to the level of attraction of the plate. To define the specifications of the lead screws, the torque that should be applied on each screw as a function of its nominal diameter must be studied. The torque is given by the following formula:

$$T_{screw} = F\left[\frac{d_m}{2}\left(\frac{L + \pi f d_m \sec(a)}{\pi d_m - fLsec(a)}\right) + \frac{f_c \overline{d_c}}{2}\right] \quad (5.3)$$

Where:

- $F = 1500N$: the force applied on each screw
- d_m: the mean diameter of the thread which is different for each one
- L: the linear displacement of the screw in one turn (lead), which in single-screw screws is equal to the pitch
- $f = 0.14$: the coefficient of friction for a well-lubricated surface
- α, the angle of the thread (60 ° for metric thread, 30 ° for trapezoidal and 0 ° for rectangular)
- $f_C = 0.14$: the coefficient of friction between the screw and the bushing
- $\overline{d_c}$: the mean friction radius of the screw against the bushing

The calculations are performed for 3 types of thread, trapezoidal (**DIN 103**), metric (**DIN 13-1**) and rectangular (not standardized). The rectangular thread was studied to compare the stress that is applied on the screw and the formulas with small corrections are applied to the other screw types. It is an iterative process where different sizes of diameters are inputted and the torque required to be supplied to the system to perform the tensile elongation is obtained. In addition, the torque of the mechanism is calculated, which must be negative for the load not to be able to self-unscrew, which would be detrimental for the application. Finally, the screw stresses and strains must be studied before the final diameter selection is made. We consider an intensive element at the base of the thread (root) of the screw which receives the following stresses:

- Compressive stress on the screw body:

$$\sigma_y = \frac{F}{A} = \frac{F}{\pi\frac{d_m^2}{4}} \quad (5.4)$$

- Shear stress on the body of the screw:

$$\tau_{yz} = \frac{16T_{screw}}{\pi d_r^3} \quad (5.5)$$

- Thread s shear stress:

$$\tau_{zx} = \frac{3*0.38F}{2\pi d_r n_t h_t} \quad (5.6)$$

- Bending stress of the thread:

$$\sigma_x = \frac{3*0.38F}{\pi d_r n_t h_t} \quad (5.7)$$

Where:

- d_r: diameter of the thread root
- n_t: number of stressed threads
- h_t: thread height

Having calculated the stresses, using the equivalent von Mises stress in the three-dimensional plane, the maximum stress on the screw is calculated:

$$\sigma_{eq_{vM}} = \frac{1}{\sqrt{2}}\sqrt{\left(\sigma_x - \sigma_y\right)^2 + \left(\sigma_y - \sigma_z\right)^2 + (\sigma_z - \sigma_x)^2 + 6(\tau_{yx}^2 + \tau_{xz}^2 + \tau_{zy}^2)} \quad (5.8)$$

Then this stress is multiplied by a safety factor of, FOS = 2 and the total stress of the screw is calculated:

$$\sigma_{eq_{vM_{tot}}} = \frac{1}{\sqrt{2}}\sqrt{\left(\sigma_x - \sigma_y\right)^2 + \left(\sigma_y - \sigma_z\right)^2 + (\sigma_z - \sigma_x)^2 + 6(\tau_{yx}^2 + \tau_{xz}^2 + \tau_{zy}^2)} * FOS \quad (5.9)$$

In addition, as the screw will have a diameter reduction for bearing reasons, low values of the nominal diameter are clearly discarded for this reason. Therefore, a screw with the following characteristics is selected: T $r18x4\ (100)\ RH/LH$, $\sigma_{eq_{vM_{tot}}} = 52.4\text{MPa}$, $T_{screw} = 6.2Nm$, $T_{screw_{Lock}} = -1.37\ [Nm]$

The screws have both right- and left-hand thread so that there are 2 sliding elements on each screw that perform linear movement during the operation of the mechanism.

The sliding element is the link between the power input and output. It is connected to the guides, lead screws and is the frame on which the clamp is attached to, therefore it has a key role. The linear motion of the sliding element applies the elongation required on the SCP. The sliding element is a piece of rectangular cross-section with certain hole configurations for the power screws axes. To study the loading conditions on the sliding element, the reaction of the tensile force as well as the reaction of the lead screws are considered. The sliding element is also subject to bending moment caused by the point load, but it can also be subject to bending as if it was a fixed support in case there is interference between the sliding element and the linear guides. It is a primary design concern not to interfere with the operation of the element due to its friction with the guides. Two cases are studied, for the mechanism (dynamic equilibrium) and the basic equilibrium. From the analysis of the mechanism, an estimation of the magnitude of the maximum torque exerted at the midpoint is calculated, as well as an order of magnitude for the deflection noted at this cross section (Figure 5.15). For the calculation of the deflection, the Castigliano theorem with formulas (5.10)-(5.13) is used without eliminating the terms of the transverse shear that occurs, as it is not correct to assume that the length of the element is significantly larger than its width and height.

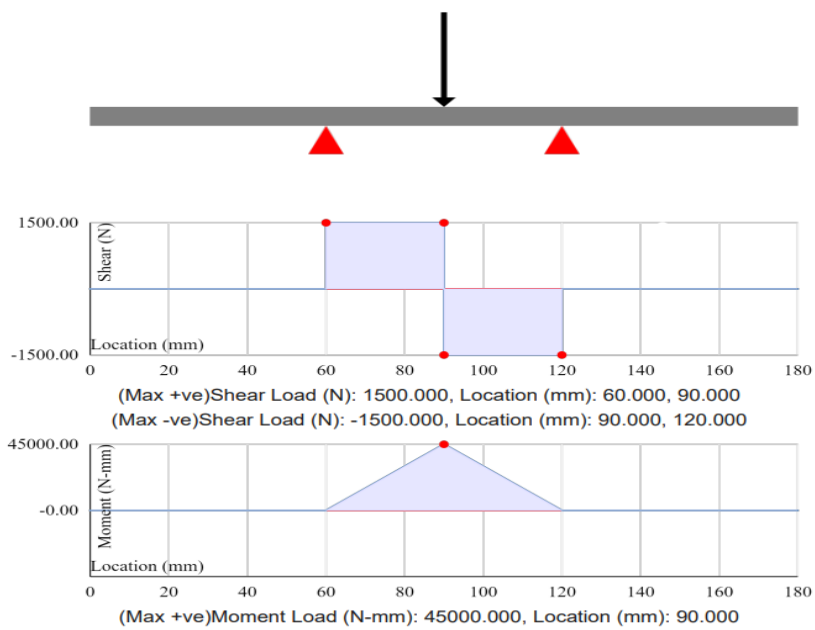

Figure 5.15: NQM Diagrams of the Sliding Element in the OptimalBeam interface

$$\delta = \frac{\partial U_{total}}{\partial F} \quad (5.10)$$

$$U_{bend} = \int_0^{Length} \frac{M^2}{2EI} dx \quad (5.11)$$

$$U_{shear} = \int_0^{Length} \frac{CV^2}{2AG} dx \quad (5.12)$$

$$U_{total} = U_{bend} + U_{shear} \quad (5.13)$$

Where:

- δ: deflection
- $M = M(x)$: bending Moment along the x axis (length)
- V: shear force applied
- $C = 1.2$: shear coefficient for rectangular cross sections
- $E = 200GPa$: steel's Young modulus
- $G = 70GPa$: steel's shear sodulus
- A: $c$ross section area
- I: Second moment of Inertia of the Cross Section. It was calculated for a rectangular cross section and a correction factor of 0.7 was established to account for the holes that we used.

This analysis also results in the maximum deflection of the sliding element (for any type of steel, with very small fluctuations in price) which is calculated equal to $\delta_{max} = 6[\mu m]$

Focusing onto the original model, it is observed that (by applying basic geometric relations), a deflection equal to the above, does not cause interference between the guides and the element. However, this case will be studied as well in case of unwanted outcomes. The total stress according to Mises that is applied on the sliding element using the stresses noted on (Figure 2) is:

$$\sigma_{eq_{vM}} = \frac{1}{\sqrt{2}} \sqrt{\left(\sigma_x - \sigma_y\right)^2 + \left(\sigma_y - \sigma_z\right)^2 + (\sigma_z - \sigma_x)^2 + 6(\tau_{yx}^2 + \tau_{xz}^2 + \tau_{zy}^2)} = 140MPa \quad (5.14)$$

To calculate the stress, a safety factor equal to 2 (i.e., FOS = 2) was considered as well as a stress concentration factor equal to 2 $(K_t = 2)$. This stress is located on the critical cross section (which is in the middle of the element) As mentioned above, a case study is conducted in case drivers are forced to sustain bending loading. This structure is statically indeterminate and is solved using the superposition method (for axial forces) and the Castigliano theorem (Equations 3.8 to 3.11). The result is presented graphically in Figure 5.16

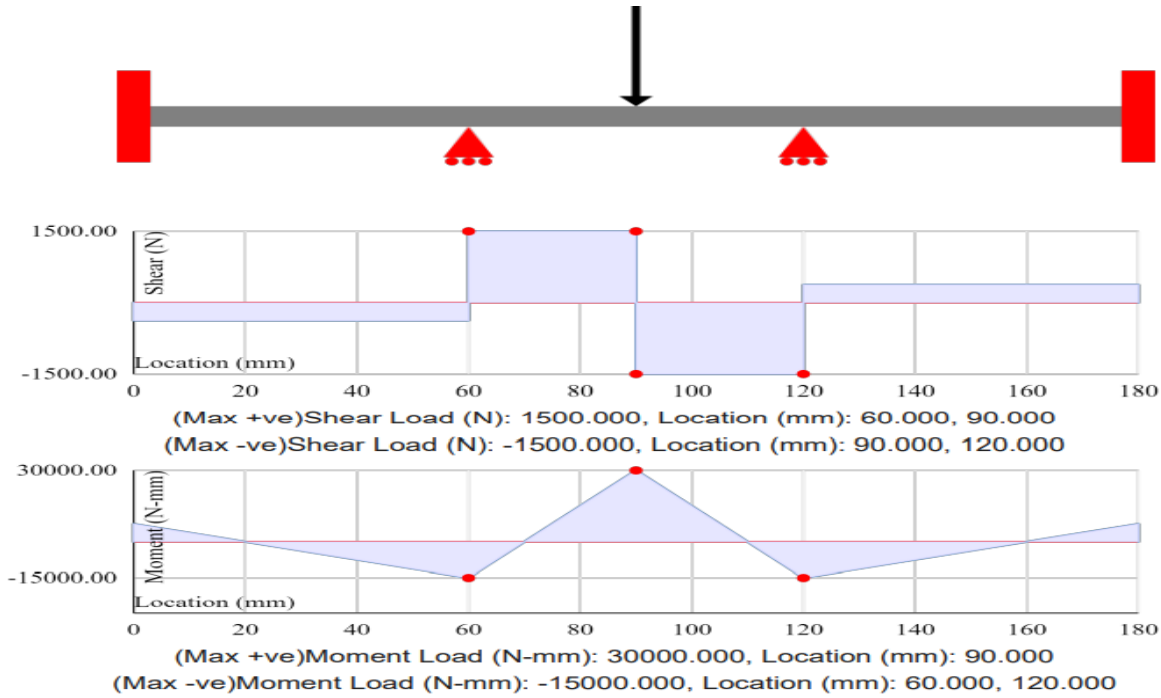

Figure 5.16 - NQM Diagrams of the Statically Indeterminate Element

It is observed, by comparing the results of Figures 5.15 and 5.16, that this case is less damaging for the element. Therefore, it is deducted that the element won't be subjected to worst stress scenarios than the ones calculated and the design is completed (Figure 5.17). The specifications are listed in Table 5.4.

Table 5.4 – Sliding element dimensions

Dimension	Value (mm)
Length	180
Height	35
Width	20
Clamp hole diameter	14
Screw holes diameter	18

Guide holes diameter	22
Screw shaft nominal distance	30
Linear guides nominal distance	~80

The material of the sliding element should be a steel of at least medium quality with a yield strength greater than **250 MPa**.

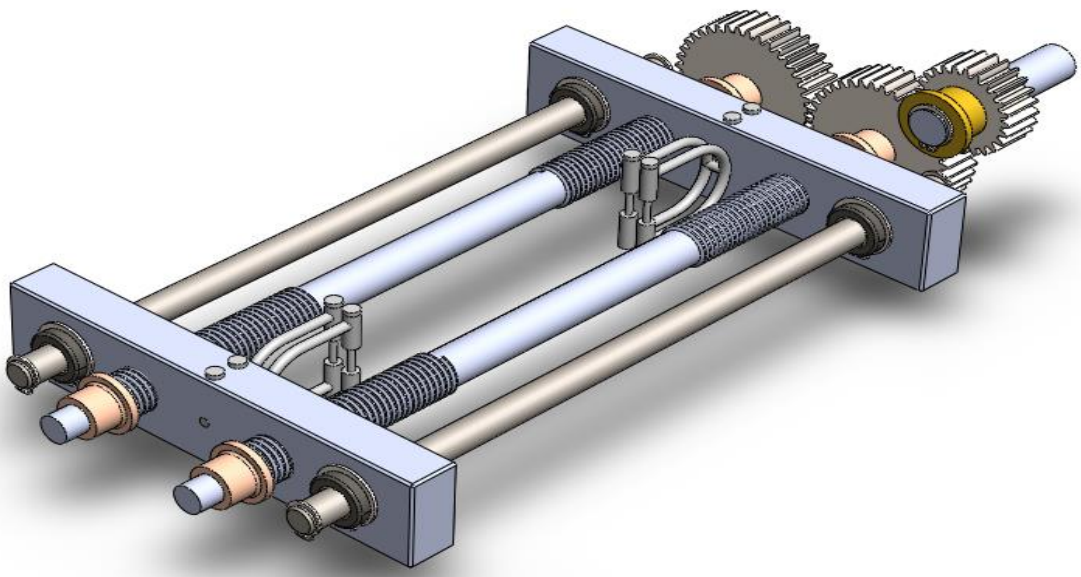

Figure 5.17 - Tension mechanism with clamp attached

The Linear Guides are the next essential part of the mechanism and they are responsible for the controlled and smooth driving of the sliding element. The guides are simple rods supported on sliding connectors mounted on the sliding element for friction reduction and better driving quality. Their loads are simply calculated from the aforementioned reaction of the sliding element, therefore the moment and shear force on the guides are obtained from Figure 5.16 and are calculated as $\mathbf{M_{slider}=7.5Nm}$, $\mathbf{V_{slider}=300N}$.

For the shear stress:

$$\tau_{slider} = \frac{V_{slider} S_y}{I_{yy} b} \rightarrow \tau_{slider_{max}} = \frac{4F}{3A} \ (5.15)$$

$$\sigma_{slider} = \frac{M_{slider}}{I_{yy}} * y \ (5.16)$$

The equivalent von Mises strength is given by the following formula:

$$\sigma_{vM} = \sqrt{\sigma_{slider}^2 + 3 * \tau_{slider}^2} \ (5.17)$$

Combining formulas (5.15) to (5.17), and assuming a $FOS_{slider} = 2$ it is deducted that the following dimension is accepted (i.e., the guide does not suffer from stress that exceeds its yield strength and any strains are within acceptable limits): **d_{slider}=12mm**, **σ_{vM}=89MPa**

The above design allows for tensile loading of the SCP, as well as for safe management of the required forces. For the mechanism to function as intended, the two lead screws must perform a rigid body motion and not present lag to one another. This will be achieved by using two identical gears, with a specific axial distance, which will be located on the shaft of the screws.

5.2.2.2. Power Input

The smooth input of power to the system as well as the ease with which the power is inserted are highly important parameters that the designer is called to achieve. Power must be supplied smoothly, and if the operation is done manually, it is desirable to provide for an easy operation. In this mechanism the operator must apply a tensile force of at most **3KN** on the plate. By the current design, so far, this force has been transformed into a torque of **8.5Nm** on the screw axis. The way with which the operator supplies the required torque is the item of study of the power input.

To achieve the said goal, two design solutions are implemented:

- Gear pair that lowers the transmission ratio.
- Force multiplier by using a ratchet to transform the force of the operator to torque on the gear shaft.

The torque applied by the operator is $T_{in} = 8.5 * i_{cg} = 5.2Nm$ (5.18), where i_{cg}: transmission ratio. Depending on the length of the ratchet that will be used, the required force will receive the following values (Figure 5.18).

$$F_{in} = \frac{T_{In}}{Lever}\ [N] \quad (5.19)$$

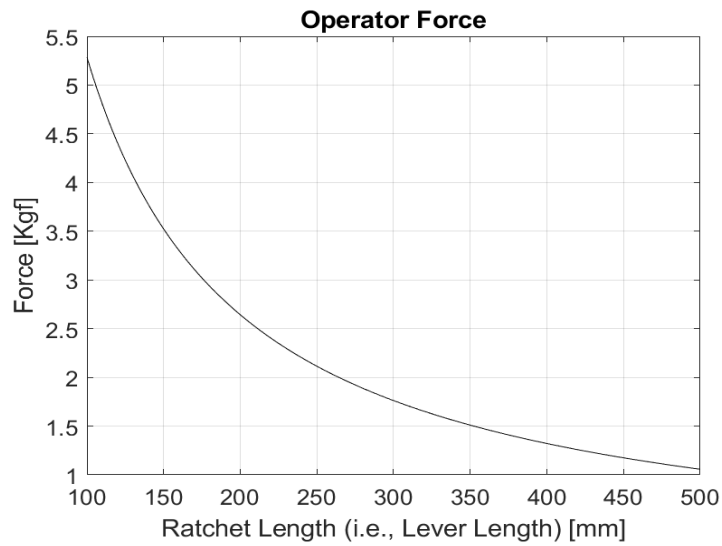

Figure 5.18 - Force – ratchet length diagram

It is obtained that for length values larger than $L = 200[mm]$ the input force receives low enough values for any average human. The end part of the ratchet is standardized under **DIN 3121**. A socket size equal to **3/8 "** is selected. The input shaft has a diameter of **16mm**. The forces acting on the shaft are considered negligible.

5.2.2.3. Supports and fixation

After the analysis of the mechanism and calculation of the input parameters, the analysis of the supports is performed.

As there is a need for certain elements to perform rotational movement, simple sliding bearings (bushings) are used. This choice is facilitated because it is slow-moving mechanism and lubrication is desired. The type of bushings selected is self-lubricated bronze – graphite bushings (Figure 5.19).

Figure 5.19 - Oilless self-lubricating bronze-graphite bushing

The bushings will be placed at the ends of each threaded shaft, to receive any loads and secure the shafts, as each screw has a reduction in its diameter at the point where it is supported. These specific elements do not require external lubrication, as they contain solid lubricant (graphite), widely used in both food industry and medicine. As a result, they present an ideal choice for surgical environments.

The bushings are analyzed by applying the uniform pressure theory (much like dry friction plates) in order to withstand the stress they might be subjected to, when under friction with compressive elements. In this case, the forces applied are not a concern. Apart from the stress magnitude, a strain (due to uniaxial compression) is calculated showing that the deformation is completely negligible, in the order of 0.2% and therefore the bushing operation is not obstructed.

These bearings are standardized under **DIN 4379** and their dimensions are presented in Table 5.5.

Table 5.5 – Bushing dimensions

Dimension	Value (mm)
Length[mm]	15
Inner Diameter[mm]	12
Outer Diameter [mm]	18
Flange Diameter[mm]	22
Flange Thickness [mm]	3

The shell of the mechanism receives minimal stress due to symmetry and forces cancelling out. Therefore, there is no need to study it extensively. Care is taken to place the configurations correctly for the bearings. In addition, the design is performed with the assembly of the construction in mind, which is why the housing is divisible. The bearings, as well as the guides, are placed on the housing. Since the guides do not need to be rotating, they can be secured with a tight fit by use of circlips. Furthermore, the housing has a base with threaded holes, so that it can be connected semi-permanently to a base or table in the surgery room.

Circlips are small rings that have an important role in securing the gear shafts against axial translation. In the design in question, the circlips are mounted on the guides (on either side of their mounting point), on the guide slots (to secure them against the sliding element) and then on the

gears, where the groove on the shaft does not lead to accumulating stress. The circlips are standardized under **DIN 471.**

5.2.2.4. Gear components

At this point the analysis of the gears will be conducted. Specifically, a pair of identical gears (synchronizing gears) and another wheel (convenience gear) were used to synchronize the movement of the lead screw.

To tackle the challenge of synchronizing the mechanism, a plethora of options regarding gear geometry is available. The technical specifications for the design are as follows:

- Least Number of Teeth: $Z_{min} = 18$
- Contact Ratio: $\varepsilon > 1.6$
- Transmission Ratio $i_{SG} = 1$
- Optimal shaft distance
- Fulfillment of modified cooperation principles

The algorithm chosen to solve this challenge is as such: For several standardized module values and for number of teeth ranging from the geometrical minimum of 18 to a logical maximum value of 40, pairs of gear are checked one by one, as to their fulfilment of the specifications. The shaft distance is directly proportional to the size of the gears (nominal shaft Distance for involute gearing), therefore it is deduced that only pairs with more than 24 teeth fulfill the requirements. Therefore, we are tasked to check which of those pairs fulfill all of the following cooperation principles for gear transmissions [57].

- Common module (per need of pitch equity)
- Law of gearing at effect (is fulfilled for involute gears).
- Positive radial clearance (is always fulfilled for nominal involute curve gearing teeth. $\Delta r = 0.25 * module$)
- Width Coefficient < 0.5. This variable was controlled by the design team and set equal to $C_s = 0.475$
- Contact Ratio > 1.4, but in this instance Contact Ratio > 1.6
- Condition of non-existence of cuts.

From the above conditions, only the latter two remain to be evaluated:

The contact section is calculated using the following equations:

$$CK_1 = \sqrt{r_{k2}^2 - r_{g2}^2 - (r_{02} \cdot \sin(a_0))^2}\ [m] \quad (5.20)$$

$$CL_1 = \sqrt{r_{k1}^2 - r_{g1}^2 - (r_{01} \cdot \sin(a_0))^2}\ [m] \ (5.21)$$

$$KL_1 = CK_1 + CL_1 \ (5.22)$$

Which can be used to calculate the contact ratio as shown below:

$$Contact\ Ratio = \frac{KL_1}{t_g} \ (5.23)$$

Where:

- r_{k2} $[m]$: radius of head circle of the $pinion$, equal to $r_{k2} = r_{02} + m_n$
- r_{g2} $[m]$: radius of basic circle of the $pinion$, equal to $r_{g2} = r_{02} \cdot \cos(a_0)$
- r_{02} $[m]$: radius of nominal circle of the $pinion$, equal to $r_{02} = z_2 * \frac{m}{2}$
- r_{k1} $[m]$: radius of head circle of the $gear$, equal to $r_{k1} = r_{01} + m_n$
- r_{g1} $[m]$: radius of basic circle of the $gear$, equal to $r_{g1} = r_{01} \cdot \cos(a_0)$
- r_{01} $[m]$: radius of nominal circle of the $Pinion$, equal to $r_{01} = \frac{z_1 \cdot m}{2}$,
- t_g: pitch of the basic circle,equal to $t_0 = \pi * m$
- m: module
- $a_0 = 20°$: angle of the involute curve

The condition of non-existence of cuts is formulated as follows:

$$\begin{cases} r_{k,2} \leq O_2A \Rightarrow \quad r_{k,2}^2 \leq r_{g,2}^2 + \mathrm{AB}^2 \\ r_{k,1} \leq O_1B \Rightarrow \quad r_{k,1}^2 \leq r_{g,1}^2 + \mathrm{AB}^2 \end{cases} \ (5.24\text{-}5.25)$$

Consequently, having ensured geometric compatibility of the gears, a pair is chosen considering:

- The size, which is directly proportional to the shaft distance
- The preference for as many teeth as possible, because the convenience gear can achieve a larger transmission ratio due to the gear ratio

Before the choice is made, the strength of the gear is calculated. It is assumed that the material used is steel and the endurance of each pair is calculated under the AGMA criteria [44]. The values of stresses under bending and surface pressure are calculated.

Bending:

$$\sigma_b = \frac{P_u}{mbJ} K_o K_u K_s K_m K_B K_T K_R * \frac{FOS_{gear}}{K_L} \leq S_{bending} \ (5.26)$$

Table 5.6 - Bending AGMA coefficients

Coefficient Symbol	Coefficient name	Value	Comments
K_L	Coeff of life expectancy	1	No wear on the gears
K_T	Coeff. of Temperature	1	Pg. 795 [4]
K_R	Coef. Of Reliability	1.25	1 failure in 1000 pieces
K_O	Coeff. of Hyper charging	1	Smooth and slow working
K_u	Dynamic Coeff	1.1	Page 793, table 18.21 [4]
K_s	Size coefficient	Variable	m<5
K_B	Coeff of Rim	Variable	Page 794 table 18.22[4]
K_m	Coeff. of Load Distribution	Variable	$K_m = 1 + C_{pf} + C_{ma}$
C_{pf}	Coeff of Pinion Proportion	Variable	$b/10d_o - 0.0375 + 49212 * 10^{-4}b$
C_{ma}	Coeff of engagement alignment	Variable	$A + B * b + C * b^2$ σελ.794 [4]
J	Geometry Coefficient	0.35	Pg 795 [4]
FOS_{gear}	Factor of Safety	1.5	-

Where:

- $b = 10m$: width of the gears
- P_u: tangential force on the cogwheel

Surface Pressure:

$$\sigma_c = C_p\sqrt{\frac{P_u}{b*d0_1*I}K_oK_uK_sK_mC_f}\ K_TK_R * \frac{FOS}{Z_NC_H} \leq S_{sp} \quad (5.27)$$

$$C_p = \sqrt{\frac{1}{\pi\left[\frac{\left(1-v_p^2\right)}{E_p}+\frac{\left(1-v_g^2\right)}{E_g}\right]}} \quad (5.28)$$

Table 5.7 - Surface Pressure Coefficients

Coefficient Symbol	Coefficient Name	Value	Comment
$\boldsymbol{K_T}$	Temperature	1	Pg. 795 [4]
$\boldsymbol{K_R}$	Reliability	1.25	1 failure in 1000 pieces
$\boldsymbol{Z_N}$	Life expectancy	1	Very few cycles
$\boldsymbol{C_H}$	Wear resistance	1	Same hardness
$\boldsymbol{K_O}$	Hypercharging	1	Smooth and slow working
$\boldsymbol{K_u}$	Dynamic	1.1	Page 793, table 18.21 [4]
$\boldsymbol{K_s}$	Size	Variable	m<5
$\boldsymbol{K_m}$	Load distribution	Variable	$\boldsymbol{K_m = 1 + C_{pf} + C_{ma}}$
$\boldsymbol{C_{pf}}$	Pinion proportion	Variable	$\boldsymbol{b/10d_o - 0.0375 + 49212 * 10^{-4}b}$
$\boldsymbol{C_{ma}}$	Engagement alignment	Variable	$\boldsymbol{A + B * b + C * b^2}$ σελ.794 [4]
$\boldsymbol{C_f}$	Surface conditions against wear	1	Pg. 803 [4]

C_p	Material	185	Pg 803 [4] - Steel
$\mathbf{FOS_{sp}}$	FOS for surface pressure	$\mathbf{1.5}$	-
I	Geometrical	0.13	Pg. 808 [4]

Where:

- v_p: Poisson ratio for pinion
- v_g: Poisson ratio for gear
- E_p: Young modulus for pinion
- E_p: Young modulus for gear

The material of the gears is steel (**v=0.28,E=200 GPa**). Those values are close to the original ones. With all the information available, a conclusion for a pair of gears for the synchronization of the mechanism is reached. The characteristics of the pair are presented in Table 5.8.

	Characteristics
1 Z	40.0000
2 D	60.0000
3 Module	1.5000
4 Cs	0.4750
5 ContactRatio	1.7135
6 Transmission	1.0000
7 Bending	33.7400
8 Surface Pressure	343.0083
9 Shaft Distance	60.0000

Table 5.8 – Synchronizing gears characteristics

The convenience gear is tasked with lowering the required input torque. Since the module is already selected as part of the synchronizing gears analysis, the only variables to be calculated are the number of teeth and the gear strength. Since the convenience gear is the pinion, it will be subjected to bending and surface pressure. Similarly to the previous analysis, the stress applied on the root of the teeth for increasing number of teeth (from 18 to 30). The iterative process concludes to values for stresses and as a result the convenience gear characteristics are derived (Table 5.9). The gearing mechanism in its entirety is presented in Figure 5.20.

Table 5.9 - Convenience gear characteristics

	Characteristics
1 Z	25.0000
2 D	37.5000
3 Module	1.5000
4 Cs	0.4750
5 ContactRatio	1.6626
6 Transmission	0.6250
7 Bending	24.7282
8 Surface Pressure	166.4200
9 Shaft Distance	48.7500

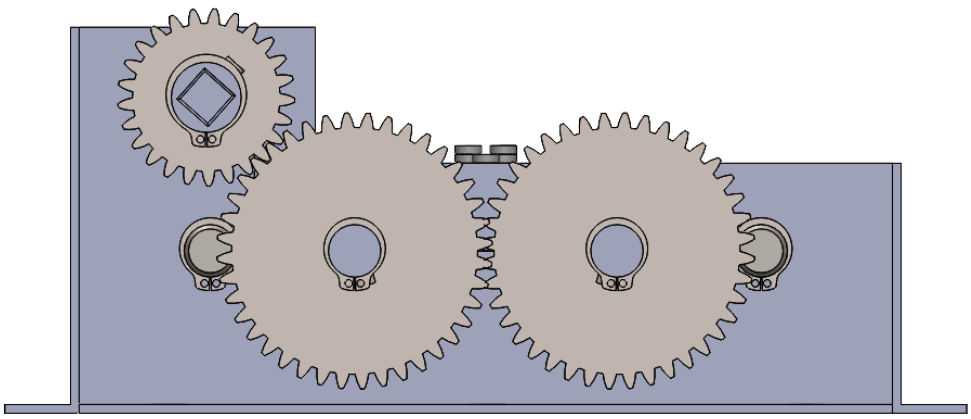

Figure 5.20 - Synchronizing gears and convenience gear configuration and meshing

5.2.2.5. Clamp

The last major part of the tension tool is the clamp. The clamp must have the required strength to withstand the tensile stress it applies on the SCP as well as the possibility for the plate to be detached from the tool and applied on the fracture, without obstructing the work of the surgeon. Additionally, since the clamp is at direct contact with the plate, it should be constructed from a material that is easy to sterilize.

The clamp mechanism should therefore be designed whilst receiving feedback from the form and working principle of the sustain tool. The final design of the clamp is presented in Figure 5.21.

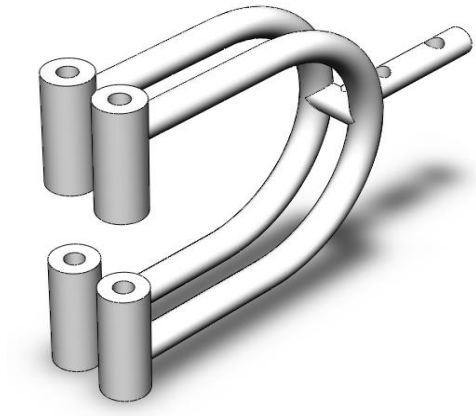

Figure 5.21 – Design for the clamp

The critical cross sections for this clamp are the ones in contact with the pins as well as the one in connection to the Sliding Element. The whole Clamp can be studied with bending and deflection of curved beams. The difference to normal beams is that the centroid axis is different to the neutral axis and therefore the problem is non – linear, however the stress can be calculated by considering the mentioned difference in the positions.

The formula for the stress caused due to bending is

$\sigma = \frac{M_y}{Ae(r_n \pm y)}$ (2.26) , where r_n: radius of neutral axis, e: distance from the centroidal axis to the neutral axis.

We can use the following equations 4to acquire the measures presented in the equation (2.26):

$$r_n = \frac{A}{\int \frac{dA}{r}} \ (2.27) - Neutral\ Axis\ Radius\ (from\ point\ of\ reference)$$

The clamp pins have circular cross sections, allowing for instant calculation of the centroidal axis. The results are as such:

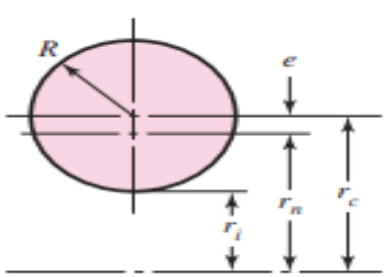

$$r_c = r_i + R$$

$$r_n = \frac{R^2}{2\left(r_c - \sqrt{r_c^2 - R^2}\right)}$$

Figure 5.22 - Curved Circular Cross Section Radius [58]

Taking these formulas into account, and applying the forces and moments applied on each end, the stress at the end of the clamp is calculated as **σ=250 MPa**.

Finally, a study of the deflection of the clamp due to the forces of the pin should be conducted. The clamp is always under tensile stress and therefore it cannot buckle. Using Castigliano's theorem (Equation 2.8), which is applied on the clamp for tension load [58], the deflection of the clamp is in a normal range.

5.2.2.6. Additional complementary elements

To conclude the study of the tool, the complementary keys, pins and screws are studied.

The keys are under shear stress when the power transfer from the gear to the shaft occurs. Keys are standardized by **DIN 950**. Normal keys are selected. The length of the key is selected to be **16mm**.

The bolts that are used to connect the housing to a table or a working bench aren't critically loaded by any of the components, therefore they don't have specific requirements. M12 screws, are sufficient.

The pins that are used to connect the clamp to the Sliding element as well as the pins of the clamp itself (used to preload the plate) are studied. Pins are subject to shear force. Pin strength is provided by the manufacturers; therefore, pins that fulfil the geometrical restrictions and can carry the load required to preload the plate (which is approximately 3KN) are selected. However, if manufacturers don't provide such a product, as the intended environment is unusual, a pin can be specially constructed for this application.

5.2.3. Design and Calculation of the sustain Tool

Having concluded the design of the tension tool, there is need for another device, the sustain tool for the preloaded SCP, to retain the tension applied on it. To achieve this without compromising the working principle of the tool, the design solution is the use of a second plate of a high strength steel that should not be elongated. The second plate has a shape similar to the SCP but scaled upwards. It will bear two holes on each side, in the position the preloaded plate will be elongated to. In this way, the two plates will be connected via pins and allow the combined plate body to detach from the clamps, for the surgeon to fix it on the patient under pretension. The second plate should not be much larger so as not to interfere with the bone or titanium casing of the SCP and should bear an opening along its length to allow for the SCP to be attached to the patient. The design of the sustain tool is presented in Figure 5.23.

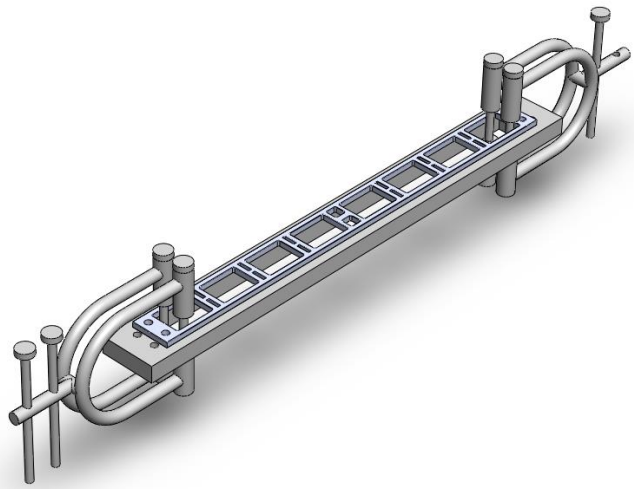

Figure 5.23 – Design for the sustain tool

With the conclusion of the sustain tool design, the comprehensive design of the tensioning tool with all additional components is presented in Figure 5.24.

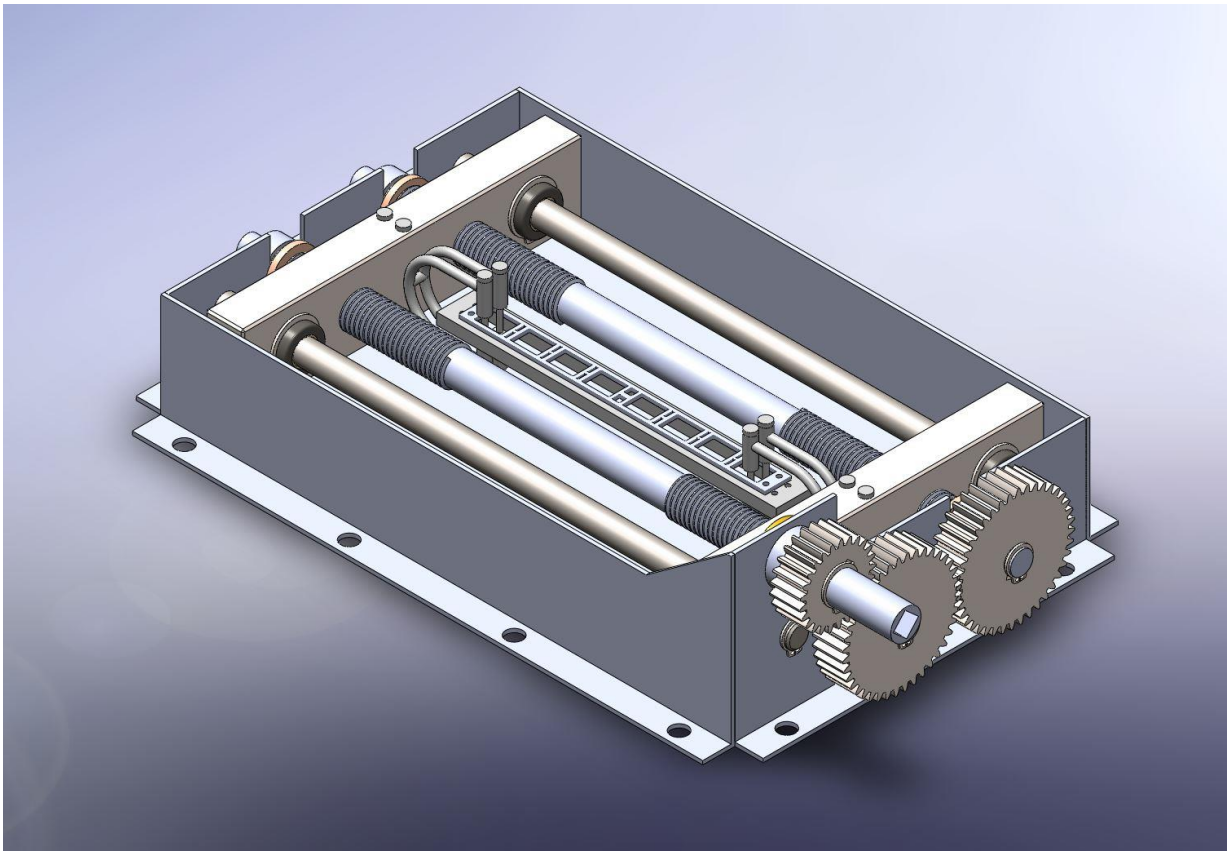

Figure 5.24 – Comprehensive design for the tensioning tool

5.3. Titanium case

The titanium case is composed of two parts. The bottom part (Figure 5.26) provides the platform for the SCP and sliding inserts to be placed and is compressed against the bone after fixing the screws and is responsible to maintain the rigidity of the structure under bending and torsional loads. Its thickness is **3.5mm** and contains slots for the sliding inserts to be inserted and guided. The slots allow the insert to slide inside them and restrict it when the maximum displacement is achieved. In this case the SCP and case have increasingly similar mechanical properties, since the SCP is in the more rigid austenitic phase. The slot length is designed at **13.5mm** to allow 3mm of displacement of the inserts in either side of the fracture, for a total of 6mm. The spacing of the slots is not uniform, since the outer slots of the SCP are displaced more compared to the innermost slots (Figure 5.25). To amend the differential, the slot spacing in the case increases progressively by 0.75mm each tim to account for the progressive displacement of each slot in the SCP and allow the inserts to be correctly positioned when they slide simultaneously.

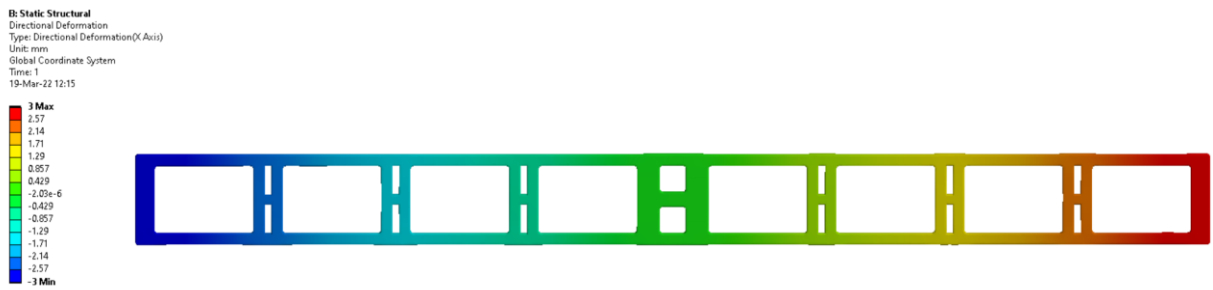

Figure 5.25 – Deformation contour for the SCP in the ANSYS Static Structural interface, showing the progressive displacement of each slot

The underside of the plate has a curvature radius of **40mm**, to approximately match the curvature of the bone and achieve a better fit.

The top part (Figure 5.27) provides additional rigidity and protects against pull-out of the screws, restricting the lateral movement of the inserts and screws. It contains matching slots for the sliding inserts, but with suitable tolerances, to ensure they do not interfere with the movement of the inserts. The thickness of the top part is maximized at **1.5mm**, as the total thickness of the case must not exceed **5mm** in order not to interfere with the surrounding soft tissues causing injury. Lastly, it is equipped with a long horizontal slot of **5mm** width which enables access to the screw heads and permits any adjustment without the need to remove the whole part.

The two parts of the case are connected with two custom **M2.5** screws on each end, with a thread length of **5mm**. The material of choice for the case is Titanium Grade 5 (Ti-6Al-4V), a popular choice for medical equipment. The complete design of the case is presented in the figures below.

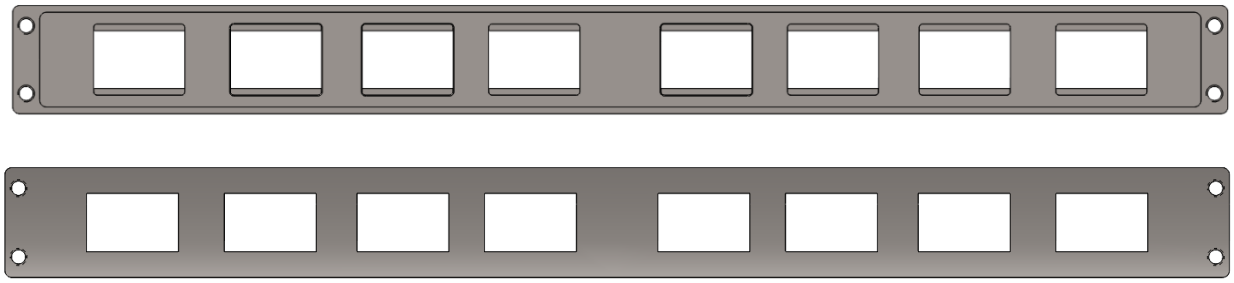

Figure 5.26 – Bottom part of the titanium case

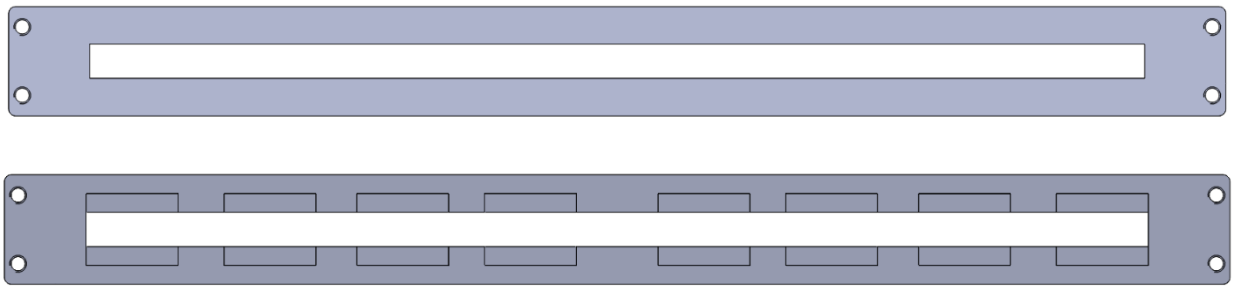

Figure 5.27 – Top part of the titanium case

With the conclusion of the titanium case design, the comprehensive design of the SCP with all additional components is presented in Figure 5.28.

The design drawings for all components and component assemblies are available in Appendix I.

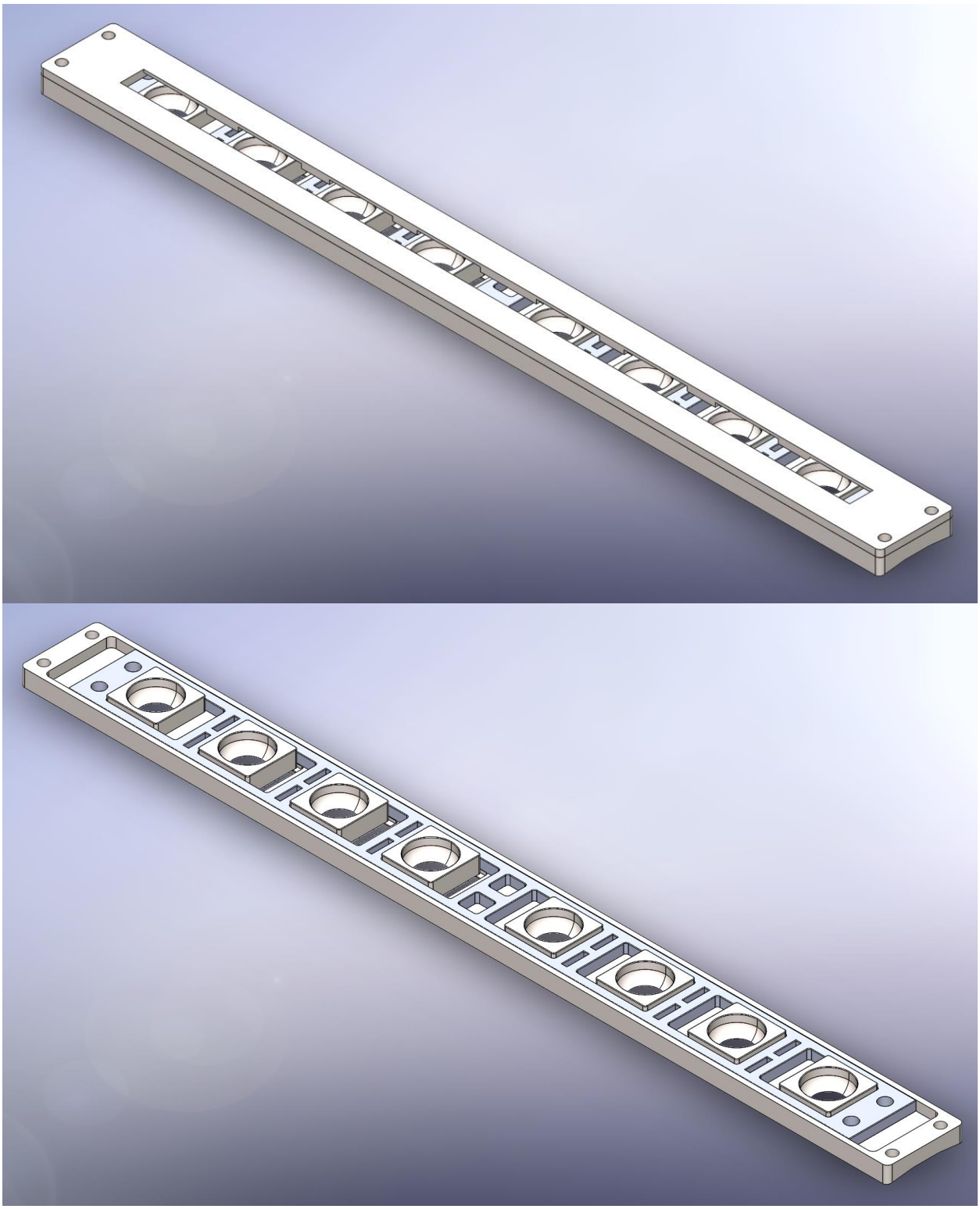

Figure 5.28 – Comprehensive design for the superelastic compression plate (SCP)

5.4. Surgical procedure description for SCP installation

The installation of the SCP in a clinical setting, requires a redesign of the normal surgical procedure followed for the DCP, due to the unique characteristics of the novel device. As a result, a description of the revised surgical procedure is required to accompany the device, in order for the medical professionals to assess it and familiarize themselves with it, before using it. The basic steps of the procedure are described as follows:

1. Performing the incision at the fracture site
2. Assessing the compression force needed, with respect to the fracture characteristics
3. Aligning the bone fragments with the appropriate device
4. Mounting the bottom part of the titanium case on the bone at the designated position
5. Drilling the screw holes at the correct positions, with the aid of a drill guide, designed for the rectangular slots
6. Placing the SCP on the tensioning tool and fixing the clamps with pins
7. Rotating the gear mechanism of the tensioning tool until the desired deformation is achieved
8. Unloading the SCP to work at the lower plateau or in any other stress level, if deemed necessary
9. Placing the pins of the sustain tool and remove the clamps
10. Lifting the SCP and sustain tool and rotate it, for the SCP to face the case
11. Placing the SCP inside the case slot without unloading
12. Inserting the sliding inserts in the SCP slots
13. Tightening the inserts on the case with cortical or other screws
14. Judging the contact and alignment situation at the fracture site
15. Removing the sustain tool to let the SCP unload
16. Screwing the top to the bottom part of the case
17. Examining the installation and performing suturing on the incision

The new process is expected to be of similar degree of difficulty to the existing one, but with a slightly longer duration due to the use of the tensioning tool. It is also logical to assume that the surgeons will need to follow training sessions before operating with the SCP, as is the case for every new medical device that deviates from the commonly practiced procedures.

6. Conclusion

This chapter concludes this study by summarizing the key findings in relation to the research aims and discussing their standing compared to relevant existing literature. The limitations of the study will be discussed and propositions for improvements and future research will be presented.

The aim of the study was to detail the design process and analyze the individual parameters of a novel long bone osteosynthesis device that addresses the problem of compression loss in traditional compression plating. Following the stages of the design process, consisting of research of past and current solutions, conceptual design and embodiment design, provided the necessary framework for the development of a final comprehensive design.

The literature review analyzed the progression of plating designs and techniques over the course of time and highlighted the advantages as well as the limitations of compression plating, while stressing the importance of understanding the fracture healing mechanism and the research areas of focus currently.

The finite element model of loading during walking for the DCP, calculated the maximum equivalent stress the plate is subjected to at 627 MPa and located on the inside of the screw slots near the fracture gap, indicating a potential critical design point. The findings are backed by several similar studies [41] - [43]. As far as the compression force is concerned, he minimum force value calculated at 810N is also comparable to the limited existing research [38].

In the conceptual design stage, the selection process concluded initially to three potential solutions, but a subsequent feasibility study and analysis in further detail qualified the current solution as the most promising. The superelastic properties of Nitinol particularly stood out, due to the hysteretic behavior in loading and unloading, which indicates the production of almost constant compression force in superelastic recovery from elongation [51], [54]. A concept of combining a thin superelastic Nitinol inner plate (SCP) for compression adjustment with a titanium outer case for strength and rigidity was created. The plate is inserted into the case under tension and let to rebound to compress the fracture gap.

In the embodiment design stage, the selected concept was tested with a combination of finite element models and experiments. The finite element model produced results indicating the SCP can be designed to achieve deformations of up to 6mm and sustained compressive force of around 800N, without exceeding 6% strain. Tension and bending stress tests produced results of ultimate tensile strength at 769 MPa and bending strength of 428 MPa, confirming the material model and findings of earlier studies [54]. Consequently, another experiment was designed, to measure the compression force of the DCP at the fracture site with a load cell. The result was a maximum force of 38.24Kgf or 375.13N. Using the calculated data, the design parameters for the SCP, two-part titanium case and sliding screw inserts were specified, thus finalizing the design of the device. The surgical procedure for installation of the device was also described.

Finally, a design process was executed for the tensioning tool required to tension the SCP and sustain it during the installation surgical procedure. Detailed calculations were performed for each component of the tool, to produce a final design.

In retrospect, the findings of the study are encouraging, as far as the working principle of the design is concerned. Both computational models and experiments point to the potential of superelasticity in compression plate osteosynthesis. The adjustment mechanism is completely non-invasive and is projected to improve the compression loss problem.

Naturally, the study also has specific limitations, mainly due to lack of resources for designing accurate experimental configurations and performing multiple series of tests. The deficiencies signalized, are planned to be improved upon in future iterations.

Particularly, the experimental testing performed cannot be considered sufficient. For both tension and bending experiments, cutting imperfections in the test specimens have likely resulted in underestimation of stress and load values. Additionally, the lack of a strain gauge in the tension experiment and the conversion of load to stress measurement in the bending experiment presented the need for corrective action through computational and theoretical models that are certain to introduce some level of error. An iteration of the experiment with more precise specimens and measuring equipment should be performed to extract reliable results.

Moreover, in the compression force experiment, the use of only four screws on a low quality bone model suggest that the results can only serve as a rough indication of the force range. An improved iteration of the experiment is planned, where the plate is applied on a bovine femur and is installed by a trained surgeon using all available screw positions. The improved surgical technique and natural bone tissue are predicted to greatly increase the force measurements and approach the known estimates.

Finally, some critical points of the design such as the friction between the case and the sliding inserts and the rigidity achieved by the multi-part device have not been addressed as of yet. A similar process to the analysis already performed is planned to be conducted, with the construction of computational models and experimental validation.

With the conclusion of the study, the hope that its findings can inspire further research in the applications of superelasticity in compression osteosynthesis and in experimental quantification of osteosynthesis parameters, is expressed. The design proposed is by no means final and conclusive, as improvement potential is apparent in several areas. The goals of the planned design steps, are the execution of a proof of concept experiment and the construction of a prototype of the SCP, the placement of a load cell on the tensioning tool to be able to monitor force values with precision and ultimately streamlining the surgical procedure, reducing the dependence on surgeon experience and skill for achieving optimal results.

Table of figures

Figure 2.1 - Bagby and Janes' compression plate [2] 16

Figure 2.2 - DCP holes form and function [4] 17

Figure 2.3 - Comparison of footprints in DCP and LC-DCP [4] 18

Figure 2.4 - Combination holes in the locking compression plate (LCP) [4] 19

Figure 3.1 – Anatomical planes and axes of the human body 23

Figure 3.2 - Femur model with holes in the ANSYS Spaceclaim interface 26

Figure 3.3 - 10-hole narrow DCP model 27

Figure 3.4 – Gait cycle phases and terms [32] 29

Figure 3.5 – Pelvic and thigh muscles of the human body [37] 29

Figure 3.6 – Femur and DCP model with reference coordinate system in the ANSYS Workbench interface 31

Figure 3.7 – Loading conditions for the femur and DCP model in the ANSYS Static Structural interface 32

Figure 3.8 – Detail of the mesh for the femur and DCP model in the ANSYS Static Structural interface 33

Figure 3.9 - Maximum equivalent von Mises stress contour on the DCP in the ANSYS Static Structural interface 34

Figure 3.10 – Loading conditions and stress contours for the Zhang et al. humerus and plate model [41] 35

Figure 3.11 – Loading conditions and stress contours for the Antoniac et al. humerus and plate model [42] 35

Figure 3.12 – Loading conditions and stress contours for the Zhou et al. femur and plate model [43] 36

Figure 4.1 – Rack-pinion sketch 41

Figure 4.2 – Weight-based ratchet sketch 41

Figure 4.3 – Weight-based permanent deformation spring sketch 41

Figure 4.4 – Magnetic screw tightening sketch 42

Figure 4.5 – Shape memory screw shaft sketch 43

Figure 4.6 – Screw-less shape memory scaffold sketch 44

Figure 4.7 – Screw-less bone sleeve sketch 44

Figure 4.8 – Shape memory screw connector sketch 44

Figure 4.9 – Split plate sketch 45

Figure 4.10 – Forces on a square thread and nut pair [44] 47

Figure 4.11 – Stiffness-temperature graph for shape memory polymers [49] 50

Figure 4.12 – Stress-strain curves for shape memory alloys exhibiting shape memory effect and superelasticity [52] 51

Figure 4.13 – Partial phase diagram of Ni-Ti [53] 51

Figure 4.14 – Superelastic nitinol stress-strain hysteresis loops comparison between experimental data and an improved Graesser and Cozzarelli theoretical model 53

Figure 4.15 – Advanced concept for the screw connector, using a titanium case and a superelastic inner plate 54

Figure 5.1 – Four screw slot configurations for the SCP 56

Figure 5.2 - Loading conditions for the femur and DCP model in the ANSYS Static Structural interface 56

Figure 5.3 – Location of force measurements on the stress-strain hysteresis loop of superelastic nitinol 57

Figure 5.4 - Maximum equivalent von Mises stress and equivalent strain contours for the 6 oval slots SCP configuration in the ANSYS Static Structural interface 58

Figure 5.5 - Maximum equivalent von Mises stress and equivalent strain contours for the 6 rectangular slots SCP configuration in the ANSYS Static Structural interface 58

Figure 5.6 - Maximum equivalent von Mises stress and equivalent strain contours for the 8 oval slots SCP configuration in the ANSYS Static Structural interface 58

Figure 5.7 - Maximum equivalent von Mises stress and equivalent strain contours for the 8 rectangular slots SCP configuration in the ANSYS Static Structural interface 59

Figure 5.8 - Loading conditions for the tension test specimen model in the ANSYS Static Structural interface 62

Figure 5.9 – Experimental tension stress-strain curve for superelastic Nitinol with corrected strain values 63

Figure 5.10 - Experimental bending stress-strain curve for superelastic Nitinol with corrected stress values 64

Figure 5.11 – Wheatstone bridge resistors configuration used in load cells [56] 67

Figure 5.12 – Sliding insert design 69

Figure 5.13 – Superelastic compression plate (SCP) design 70

Figure 5.14 – Concept for the tension tool..... 71

Figure 5.15: NQM Diagrams of the Sliding Element in the OptimalBeam interface 74

Figure 5.16 - NQM Diagrams of the Statically Indeterminate Element..... 76

Figure 5.17 - Tension mechanism with clamp attached..... 77

Figure 5.18 - Force – ratchet length diagram 79

Figure 5.19 - Oilless self-lubricating bronze-graphite bushing 79

Figure 5.20 - Synchronizing gears and convenience gear configuration and meshing..... 86

Figure 5.21 – Design for the clamp 87

Figure 5.22 - Curved Circular Cross Section Radius [58]..... 87

Figure 5.23 – Design for the sustain tool 89

Figure 5.24 – Comprehensive design for the tensioning tool..... 89

Figure 5.25 – Deformation contour for the SCP in the ANSYS Static Structural interface, showing the progressive displacement of each slot 90

Figure 5.26 – Bottom part of the titanium case 91

Figure 5.27 – Top part of the titanium case 91

Figure 5.28 – Comprehensive design for the superelastic compression plate (SCP) 92

List of tables

Table 3.1 – Material properties of cortical bone tissue in the ANSYS Workbench interface ... 27

Table 3.2 - Material properties of Grade 5 Titanium alloy (Ti-6Al-4V) in the ANSYS Workbench interface ... 28

Table 3.3 – Force components acting on the femur model ... 30

Table 3.4 – Contact areas and types for the femur and DCP model ... 32

Table 3.5 – Analysis settings for the femur and DCP model in the ANSYS Static Structural interface ... 33

Table 4.1 – Final evaluation scores of alternative solutions in descending order of highest score ... 46

Table 4.2 – Parameters for 3.5mm and 4.5mm cortical screws (ISO 5835:1991) ... 48

Table 4.3 - Screwing force and torque values for 3.5mm and 4.5mm cortical screws ... 49

Table 5.1 - Material properties of superelastic Nitinol in the ANSYS Workbench interface ... 57

Table 5.2 – Values of maximum stress, maximum strain, maximum force and lower plateau force of the four screw slots configurations for the SCP ... 59

Table 5.3 – Compression force measurements from the load cell for the DCP with one or two screw pairs fixed ... 68

Table 5.4 – Sliding element dimensions ... 76

Table 5.5 – Bushing dimensions ... 80

Table 5.6 - Bending AGMA coefficients ... 83

Table 5.7 - Surface Pressure Coefficients ... 84

Table 5.8 – Synchronizing gears characteristics ... 85

Table 5.9 - Convenience gear characteristics ... 86

List of images

Image 2.1 – Hansmann's plate set [4] **14**

Image 2.2 – Lane's plate design [2] **14**

Image 2.3 – Lambotte's plate design [2] **14**

Image 2.4 – Danis' "coapteur" plate, the first compression plate [2] **15**

Image 2.5 – Modern dynamic compression plate (DCP) [21] **17**

Image 3.1 – The interface of the 3D Slicer software **23**

Image 3.2 – Bone tissue thresholding in the 3D Slicer interface **24**

Image 3.3 – The interface of the Meshmixer software **25**

Image 3.4 – Comparison of the initial and the smooth femur model **25**

Image 5.1 – Test specimens for tensile test (left), loading-unloading test (middle) and bending test (right) **60**

Image 5.2 – INSTRON 4482 testing machine with tension test specimen clamped **61**

Image 5.3 - INSTRON 4482 testing machine with compression test specimen placed **61**

Image 5.4 – Brittle fracture of Nitinol **64**

Image 5.5 – Split PLA femur model, 10-hole wide DCP and two 4.5mm cortical screws **65**

Image 5.6 (left) – Placement of the DCP on the 3D printed femur model **65**

Image 5.7 (right) – Use of a drill guide for positioning of the holes **65**

Image 5.8 – Cutting of an aluminum cup from a rod using a lathe machine **66**

Image 5.9 (left) – Aluminum cup inside a slot in the 3D printed bone fragment **66**

Image 5.10 (right) – Placement of a button type load cell inside the aluminum cup in the 3D printed bone fragment **66**

Image 5.11 – Load cell, ADC and Arduino microcontroller configuration **67**

Image 5.12 – DCP mounted on the 3D printed femur fragments with two screw pairs **68**

List of references

[1] R. Lakatos, M. Herbenick, F. Talavera, and S. Agnew, “General Principles of Internal Fixation,” *Medscape*, Aug. 25, 2021. https://emedicine.medscape.com/article/1269987

[2] H. K. Uhthoff, P. Poitras, and D. S. Backman, “Internal plate fixation of fractures: short history and recent developments,” *Journal of Orthopaedic Science*, vol. 11, no. 2, pp. 118–126, Mar. 2006, doi: 10.1007/s00776-005-0984-7.

[3] P. Augat and C. von Rüden, “Evolution of fracture treatment with bone plates,” *Injury*, vol. 49, pp. S2–S7, Jun. 2018, doi: 10.1016/S0020-1383(18)30294-8.

[4] C. Colton and J. Orson, “Plates–Form and function,” AO Foundation/AO Trauma, Study Guide.

[5] J. Hunter, in *The Works of John Hunter, With Notes, Ed. By J.f.Palmer*, 4 vols., London: Longman Rees, 1837.

[6] J. Belchier, “II. A further account of the bones of animals being made red by aliment only,” *Phil. Trans. R. Soc.*, vol. 39, no. 443, pp. 299–300, Dec. 1735, doi: 10.1098/rstl.1735.0065.

[7] L. Marzona and B. Pavolini, “Play and players in bone fracture healing match,” *Clinical Cases in Mineral and Bone Metabolism*, vol. 6, no. 2, pp. 159–162, 2009.

[8] J. M. Kanczler and R. O. C. Oreffo, “Osteogenesis and angiogenesis: the potential for engineering bone,” *Eur Cell Mater*, vol. 15, pp. 100–114, May 2008, doi: 10.22203/ecm.v015a08.

[9] R. Bielby, E. Jones, and D. McGonagle, “The role of mesenchymal stem cells in maintenance and repair of bone,” *Injury*, vol. 38 Suppl 1, pp. S26-32, Mar. 2007, doi: 10.1016/j.injury.2007.02.007.

[10] F. N. K. Kwong and M. B. Harris, “Recent developments in the biology of fracture repair,” *J Am Acad Orthop Surg*, vol. 16, no. 11, pp. 619–625, Nov. 2008, doi: 10.5435/00124635-200811000-00001.

[11] R. Danis and Universit?? libre de Bruxelles (1834-1970), *Theorie et pratique de l’osteosynthese: par Robert Danis ...* Paris: Masson (Niort, impr. de Soulisse-Martin), 1949.

[12] C. Hansmann, “Eine neue Methode der Fixierung der Fragmente bei komplizierten Frakturen.,” *Verhandlungen der Deutschen Gesellschaft für Chirurgie*, no. 15, pp. 134–37, 1886.

[13] W. A. Lane, “Clinical Remarks ON THE OPERATIVE TREATMENT OF FRACTURES,” *Br Med J*, vol. 1, no. 2418, pp. 1037–1038, May 1907.

[14] A. Lambotte, “Technique et indication des prothèses dans le traitement des fractures,” *Presse Med*, no. 17, p. 321, 1909.

[15] W. O. Sherman, “Vanadium steel bone plates and screws,” *Surg Gynecol Obstet*, no. 14, pp. 629–34, 1912.

[16] J. Bartoníček, “Early history of operative treatment of fractures,” *Arch Orthop Trauma Surg*, vol. 130, no. 11, pp. 1385–1396, Nov. 2010, doi: 10.1007/s00402-010-1082-7.

[17] G. W. N. Eggers, “Internal contact splint,” *J Bone Joint Surg Am*, vol. 30A, no. 1, pp. 40–52, Jan. 1948.

[18] G. W. Bagby and J. M. Janes, “The effect of compression on the rate of fracture healing using a special plate,” *Am J Surg*, vol. 95, no. 5, pp. 761–771, May 1958, doi: 10.1016/0002-9610(58)90625-1.

[19] M. E. Mueller, M. Allgoewer, and H. Willenegger, “Compression fixation with plates,” in *echnique of internal fixation of fractures*, Berlin: Springer, 1965, pp. 47–51.

[20] R. Schenk and H. Willenegger, “Morphological findings in primary fracture healing,” in *Krompecher S, Kerner E, editors. Callus formation symposium on the biology of fracture healing.*, Budapest: Akadémiai Kiadó, 1967, pp. 75–86.

[21] “Titanium 3.5 mm Small DCP Plate, Relife Ortho | ID: 4108702791.” https://www.indiamart.com/proddetail/3-5-mm-small-dcp-plate-4108702791.html (accessed Mar. 17, 2022).

[22] S. M. Perren, K. Klaue, O. Pohler, M. Predieri, S. Steinemann, and E. Gautier, “The limited contact dynamic compression plate (LC-DCP),” *Arch Orthop Trauma Surg*, vol. 109, no. 6, pp. 304–310, 1990, doi: 10.1007/BF00636166.

[23] H. K. Uhthoff, D. Boisvert, and M. Finnegan, “Cortical porosis under plates. Reaction to unloading or to necrosis?,” *J Bone Joint Surg Am*, vol. 76, no. 10, pp. 1507–1512, Oct. 1994, doi: 10.2106/00004623-199410000-00010.

[24] H. K. Uhthoff and Z. F. Jaworski, “Bone loss in response to long-term immobilisation,” *J Bone Joint Surg Br*, vol. 60-B, no. 3, pp. 420–429, Aug. 1978, doi: 10.1302/0301-620X.60B3.681422.

[25] R. Jain, N. Podworny, T. M. Hupel, J. Weinberg, and E. H. Schemitsch, “Influence of plate design on cortical bone perfusion and fracture healing in canine segmental tibial fractures,” *J Orthop Trauma*, vol. 13, no. 3, pp. 178–186, Apr. 1999, doi: 10.1097/00005131-199903000-00005.

[26] A. Gerber and R. Ganz, “Combined internal and external osteosynthesis a biological approach to the treatment of complex fractures of the proximal tibia,” *Injury*, vol. 29, pp. 22–28, Dec. 1998, doi: 10.1016/S0020-1383(98)95005-7.

[27] S. Tepic and S. M. Perren, “The biomechanics of the PC-Fix internal fixator,” *Injury*, vol. 26, pp. B5–B10, Jan. 1995, doi: 10.1016/0020-1383(95)96892-8.

[28] S. M. Perren, “EVOLUTION OF THE INTERNAL FIXATION OF LONG BONE FRACTURES,” *THE JOURNAL OF BONE AND JOINT SURGERY*, vol. 84, no. 8, p. 18, 2002.

[29] A. Padolino *et al.*, “Comparison of CFR-PEEK and conventional titanium locking plates for proximal humeral fractures: a retrospective controlled study of patient outcomes,” *Musculoskelet Surg*, vol. 102, no. S1, pp. 49–56, Oct. 2018, doi: 10.1007/s12306-018-0562-8.

[30] “Image Segmentation | Types Of Image Segmentation.” https://www.analyticsvidhya.com/blog/2019/04/introduction-image-segmentation-techniques-python/ (accessed Mar. 17, 2022).

[31] E. F. Morgan, G. U. Unnikrisnan, and A. I. Hussein, “Bone Mechanical Properties in Healthy and Diseased States,” *Annu. Rev. Biomed. Eng.*, vol. 20, no. 1, pp. 119–143, Jun. 2018, doi: 10.1146/annurev-bioeng-062117-121139.

[32] M. Karadsheh, “Gait Cycle - Foot & Ankle,” *Orthobullets*, Aug. 13, 2021. https://www.orthobullets.com/foot-and-ankle/7001/gait-cycle (accessed Mar. 17, 2022).

[33] J. A. Simoes, M. A. Vaz, S. Blatcher, and M. Taylor, “Influence of head constraint and muscle forces on the strain distribution within the intact femur,” *Medical Engineering*, p. 7, 2000.

[34] J. Skubich and S. Piszczatowski, “Model of loadings acting on the femoral bone during gait,” *Journal of Biomechanics*, vol. 87, pp. 54–63, Apr. 2019, doi: 10.1016/j.jbiomech.2019.02.018.

[35] T. San Antonio, M. Ciaccia, C. Müller-Karger, and E. Casanova, “Orientation of orthotropic material properties in a femur FE model: A method based on the principal stresses directions,” *Medical Engineering & Physics*, vol. 34, no. 7, pp. 914–919, Sep. 2012, doi: 10.1016/j.medengphy.2011.10.008.

[36] G. Bergmann, A. Bender, J. Dymke, G. Duda, and P. Damm, “Standardized Loads Acting in Hip Implants,” *PLoS ONE*, vol. 11, no. 5, p. e0155612, May 2016, doi: 10.1371/journal.pone.0155612.

[37] M. Björnsdóttir, “Influence of Muscle Forces on Stresses in the Human Femur,” KTH, Stockholm, 2014.

[38] S. M. Perren, A. Huggler, M. Russenberger, F. Straumann, M. E. Mueller, and M. Allgoewer, “A Method of Measuring the Change in Compression Applied to Living Cortical Bone,” *Acta Orthopaedica Scandinavica*, vol. 40, no. 125, pp. 1–63, 1969, doi: 10.3109/ort.1969.40.suppl-125.01.

[39] C. Voutat, J. Nohava, J. Wandel, and P. Zysset, “The Dynamic Friction Coefficient of the Wet Bone-Implant Interface: Influence of Load, Speed, Material and Surface Finish,” *Biotribology*, vol. 17, pp. 64–74, Mar. 2019, doi: 10.1016/j.biotri.2019.03.002.

[40] Y. Zhang, P. B. Ahn, D. C. Fitzpatrick, A. D. Heiner, R. A. Poggie, and T. D. Brown, “Interfacial frictional behavior: cancellous bone, cortical bone, and a novel porous tantalum biomaterial,” *J. Musculoskelet. Res.*, vol. 03, no. 04, pp. 245–251, Dec. 1999, doi: 10.1142/S0218957799000269.

[41] T. Zhang, N. M. Harrison, P. F. McDonnell, P. E. McHugh, and S. B. Leen, “A finite element methodology for wear–fatigue analysis for modular hip implants,” *Tribology International*, vol. 65, pp. 113–127, Sep. 2013, doi: 10.1016/j.triboint.2013.02.016.

[42] I. Antoniac *et al.*, “Failure Analysis of a Humeral Shaft Locking Compression Plate—Surface Investigation and Simulation by Finite Element Method,” *Materials*, vol. 12, no. 7, p. 1128, Apr. 2019, doi: 10.3390/ma12071128.

[43] J.-J. Zhou, M. Zhao, D. Liu, H.-Y. Liu, and C.-F. Du, “Biomechanical Property of a Newly Designed Assembly Locking Compression Plate: Three-Dimensional Finite Element Analysis,” *Journal of Healthcare Engineering*, vol. 2017, pp. 1–10, 2017, doi: 10.1155/2017/8590251.

[44] C. Papadopoulos, *Machine Elements*, 3rd ed. Patras: Tziola Publications, 2017.

[45] W. Rottiers, L. Van den Broeck, C. Peeters, and P. Arras, “Shape Memory Materials and their applications,” p. 12.

[46] W. M. Huang, Z. Ding, C. C. Wang, J. Wei, Y. Zhao, and H. Purnawali, “Shape memory materials,” *Materials Today*, vol. 13, no. 7–8, pp. 54–61, Jul. 2010, doi: 10.1016/S1369-7021(10)70128-0.

[47] R. Sarvari *et al.*, “Shape-memory materials and their clinical applications,” *International Journal of Polymeric Materials and Polymeric Biomaterials*, pp. 1–21, Oct. 2020, doi: 10.1080/00914037.2020.1833010.

[48] F. Pilate, A. Toncheva, P. Dubois, and J.-M. Raquez, “Shape-memory polymers for multiple applications in the materials world,” *European Polymer Journal*, vol. 80, pp. 268–294, Jul. 2016, doi: 10.1016/j.eurpolymj.2016.05.004.

[49] R. Gopal, “Glass Transition Temperature (Tg),” *Corrosionpedia*, Mar. 15, 2021. https://www.corrosionpedia.com/definition/593/glass-transition-temperature-tg (accessed Mar. 19, 2022).

[50] C. W. Müller *et al.*, “A Novel Shape Memory Plate Osteosynthesis for Noninvasive Modulation of Fixation Stiffness in a Rabbit Tibia Osteotomy Model,” *BioMed Research International*, vol. 2015, pp. 1–8, 2015, doi: 10.1155/2015/652940.

[51] A. Wadood, “Brief Overview on Nitinol as Biomaterial,” *Advances in Materials Science and Engineering*, vol. 2016, pp. 1–9, 2016, doi: 10.1155/2016/4173138.

[52] J. W. Mwangi, H. Zeidler, R. Kühn, and A. Schubert, “Suitability assessment of micro-EDM in machining Nitinol for medical applications,” May 2016.

[53] C. M. Wayman and K. Otsuka, *Shape memory materials*. Cambridge: Cambridge University Press, 1999.

[54] H. Qian, H. Li, G. Song, and W. Guo, “Recentering Shape Memory Alloy Passive Damper for Structural Vibration Control,” *Mathematical Problems in Engineering*, vol. 2013, p. e963530, Nov. 2013, doi: 10.1155/2013/963530.

[55] E. J. Graesser and F. A. Cozzarelli, “Shape-Memory Alloys as New Materials for Aseismic Isolation,” *Journal of Engineering Mechanics*, vol. 117, no. 11, pp. 2590–2608, Nov. 1991, doi: 10.1061/(ASCE)0733-9399(1991)117:11(2590).

[56] “What is a wheatstone bridge and other strain gauges circuits.” https://www.omega.co.uk/literature/transactions/volume3/strain2.html (accessed Mar. 19, 2022).

[57] Th. N. Kostopoulos, *Gearing and Speed Reducers*. Athens: Symeon Publications, 2010.

[58] R. G. Budynas, J. K. Nisbett, and J. E. Shigley, *Shigley’s mechanical engineering design*. New York: McGraw-Hill, 2011.

[59] Y.-K. Zhang, H.-W. Wei, K.-P. Lin, W.-C. Chen, C.-L. Tsai, and K.-J. Lin, “Biomechanical effect of the configuration of screw hole style on locking plate fixation in proximal humerus fracture with a simulated gap: A finite element analysis,” *Injury*, vol. 47, no. 6, pp. 1191–1195, Jun. 2016, doi: 10.1016/j.injury.2016.02.028.

Appendix I – Design drawings

Appendix II – Alternative solutions table with scores

Evaluation 1

Group	1 (Bone healing facilitation)			2 (Adjustment potential)			
Variant	a (Blood supply)	b (Alignment & contact)	c (Micromovements)	a (Range)	b (Axial force control)	c (Mistake correction)	d (Non-adjustment)
Weight	0.08	0.08	0.01	0.02	0.065	0.065	0.06
1	3	3	4	5	2	4	5
2a	3	3	2	5	1	1	1
2b	3	3	3	3	3	1	1
3	4	4	2	3	5	5	5
4a	4	4	3	3	4	3	3
4b	4	4	5	4	3	2	2
5a	4	4	5	2	3	2	2
5b	4	4	5	2	3	2	2
6a	5	5	2	4	4	4	5
6b	1	5	2	3	5	4	5
7	3	4	3	4	5	3	2
8	3	3	5	2	3	3	3

Group	3 (Application difficulty)								
Variant	a (Control equipment)	b (Manufacturing)	c (Storage)	d (Dimensions)	e (Invasion)	f (Improvement on current)	g (Removal)	h (Surgeon training)	i (Post-op)
Weight	0.02	0.015	0.005	0.04	0.06	0.04	0.015	0.005	0.02
1	2	3	5	3	4	2	1	4	4
2a	5	4	5	3	5	1	1	4	3
2b	5	3	5	3	5	3	1	4	3
3	2	3	3	4	5	4	2	5	4
4a	3	2	2	4	4	5	3	4	5
4b	3	2	3	4	4	5	3	4	5
5a	3	3	3	4	5	5	3	3	5
5b	3	3	3	4	5	5	3	3	5
6a	3	2	2	5	4	5	4	3	5
6b	3	4	4	5	2	2	1	3	5
7	4	3	4	3	4	3	4	5	5
8	4	2	5	3	4	4	4	5	5

Group	4 (Robustness and reliability)						
Variant	a (Strength)	b (Post-op complications)	c (Versatility)	d (Adjusting mechanism)	e (Biocompatibility)	f (Environment)	g (Failure consequences)
Weight	0.06	0.015	0.015	0.04	0.01	0.06	0.05
1	1	3	3	3	5	4	1
2a	1	2	2	2	5	2	1
2b	2	2	2	2	5	2	1
3	5	5	5	4	4	4	4
4a	3	3	5	3	4	4	3
4b	4	4	5	3	5	4	3
5a	5	4	5	3	5	4	3
5b	5	4	5	3	5	4	3
6a	3	4	5	4	4	4	3
6b	5	2	5	5	2	5	2
7	5	4	5	2	5	4	5
8	2	4	3	2	4	4	3

Group	5 (Cost)				Total
Variant	a (Materials)	b (Manufacturing)	c (Post-op)	d (Training)	
Weight	0.06	0.06	0.02	0.01	
1	3	2	3	4	2.99
2a	5	4	5	4	2.63
2b	4	4	5	4	2.80
3	3	4	3	5	4.15
4a	1	4	4	5	3.51
4b	2	4	4	5	3.51
5a	2	3	4	3	3.52
5b	2	3	4	3	3.52
6a	1	1	3	3	3.75
6b	3	3	5	3	3.63
7	3	3	5	5	3.69
8	4	3	5	5	3.29

Evaluation 2

Group	1 (Bone healing facilitation)			2 (Adjustment potential)			
Variant	a (Blood supply)	b (Alignment & contact)	c (Micromovements)	a (Range)	b (Axial force control)	c (Mistake correction)	d (Non-adjustment)
Weight	0.08	0.08	0.01	0.02	0.065	0.065	0.06
1	2	2	4	5	2	4	5
2a	2	2	3	3	1	0	1
2b	2	2	3	3	3	1	1
3	4	3	5	3	5	5	5
4a	3	3	5	3	4	3	3
4b	3	3	4	2	3	2	3
5a	4	3	4	2	3	2	3
5b	4	3	4	2	3	2	3
6a	4	5	4	4	5	3	5
6b	1	5	3	3	4	5	5
7	4	3	5	4	4	2	2
8	2	3	5	2	4	2	3

Group	3 (Application difficulty)								
Variant	a (Control equipment)	b (Manufacturing)	c (Storage)	d (Dimensions)	e (Invasion)	f (Improvement on current)	g (Removal)	h (Surgeon training)	i (Post-op)
Weight	0.02	0.015	0.005	0.04	0.06	0.04	0.015	0.005	0.02
1	2	3	5	2	4	2	1	4	5
2a	5	3	5	2	4	1	1	4	3
2b	5	4	5	2	4	3	1	4	3
3	2	3	3	4	5	4	3	5	5
4a	3	2	2	3	4	5	3	4	4
4b	3	1	3	4	3	5	3	4	4
5a	3	2	3	4	4	5	3	3	4
5b	3	1	3	4	3	5	3	3	4
6a	3	1	2	2	1	5	4	3	4
6b	3	4	4	1	1	2	1	3	5
7	3	2	4	3	3	4	3	4	4
8	3	2	5	3	3	4	3	5	4

Group	4 (Robustness and reliability)						
Variant	a (Strength)	b (Post-op complications)	c (Versatility)	d (Adjusting mechanism)	e (Biocompatibility)	f (Environment)	g (Failure consequences)
Weight	0.06	0.015	0.015	0.04	0.01	0.06	0.05
1	1	3	3	3	4	4	1
2a	1	2	1	2	5	2	1
2b	2	2	1	2	5	2	1
3	4	4	5	4	4	4	5
4a	3	3	5	3	4	4	3
4b	4	4	5	2	5	4	3
5a	4	4	5	2	5	4	3
5b	4	4	5	2	5	4	3
6a	3	4	5	3	4	4	3
6b	5	2	5	4	2	5	2
7	4	4	5	2	5	4	3
8	2	4	3	2	4	4	3

Group	5 (Cost)				Total
Variant	a (Materials)	b (Manufacturing)	c (Post-op)	d (Training)	
Weight	0.06	0.06	0.02	0.01	
1	3	2	3	4	2.80
2a	5	3	5	4	2.19
2b	4	4	5	4	2.54
3	3	3	3	5	4.05
4a	1	3	4	5	3.25
4b	2	3	3	5	3.15
5a	2	3	3	3	3.28
5b	2	3	3	3	3.20
6a	1	1	3	3	3.32
6b	1	3	5	3	3.26
7	3	3	3	5	3.28
8	3	3	3	5	2.99

Appendix III – Compression load cell specifications and program codes

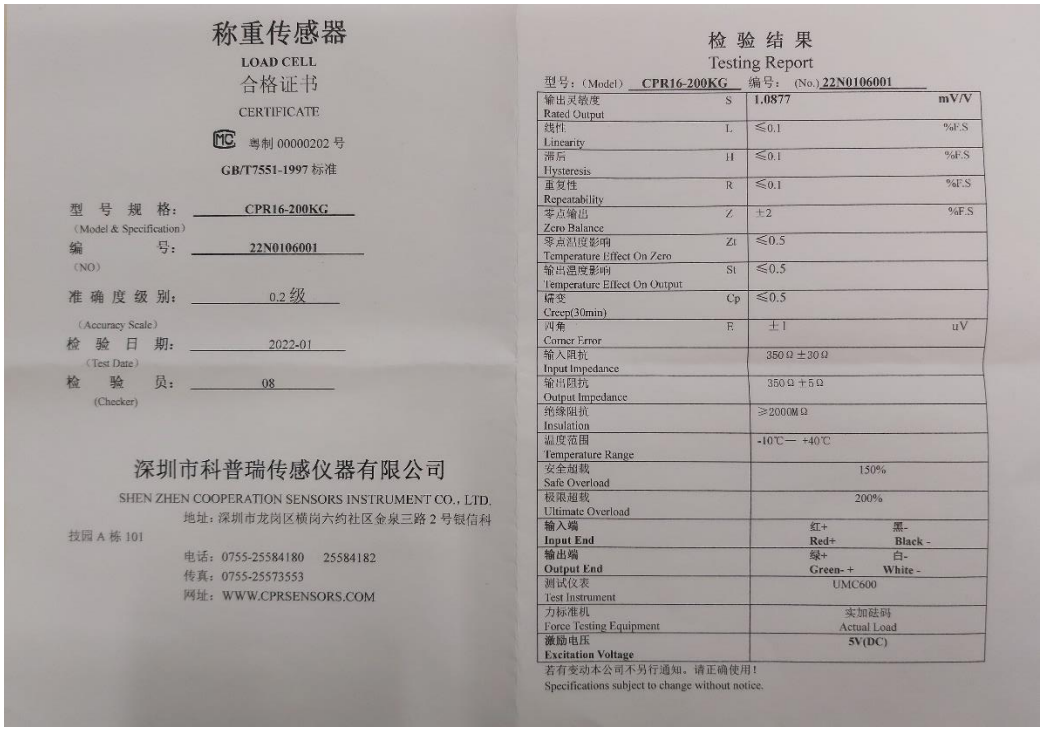

称重传感器

LOAD CELL

合格证书

CERTIFICATE

粤制 00000202 号

GB/T7551-1997 标准

型 号 规 格: CPR16-200KG
(Model & Specification)

编 号: 22N0106001
(NO)

准 确 度 级 别: 0.2 级
(Accuracy Scale)

检 验 日 期: 2022-01
(Test Date)

检 验 员: 08
(Checker)

深圳市科普瑞传感仪器有限公司

SHEN ZHEN COOPERATION SENSORS INSTRUMENT CO., LTD.

地址：深圳市龙岗区横岗六约社区金泉三路 2 号银信科技园 A 栋 101

电话：0755-25584180 25584182

传真：0755-25573553

网址：WWW.CPRSENSORS.COM

检 验 结 果

Testing Report

型号：(Model) CPR16-200KG 编号：(No.) 22N0106001

输出灵敏度 Rated Output	S	1.0877	mV/V
线性 Linearity	L	≤0.1	%F.S
滞后 Hysteresis	H	≤0.1	%F.S
重复性 Repeatability	R	≤0.1	%F.S
零点输出 Zero Balance	Z	±2	%F.S
零点温度影响 Temperature Effect On Zero	Zt	≤0.5	
输出温度影响 Temperature Effect On Output	St	≤0.5	
蠕变 Creep(30min)	Cp	≤0.5	
间角 Corner Error	E	±1	uV
输入阻抗 Input Impedance		350Ω±30Ω	
输出阻抗 Output Impedance		350Ω±5Ω	
绝缘阻抗 Insulation		≥2000MΩ	
温度范围 Temperature Range		-10℃— +40℃	
安全超载 Safe Overload		150%	
极限超载 Ultimate Overload		200%	
输入端 Input End		红+ Red+ 黑- Black -	
输出端 Output End		绿+ Green- + 白- White -	
测试仪表 Test Instrument		UMC600	
力标准机 Force Testing Equipment		实加砝码 Actual Load	
激励电压 Excitation Voltage		5V(DC)	

若有变动本公司不另行通知，请正确使用！

Specifications subject to change without notice.

Image C.1 – Compression load cell specification sheet

Measurements reading program code

```
#include <HX711_ADC.h>
#if defined(ESP8266)|| defined(ESP32) || defined(AVR)
#include <EEPROM.h>
#endif

//pins:
const int HX711_dout = 4; //mcu > HX711 dout pin
const int HX711_sck = 5; //mcu > HX711 sck pin

//HX711 constructor:
HX711_ADC LoadCell(HX711_dout, HX711_sck);

const int calVal_eepromAdress = 0;
unsigned long t = 0;
```

```
oid setup() {
  Serial.begin(57600); delay(10);
  Serial.println();
  Serial.println("Starting...");

  LoadCell.begin();
  //LoadCell.setReverseOutput(); //uncomment to turn a negative output value to positive
  float calibrationValue; // calibration value (see example file "Calibration.ino")
  //calibrationValue = 696.0; // uncomment this if you want to set the calibration value in the sketch
#if defined(ESP8266)|| defined(ESP32)
  //EEPROM.begin(512); // uncomment this if you use ESP8266/ESP32 and want to fetch the calibration value from
eeprom
#endif
  EEPROM.get(calVal_eepromAdress, calibrationValue); // uncomment this if you want to fetch the calibration
value from eeprom

  unsigned long stabilizingtime = 2000; // preciscion right after power-up can be improved by adding a few seconds
of stabilizing time
  boolean _tare = true; //set this to false if you don't want tare to be performed in the next step
  LoadCell.start(stabilizingtime, _tare);
  if (LoadCell.getTareTimeoutFlag()) {
    Serial.println("Timeout, check MCU>HX711 wiring and pin designations");
    while (1);
  }
  else {
    LoadCell.setCalFactor(calibrationValue); // set calibration value (float)
    Serial.println("Startup is complete");
  }
}

void loop() {
  static boolean newDataReady = 0;
  const int serialPrintInterval = 0; //increase value to slow down serial print activity
```

```
  // check for new data/start next conversion:
  if (LoadCell.update()) newDataReady = true;

  // get smoothed value from the dataset:
  if (newDataReady) {
    if (millis() > t + serialPrintInterval) {
      float i = LoadCell.getData();
      Serial.print("Load_cell output val: ");
      Serial.println(i);
      newDataReady = 0;
      t = millis();
    }
  }

  // receive command from serial terminal, send 't' to initiate tare operation:
  if (Serial.available() > 0) {
    char inByte = Serial.read();
    if (inByte == 't') LoadCell.tareNoDelay();
  }

  // check if last tare operation is complete:
  if (LoadCell.getTareStatus() == true) {
    Serial.println("Tare complete");
  }

}
```

Calibration program code

```
#include <HX711_ADC.h>
#if defined(ESP8266)|| defined(ESP32) || defined(AVR)
#include <EEPROM.h>
#endif

//pins:
const int HX711_dout = 4; //mcu > HX711 dout pin
const int HX711_sck = 5; //mcu > HX711 sck pin

//HX711 constructor:
HX711_ADC LoadCell(HX711_dout, HX711_sck);

const int calVal_eepromAdress = 0;
unsigned long t = 0;

void setup() {
  Serial.begin(57600); delay(10);
  Serial.println();
  Serial.println("Starting...");

  LoadCell.begin();
  //LoadCell.setReverseOutput(); //uncomment to turn a negative output value to positive
  unsigned long stabilizingtime = 2000; // preciscion right after power-up can be improved by adding a few seconds
of stabilizing time
  boolean _tare = true; //set this to false if you don't want tare to be performed in the next step
  LoadCell.start(stabilizingtime, _tare);
  if (LoadCell.getTareTimeoutFlag() || LoadCell.getSignalTimeoutFlag()) {
    Serial.println("Timeout, check MCU>HX711 wiring and pin designations");
    while (1);
  }
  else {
    LoadCell.setCalFactor(1.0); // user set calibration value (float), initial value 1.0 may be used for this sketch
```

```
  Serial.println("Startup is complete");
 }
 while (!LoadCell.update());
 calibrate(); //start calibration procedure
}

void loop() {
 static boolean newDataReady = 0;
 const int serialPrintInterval = 0; //increase value to slow down serial print activity

 // check for new data/start next conversion:
 if (LoadCell.update()) newDataReady = true;

 // get smoothed value from the dataset:
 if (newDataReady) {
  if (millis() > t + serialPrintInterval) {
   float i = LoadCell.getData();
   Serial.print("Load_cell output val: ");
   Serial.println(i);
   newDataReady = 0;
   t = millis();
  }
 }

 // receive command from serial terminal
 if (Serial.available() > 0) {
  char inByte = Serial.read();
  if (inByte == 't') LoadCell.tareNoDelay(); //tare
  else if (inByte == 'r') calibrate(); //calibrate
  else if (inByte == 'c') changeSavedCalFactor(); //edit calibration value manually
 }

 // check if last tare operation is complete
```

```
  if (LoadCell.getTareStatus() == true) {
    Serial.println("Tare complete");
  }

}

void calibrate() {
  Serial.println("***");
  Serial.println("Start calibration:");
  Serial.println("Place the load cell an a level stable surface.");
  Serial.println("Remove any load applied to the load cell.");
  Serial.println("Send 't' from serial monitor to set the tare offset.");

  boolean _resume = false;
  while (_resume == false) {
    LoadCell.update();
    if (Serial.available() > 0) {
      if (Serial.available() > 0) {
        char inByte = Serial.read();
        if (inByte == 't') LoadCell.tareNoDelay();
      }
    }
    if (LoadCell.getTareStatus() == true) {
      Serial.println("Tare complete");
      _resume = true;
    }
  }

  Serial.println("Now, place your known mass on the loadcell.");
  Serial.println("Then send the weight of this mass (i.e. 100.0) from serial monitor.");

  float known_mass = 0;
  _resume = false;
```

```
  while (_resume == false) {
    LoadCell.update();
    if (Serial.available() > 0) {
      known_mass = Serial.parseFloat();
      if (known_mass != 0) {
        Serial.print("Known mass is: ");
        Serial.println(known_mass);
        _resume = true;
      }
    }
  }

  LoadCell.refreshDataSet(); //refresh the dataset to be sure that the known mass is measured correct
  float newCalibrationValue = LoadCell.getNewCalibration(known_mass); //get the new calibration value

  Serial.print("New calibration value has been set to: ");
  Serial.print(newCalibrationValue);
  Serial.println(", use this as calibration value (calFactor) in your project sketch.");
  Serial.print("Save this value to EEPROM adress ");
  Serial.print(calVal_eepromAdress);
  Serial.println("? y/n");

  _resume = false;
  while (_resume == false) {
    if (Serial.available() > 0) {
      char inByte = Serial.read();
      if (inByte == 'y') {
#if defined(ESP8266)|| defined(ESP32)
        EEPROM.begin(512);
#endif
        EEPROM.put(calVal_eepromAdress, newCalibrationValue);
#if defined(ESP8266)|| defined(ESP32)
        EEPROM.commit();
```

```
#endif
      EEPROM.get(calVal_eepromAdress, newCalibrationValue);
      Serial.print("Value ");
      Serial.print(newCalibrationValue);
      Serial.print(" saved to EEPROM address: ");
      Serial.println(calVal_eepromAdress);
      _resume = true;

    }
    else if (inByte == 'n') {
      Serial.println("Value not saved to EEPROM");
      _resume = true;
    }
  }
 }

 Serial.println("End calibration");
 Serial.println("***");
 Serial.println("To re-calibrate, send 'r' from serial monitor.");
 Serial.println("For manual edit of the calibration value, send 'c' from serial monitor.");
 Serial.println("***");
}

void changeSavedCalFactor() {
 float oldCalibrationValue = LoadCell.getCalFactor();
 boolean _resume = false;
 Serial.println("***");
 Serial.print("Current value is: ");
 Serial.println(oldCalibrationValue);
 Serial.println("Now, send the new value from serial monitor, i.e. 696.0");
 float newCalibrationValue;
 while (_resume == false) {
  if (Serial.available() > 0) {
```

```
    newCalibrationValue = Serial.parseFloat();
    if (newCalibrationValue != 0) {
      Serial.print("New calibration value is: ");
      Serial.println(newCalibrationValue);
      LoadCell.setCalFactor(newCalibrationValue);
      _resume = true;
    }
  }
}
_resume = false;
Serial.print("Save this value to EEPROM adress ");
Serial.print(calVal_eepromAdress);
Serial.println("? y/n");
while (_resume == false) {
  if (Serial.available() > 0) {
    char inByte = Serial.read();
    if (inByte == 'y') {
#if defined(ESP8266)|| defined(ESP32)
      EEPROM.begin(512);
#endif
      EEPROM.put(calVal_eepromAdress, newCalibrationValue);
#if defined(ESP8266)|| defined(ESP32)
      EEPROM.commit();
#endif
      EEPROM.get(calVal_eepromAdress, newCalibrationValue);
      Serial.print("Value ");
      Serial.print(newCalibrationValue);
      Serial.print(" saved to EEPROM address: ");
      Serial.println(calVal_eepromAdress);
      _resume = true;
    }
    else if (inByte == 'n') {
      Serial.println("Value not saved to EEPROM");
```

```
      _resume = true;
     }
    }
  }
  Serial.println("End change calibration value");
  Serial.println("***");
}
```

--- end of document ---